

LASER MATERIALS AND TECHNOLOGY RESEARCH CENTER  
OF GENERAL PHYSICS INSTITUTE

F61775-98-WE056  
SPC 98-4043

FINAL REPORT

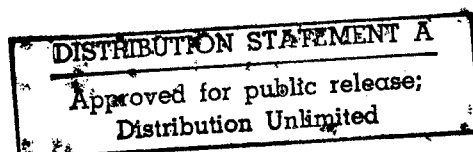
on the project

**Solid state Raman Materials Characterization for  
High Average Power 1.3  $\mu\text{m}$  Laser Frequency Shift**

Moscow  
January 1999

19990305 009

DTIC QUALITY INSPECTED 1



AQF99-06-1074

# Content

## Introduction.

### 1. Nonlinear susceptibility, Raman scattering and "Z-scan" technique

#### 1.1. Nonlinear susceptibility (theoretical approach)

#### 1.2. Stimulated Raman scattering (theoretical approach)

#### 1.3. Raman scattering and "Z-scan" technique

### 2. Optimization of the Raman Laser Intracavity Pumping

### 3. Spontaneous Raman spectroscopy of crystals.

#### 3.1. Experimental setup

#### 3.2. Tungstate crystals

Comparison of different tungstate crystals

Phase transitions in double tungstate crystals

Line broadening of SRS-active mode in KGW crystal

#### 3.3. Molibdate crystals

#### 3.4. Simple oxide crystals

#### 3.5. Semiconductor crystals

### 4. Investigation of Raman gain characteristics of solid state materials by SRS-amplification technique.

# REPORT DOCUMENTATION PAGE

Form Approved OMB No. 0704-0188

Public reporting burden for this collection of information is estimated to average 1 hour per response, including the time for reviewing instructions, searching existing data sources, gathering and maintaining the data needed, and completing and reviewing the collection of information. Send comments regarding this burden estimate or any other aspect of this collection of information, including suggestions for reducing this burden to Washington Headquarters Services, Directorate for Information Operations and Reports, 1215 Jefferson Davis Highway, Suite 1204, Arlington, VA 22202-4302, and to the Office of Management and Budget, Paperwork Reduction Project (0704-0188), Washington, DC 20503.

1. AGENCY USE ONLY (Leave blank)	2. REPORT DATE  January 1999	3. REPORT TYPE AND DATES COVERED  Final Report	
4. TITLE AND SUBTITLE  Solid State Raman Materials Characterization for High Power 1.3 $\mu$ m Laser Frequency Shift		5. FUNDING NUMBERS  F61775-98-	
6. AUTHOR(S)  Prof Tasoltan Tazretovich Basiev		8. PERFORMING ORGANIZATION REPORT NUMBER  N/A	
7. PERFORMING ORGANIZATION NAME(S) AND ADDRESS(ES)  Laser Materials and Technology Research Center of the General Physics Institute Vavilov St. 38 Moscow 117942 Russia			
9. SPONSORING/MONITORING AGENCY NAME(S) AND ADDRESS(ES)  EOARD PSC 802 BOX 14 FPO 09499-0200		10. SPONSORING/MONITORING AGENCY REPORT NUMBER  SPC 98-4043	
11. SUPPLEMENTARY NOTES			
12a. DISTRIBUTION/AVAILABILITY STATEMENT  Approved for public release; distribution is unlimited.		12b. DISTRIBUTION CODE  A	
13. ABSTRACT (Maximum 200 words)  This report results from a contract tasking Laser Materials and Technology Research Center of the General Physics Institute as follows: The contractor will evaluate the thermomechanical and optical properties, and conduct Raman spectroscopic studies and laser laboratory tests to determine the most promising Raman frequency shifting materials for use with 1.3 micron, high power lasers.			
14. SUBJECT TERMS  EOARD, Raman laser materials, Non-linear Optical Materials , Laser Raman Conversion		15. NUMBER OF PAGES  85	16. PRICE CODE  N/A
17. SECURITY CLASSIFICATION OF REPORT  UNCLASSIFIED	18. SECURITY CLASSIFICATION OF THIS PAGE  UNCLASSIFIED	19. SECURITY CLASSIFICATION OF ABSTRACT  UNCLASSIFIED	20. LIMITATION OF ABSTRACT  UL

## Introduction.

Stimulated Raman Scattering (SRS) in solid state materials is a new extensively growing area in laser physics. SRS allows to change the laser radiation frequency with a certain frequency shift which is determined by spontaneous Raman spectra of nonlinear material. The first observation of stimulated Raman scattering in solids was published in 1963 [1]. The authors investigated SRS in diamond, calcite and  $\alpha$ -sulfur single crystals. Since then the natural calcite crystal has become the most popular Raman material due to its comparatively large size and low cost. It has an intense quasi molecular SRS-active vibronic mode with the energy as large as  $1086\text{ cm}^{-1}$  and linewidth about  $1.2\text{ cm}^{-1}$  [2, 3]. The Raman gain coefficient was measured to be  $5.5\text{ cm/GW}$  at  $532\text{ nm}$  wavelength [4]. The diamond crystal has larger Raman frequency shift  $1332\text{ cm}^{-1}$  and higher gain [5]. But due to its small dimensions and high cost it has not found practical applications as a Raman material.

In 1980 a number of new synthetic crystals, barium, sodium, and lead nitrates were proposed as perspective Raman laser materials [5]. These crystals have intense vibronic modes with the energy of about  $1050\text{ cm}^{-1}$ , which correspond to the internal symmetrical vibrations of  $[\text{NO}_3]$  molecular ion. The Raman gain in  $\text{Ba}(\text{NO}_3)_2$  crystal was measured to be as high as  $47\text{ cm/GW}$  at  $532\text{ nm}$  wavelength [4]. The number of various laser configurations have shown that the quantum conversion efficiency of  $\text{Ba}(\text{NO}_3)_2$  SRS shifter can be up to 80% for nanosecond laser pulses [7-9] even for IR radiation with much lower gain. This has lead to the availability of commercial solid state Raman lasers with special properties such as high efficiency and diffraction-limited beam quality at eye-safe wavelengths [10]. However, the SRS threshold for 25 ps pump pulses was found to be 10 times higher than that for nanosecond pulses due to long vibronic relaxation time [11]. This transient SRS was accompanied by wide angular scattering to higher Stokes and anti-Stokes components, that interferes in their application for picosecond pump pulses.

Authors [12, 13] found that potassium gadolinium tungstate,  $\text{KGd}(\text{WO}_4)_2$  exhibited efficient Raman properties. In spite of the fact that its Raman gain coefficient at  $1064\text{ nm}$  ( $6\text{ cm/GW}$ ) is twice less than that in barium nitrate, the KGW crystal found many practical applications for frequency shifting of picosecond laser radiation [13]. Variations in the Raman scattering cross section and Raman mode linewidth are responsible for the difference in the behaviour of the above SRS materials.

The detailed spectroscopic investigation of SRS-active vibronic modes in many different crystalline materials using spontaneous Raman spectroscopy and analysis of their non-linear Raman properties are presented in this report.

1. G. Eckhardt, D. P. Bortfeld, and M. Geller, „Stimulated emission of Stokes and anti-Stokes Raman lines from diamond, calcite and  $\alpha$ -sulphur single crystals,” *Appl. Phys. Lett.*, **3**, 137-138 (1963).
2. G. Bisson, and G. Mayer, „Effects Raman stimule's dans la calcite,” *Cr. Acad. Sci. (Paris)*, **265**, 397-398 (1967).
3. K. Park, „New width data of the  $A_{1g}$  Raman line in calcite,” *Phys. Lett.* **22**, 39-41 (1966); K. Park, „Thermal variation of a Raman line width in calcite,” *Phys. Lett.* **A25**, 490-491 (1967).
4. S. N. Karpukhin and A. I. Stepanov, „Intracavity Raman emission in  $Ba(NO_3)_2$ ,  $NaNO_3$  and  $CaCO_3$  crystals,” *Sov J. Quantum Electron.* **16**, 1027-1032 (1986).
5. G. Eckhardt, „Selection of Raman materials,” *IEEE J. Quantum Electr.*, **QE-2**, 1-8 (1966).
6. A. S. Eremenko, S. N. Karpukhin, and A. I. Stepanov, „SRS of the second harmonic of neodymium laser in nitrate crystals,” *Sov. J. Quantum Electron.*, **10**, 113-116 (1980).
7. T. T. Basiev, V. N. Voitsekhovskii, P. G. Zverev, F. V. Karpushko, A. V. Lubimov, S. B. Mirov, V. P. Morozov, I. V. Mochalov, A. A. Pavlyuk, G. V. Sinityn, and V. E. Yakobson, „Conversion of tunable radiation from a laser utilising an  $LiF$  crystal containing  $F_2^-$  colour centres by stimulated Raman scattering in  $Ba(NO_3)_2$  and  $KGd(WO_4)_2$  crystals,” *Sov. J. Quantum Electron.*, **17**, 1560-1563 (1987).
8. P. G. Zverev, and T. T. Basiev, „Compact SRS laser on barium nitrate crystal,” *Proceedings of All-Union Conference „Laser Optics“*, Leningrad, **2**, 363 (1993).
9. P. G. Zverev, T. T. Basiev, I. V. Ermakov, and A. M. Prokhorov, „Stimulated Raman scattering in barium nitrate crystal in the external optical cavity,” in *Laser Methods of Surface Treatment and Modification*, SPIE - The International Society for Optical Engineering, **2498**, 164-169 (1994).
10. J. T. Murray, R. C. Powell, N. Peyghambarian, D. Smith, W. Austin, and R. A. Stolzenberger, „Generation of 1.5  $\mu$ m radiation through intracavity solid-state Raman shifting in  $Ba(NO_3)_2$  non-linear crystals,” *Opt. Lett.* **20**, 1017-1019 (1995).
11. P. G. Zverev, J. T. Murray, R. C. Powell, R. J. Reeves, and T. T. Basiev, „Stimulated Raman scattering of picosecond pulses in barium nitrate crystals,” *Optics Commun.*, **97**, 59-63 (1993).
12. K. Andryunas, Y. K. Vishchakas, V. Kabelka, I. V. Mochalov, A. A. Pavlyuk, G. T. Petrovskii and V. P. Syrus, „SRS-self-conversion of  $Nd^{3+}$  laser emission in tungstate crystals,” *JETP Letters* **42**, 410-412 (1985).
13. A. M. Ivanuk, M. A. Ter-Pogosyan, P. A. Shakhverdov, V. D. Belyaev, V. L. Ermolayev, and N. P. Tikhonova, „Picosecond light pulses under intracavity stimulated Raman scattering in the active element of neodymium laser,” *Optika i Spectroskopiya*, **59**, 950-952 (1985) (in Russian); A. M. Ivanuk, V. A. Sandulenko, M. A. Ter-Pogosyan, P. A. Shakhverdov, V. G. Chervinskii, A. V. Lukin, and V. L. Ermolaev, „Intracavity stimulated Raman scattering in a nanosecond neodymium laser based on potassium gadolinium tungstate,” *Optika i Spectroskopiya*, **62**, 961-962 (1987) (in Russian).
14. CRS Handbook of Laser Science and Technology, Nonlinear Optical Properties, pp.269-288 (1995).

# 1. Nonlinear susceptibility, Raman scattering and 'Z-scan' technique

## 1.1. Nonlinear susceptibility (theoretical approach)

Stimulated Raman scattering (SRS) as a nonlinear process derive its behavior from the nonlinear index of refraction. The general description of the nonlinear refractive index on light intensity can be expressed as

$$n(r,t) = n_0(r,t) + \Delta n(I(r,t)) \quad (1.1)$$

This equation indicates that the change in the refractive index  $\Delta n$  over its value at low intensities  $n_0$  has a functional dependence on the intensity of light  $I(r,t)$ . In case of Kerr-like media the nonlinear refractive index change can be written as  $\Delta n(I(r,t)) = n_2 \langle E \cdot E \rangle$ , where  $n_2$  is called the nonlinear index coefficient, and the angle brackets indicate a time average over at least one optical cycle. The oscillation of the optical light is too quick, so the nonlinear index of refraction depends on the slowly varying complex amplitude  $E(r,t)$ . Since the intensity  $I \sim |E|^2$ , it is sometimes convenient to express the nonlinear index in terms of intensity:  $\Delta n = \gamma I$ , where  $\gamma$  is the nonlinear refractive coefficient.

The nonlinear index coefficient is related to the third order nonlinear susceptibility that appears in the expansion of third order of the nonlinear polarization. The  $i$ -th component ( $i = x, y, z$ ) of this third order polarization at probe frequency  $\omega'$  induced by the strong pump beam with frequency  $\omega$  is given by

$$P_i^{(3)}(\omega') = 6\epsilon_0 \sum_{jkl} \chi_{ijkl}^{(3)}(-\omega', \omega', \omega, -\omega) E_j(\omega') E_k(\omega) E_l^*(\omega) \quad (1.2)$$

Equation that relate  $n_2$  and  $\gamma$  to the third order susceptibility for isotropic material and linear polarization of the pump laser looks as following (cgs units):

$$\gamma = \frac{4\pi}{n_0 c} n_2 = \frac{12\pi^2}{n_0^2 c} \chi_{xxxx}^{(3)}(-\omega', \omega', \omega, -\omega) \quad (1.3)$$

The nonlinear refractive index is not a unique quantity for a given material, because a number of physical mechanisms contribute to the nonlinear polarization that is cubic in applied optical electric field. These physical mechanisms require some material response, and that response can take place on various time scales. The mechanisms that contribute most strongly to  $n_2$  and their characteristic time scales (in brackets) are: bound electrons ( $10^{-15}$  s), optically created free carriers ( $>10^{-12}$  - 1 s), Raman-active optical phonons ( $10^{-12}$  s), electrostriction ( $>10^{-9}$  s), and thermal excitation ( $\sim 10^{-9}$  - 1 s) [1]. The most part of theoretical investigations of nonlinear physical mechanisms concerned with the bound electron contribution to  $n_2$  or  $\chi^{(3)}$ . On the other hand, the

effects of optical phonons and libration of molecular units can occur on such a short time scale that they contribute fully to nearly all of the measurements of  $n_2$ . Very little experimental and theoretical work has been done to distinguish between these contributions. It has been shown that in glasses the optical phonon contribution is ~20% as large as that of the bound electrons [2, 3]

Boling, Gass and Owyong [4] derived an empirical formula relating  $n_2$  at wavelengths much longer than the interband absorption to the linear refractive index and its dispersion. Recent work has shown that this formula, which is widely accepted as a method for estimating  $n_2$ , is accurate to within about 25% for a wide range of crystals and glasses [5, 6]. The third order polarizabilities (also so called hyperpolarizabilities) of isolated atoms and molecules act as the sources of nonlinear refraction. A similar concept is useful for solids. Recently, the calculations of ionic hyperpolarizabilities were made for alkali halide crystals [7], and it was shown that the anions were the dominant source of  $\chi^{(3)}$ , although this anion hyperpolarizability is strongly dependent on the size of the coordinating cation, so hyperpolarizabilities are not uniquely defined in solids. Below we will consider data on hyperpolarizability and Raman properties in simple oxide materials.

1. R. W. Hellwarth, J. Cherlow "Origin and frequency dependence of nonlinear optical susceptibilities of glasses", Phys. Rev. **B11**, 964 (1975).
2. D. Heiman, R. W. Hellwarth, and D. S. Hamilton, "Raman scattering and nonlinear refractive index measurements of optical glasses", J. Non-Cryst. Solids **34**, 63 (1979)].
3. N. L. Boling, A. J. Glass, and A. Owyong, "Empirical relationships for predicting nonlinear refractive index changes in optical solids", IEEE J Quantum Electronics, **QE-14**, 601 (1978).
4. R. Adair, L. L. Chase, and S. A. Payne, Nonlinear refractive index measurements of glasses using three-wave frequency mixing", J. Opt. Soc Amer. **B4**, 875 (1987).
5. R. Adair, L. L. Chase, and S. A. Payne, Nonlinear refractive index of optical crystals", Phys Rev. **B39**, 3337 (1989).
6. M. D. Johnson, K. R. Subbaswamy, and G. Senatore, Hyperpolarizabilities of alkali halide crystals using the local density approximation", Phys. Rev. **B36**, 9202 (1987).

## 1.2. Stimulated Raman Scattering (theoretical approach)

Stimulated Raman scattering SRS as a nonlinear process can be described in the linear approximation with nonlinear susceptibility  $\chi^{(3)}$ . The third order polarization at the Stokes frequency is given by

$$P_S^{(3)} = 6\epsilon_0 \chi_R^{(3)}(-\omega_S; \omega_S, \omega_L, \omega_L) E_S |E_L|^2 \quad (1.4)$$

where all the fields are linearly polarized and are parallel. The subscript  $R$  signifies a Raman susceptibility, which is a complex quantity. The Raman gain factor is related to the imaginary part of this susceptibility:

$$G(\omega_S) = -\frac{6\omega_S}{n_s c} \text{Im} \left[ \chi_R^{(3)}(-\omega_S; \omega_S, \omega_L, -\omega_L) \right] |E_L|^2 \quad (1.5)$$

where  $n_s$  is the linear index of refraction at the Stokes frequency, and the exponential gain factor  $G(\omega_S)$  has units of  $\text{m}^{-1}$ . The real and imaginary parts of  $\chi_R^{(3)}$  are related through Kramers-Kronig relation. The frequency dependence of the gain factor displays a Raman resonance:

$$G(\omega_S) = \frac{\left(\frac{\Gamma}{2}\right)^2 G^{peak}}{\left[\omega_S - (\omega_L - \omega_V)\right]^2 + \left(\frac{\Gamma}{2}\right)^2} \quad (1.6)$$

where  $G^{peak}$  is the peak gain,  $\Gamma$  is the Raman linewidth,  $\Omega_L$  - is the Raman resonance. The nonlinear index coefficient is related to the real part of  $\chi_R^{(3)}$  and can be expressed in terms of the gain coefficient  $g_S$ , which is the gain factor  $G(\omega_S)$  per unit pump intensity.

In the classical picture, for plane pump and Stokes waves, SRS is described as a coupling of the optical waves to the coherent material excitation [1]. In the moving frame  $(z, t)$  where the optical pulses are at rest, the set of coupled differential equations can be written as [2]:

$$\frac{\partial E_p(z, t)}{\partial z} = -K_p E_s A_Q \quad (1.7a)$$

$$\frac{\partial E_s(z, t)}{\partial z} = K_s E_p A_Q^* \quad (1.7b)$$

$$\left(\frac{\partial}{\partial t} + \Gamma\right) A_Q^* = E_p^* E_s \quad (1.7c)$$

Here  $K_p$  and  $K_s$  are coupling coefficients which include the Raman susceptibility;  $E_p$  and  $E_s$  are the pump and Stokes optical field amplitudes, and  $A_Q$  is the amplitude of material excitation.  $\Gamma$  is the Raman linewidth which is for homogeneously broadened line equals  $\Gamma = c\Delta\Omega_R = (\pi T_R)^{-1}$ , here  $T_R$  is the dephasing time and  $\Delta\Omega_R$  is FWHM. The theoretical treatment of the set of equations (1.7) can

be found in [3-6]. Depending on the pump pulse duration two temporal cases: a steady-state and a transient can be considered.

The steady state case is observed when the duration of the pump laser pulse is longer than the vibronic relaxation time ( $\tau_p \gg T_R$ ). In this case if there is no pump depletion, the solution for the Stokes amplitude is exponential with a plane wave gain coefficient given as  $G_{ss} = K_s \Gamma^{-1} |E_p|^2$ . This solution is readily obtained from the coupled set (1.7) when it is noted that, no changes of  $A_Q$  occur for a constant pump:  $\frac{dA_Q}{dt} = 0$ . The intensity of the first Stokes component can be written as [5]:

$$I_s(l) = I_s(0) \exp\{g_{ss} I_p l\} \quad (1.8)$$

Here  $I_s(0)$  and  $I_s(l)$  are Stokes intensities at the input and the output of the Raman medium,  $I_p$  is the pump intensity and  $l$  is the length of the nonlinear crystal. The  $g_{ss}$  is a steady state Raman gain coefficient which is determined by the Raman properties of nonlinear medium [5]:

$$g_{ss} = \frac{\lambda_p \lambda_s^2 N}{\hbar c \pi n_s^2 \Delta\Omega_R} \left( \frac{d\sigma}{d\Omega} \right) \quad (1.9)$$

Here  $N$  is the number of scattering centers,  $\lambda_{p,s}$  are the pump and Stokes wavelengths,  $n_s$  - refractive index at  $\lambda_s$  and  $\frac{d\sigma}{d\Omega}$  is the Raman scattering cross section. Thus, we can note that in the steady state case the Raman gain coefficient  $g_{ss}$  is linearly proportional to the Raman scattering cross section and inversely proportional to the linewidth of Raman transition. The Raman linewidth is determined by a mechanism of vibronic phase relaxation due to the phonon-phonon coupling in the medium [6]. The value of  $\frac{d\sigma}{d\Omega} (\Delta\Omega_R)^{-1}$  can be measured as a maximum in the spontaneous Raman scattering spectrum and for simplicity we will denote it as  $\Sigma_{peak}$ .

After Wang [3] in the transient case ( $\tau_p \ll T_R$ ) with no pump depletion the transient Raman gain  $G_{tr}$  equals:

$$G_{tr} l = \ln \frac{|E_s(l)|}{|E_s(0)|} \cong 2 \left( K_s I \int_{-\infty}^{\tau_p} |E_p(t')|^2 dt' \right)^{1/2} \quad (1.10)$$

And for rectangular pump pulse with duration  $\tau_p$  it can be rewritten as

$$G_{tr} l \sim 2 \left( K_s I |E_p|^2 \tau_p \right)^{1/2} = 2 \left( G_{ss} l c \Delta\Omega_R \tau_p \right)^{1/2} \quad (1.11)$$

One can see that the transient Raman gain  $G_{tr}$  is reduced with shortening pump pulse as  $(\tau_p)^{1/2}$  and is proportional to the multiplication of  $G_{ss} \Delta\Omega_R$ , hence, it depends on the integral Raman

scattering cross section. The analytical expression for the Stokes amplitude for large amplification gain was found in [3] as

$$I_s(l) \sim I_s(0) \exp \left[ 2 \sqrt{\left( I_p \tau_p l \frac{8\pi^2 c^2 N}{\hbar \omega_s^3 n^2} \left( \frac{d\sigma}{d\Omega} \right) \right)} - \pi c \Delta \Omega_R \tau_p \right] \quad (1.12)$$

From (1.12) one can see that for large amplification when the second term in the exponent gain is small the Raman gain is proportional to the square root of the total integral Raman scattering cross section  $\frac{d\sigma}{d\Omega}$ . It can be measured as an integral value of the Raman line intensity

in spontaneous Raman scattering spectrum and we denoted it as  $\Sigma_{int} = d\sigma/d\Omega$

Below we will compare spectroscopic characteristics  $\Sigma_{peak}$  and  $\Sigma_{int}$  in different materials in order to characterize their SRS features for the Raman laser development.

1. Y. R. Shen, *The Principles of Nonlinear Optics* (New York; John Wiley & Sons Inc., 1984). ch. 10 „Stimulated Raman Scattering,“ (pages 146-185 in Russian translation published by «Nauka», Moscow 1989).
2. R. L. Carman, F. Shimizu, C. S. Wang, and N. Bloembergen, „Theory of Stokes pulse shapes in transient stimulated Raman scattering,“ *Phys. Rev.*, **A2**, 60-72 (1972).
3. Y. Wang, „Theory of stimulated Raman scattering,“ *Phys. Rev.*, **182**, 482-494 (1969).
4. M. G. Raymer, and J. A. Walmsley, „The quantum coherence properties of stimulated Raman scattering“, in *Progress in Optics*, **XXIII**, E. Wolf, ed. Amsterdam, Elsevier Science, 181-270 (1990).
5. W. Kaiser, and M. Maier, „Stimulated Rayleigh, Brillouin and Raman spectroscopy,“ in *Laser Handbook*, F. T. Arecchi and E. O. Schulz-Dubois eds., ch. E2, 1077-1150 (Amsterdam, North-Holland Publishing Company, 1972).
6. P. G. Zverev, H. Liu, W. Jia, and T. T. Basiev, "Vibrational dynamic of Raman-active mode in barium nitrate crystal", *Optics Letters*, **20**, 2378-2380 (1995).

### 1.3. Raman scattering and 'Z-scan' technique

In this part of our report we compare our Raman spectroscopic data of solid state materials with nonlinear refractive index measurements obtained by different techniques. Among them a 'Z-scan' method is known as one of the most effective procedure to investigate and measure nonlinear refractive index as well as nonlinear absorption and losses in the medium.

In Table 1.1 data on  $n_2$  for some cubic fluoride crystals are presented following Ref. [1]. One can see that LiF crystal has the lowest value of  $n_2 = 0.26 \cdot 10^{-13}$  esu. A  $\text{CaF}_2$  crystal has slightly higher nonlinearity  $n_2 = 0.43 \cdot 10^{-13}$  esu and the highest value for fluorides is found in  $\text{CdF}_2$  crystal  $n_2 = 3.95 \cdot 10^{-13}$  esu which is 15 times larger than in LiF sample and 9 times larger than in  $\text{CaF}_2$ . As we can see in the range Ca, Sr, Ba fluorides crystals hyperpolarizability is increased with the increase of anion-cation separation. The sharp rise of hyperpolarizability in  $\text{CdF}_2$  crystal distinguish it from fluoride range and has fundamentally different origin. Cations with filled outlet shells may greatly augment the effective number of valence electrons. In  $\text{CdF}_2$  crystal the  $4d^{10}$  states of  $\text{Cd}^{2+}$  lie within only a few eV of the  $2p$  states of the fluoride ion. This accounts for the anomalous large effective hyperpolarizability for the  $\text{Cd}_{1/2}\text{F}$  pair (Table 1.1).

To find correlation between  $n_2$  and  $\chi^{(3)}$  property of fluoride crystals and their Raman scattering cross section we investigated spontaneous Raman scattering spectra of fluoride single crystals. We synthesized, cut and polished two optically transparent  $\text{CaF}_2$  and  $\text{CdF}_2$  crystals with equal thickness  $d=2\text{mm}$ . Then we proceed comparative spectroscopic measurements of spontaneous Raman spectra of these two crystals with  $\text{CaWO}_4$  tungstate crystal. Two spectra are shown in Fig. 1.1, 1.2. As we can see both calcium and cadmium fluorides exhibit single Raman scattering line feature with the frequency shift  $\Omega_R=323 \text{ cm}^{-1}$  for  $\text{CaF}_2$  crystal and  $\Omega_R=318 \text{ cm}^{-1}$  for  $\text{CdF}_2$ . Both lines get into the interesting region for developing high power Raman laser converter.

Peak values ( $\Sigma_{peak}$ ) of Raman scattering cross section are close to each other while the linewidth ( $\Delta\Omega_R$ ) and integral cross section ( $\Sigma_{integr.}$ ) in  $\text{CdF}_2$  crystal is much higher than in  $\text{CaF}_2$ . The  $\Sigma_{integr.}$  increasing well correlate with the higher polarizability and nonlinear refraction index in  $\text{CdF}_2$  crystal.

Comparison of peak and integral Raman scattering cross sections of investigated fluorine materials with reference data of  $\text{CaWO}_4$  crystal shows that in spite of the increase of  $\Sigma_{integr.}$  value from  $\text{CaF}_2$  to  $\text{CdF}_2$  crystals both of them remains much smaller than those in tungstate.

**Table 1.1. Nonlinearity, anion-cation separation and hyperpolarizability of some fluoride cubic crystals [1].**

<i>Sample</i>	$n_2$ ( $10^{-13}$ esu)	<i>Anion-Cation Separation (Å)</i>	<i>Hyperpolarizability, <math>\gamma(M_xF)</math> (<math>10^{-39}</math> esu)</i>
LiF	0.26	2.01	141
CaF <sub>2</sub>	0.43	2.37	282
SrF <sub>2</sub>	0.5	2.51	412
BaF <sub>2</sub>	0.67	2.69	626
CdF <sub>2</sub>	3.95	2.33	1520

In 1989 Sheik-bahae et al. [3] developed a sensitive self-focusing measurement technique that involves focusing a laser beam through a thin sample and detecting the light transmitted by a small aperture in the far field. This method is illustrated in Fig.1.3. It consists in scanning of a sample along the z-axis through the focus of the lens for a constant laser input and analyzing the change of spatial distribution and intensity of the transmitted beam.

Assuming a Gaussian beam traveling in +z direction, the magnitude of electromagnetic field  $E(z)$  along the optical axis can be written as:

$$|E(r, z, t)| = |E_0(t)| \frac{\omega_0}{\omega(z)} \exp\left[-\frac{r^2}{\omega^2(z)}\right] \quad (1.13)$$

**Table 1.2. Comparative spontaneous Raman scattering data for calcium and cadmium fluoride and calcium tungstate single crystals.**

<i>Sample</i>	$\Omega_R$ ( $cm^{-1}$ )	$\Delta\Omega_R$ ( $cm^{-1}$ )	$\Sigma_{integr.}$ a.u.*	$\Sigma_{peak}$ a.u.*
CaF <sub>2</sub>	323	8.4	0.07	0.21
CdF <sub>2</sub>	318	21	0.16	0.2
CaWO <sub>4</sub>	208	76	47	18.6

\* - the values of  $\Sigma_{peak}$  and  $\Sigma_{integ.}$  are normalized to those in diamond crystal following Ref. [2]

where  $\omega^2(z) = \omega_0^2(1 + z^2/z_0^2)$  is the beam radius at  $z$ ,  $z_0 = k\omega_0/2$  is the diffraction length of the beam,  $k = 2\pi/\lambda$  is the wave vector, and  $\lambda$  is the laser wavelength.  $E_0$  denotes the radiation electric field at the focus and contains the temporal evolution of the laser pulse. So the intensity of the laser input beam inside the crystal is changed depending on its position along the  $z$ -axis.

Two types of experiments can be made with 'Z-scan' technique. Usually the far field pattern is registered by collecting all the light transmitted through the sample with partly closed aperture in front of detector and without it. The set of data with the aperture is referred to as a "closed aperture" Z-scan data, and without it - an "open aperture" data. As it was shown in Ref. [3] the "open aperture" Z-scan is sensitive only to nonlinear absorption, while the "closed aperture" Z-scan provides measurement of a nonlinear refraction together with nonlinear absorption. Division of the "closed" by the "open aperture" data sets can give a result that depends only on the nonlinear refraction. The typical curve for nonlinear refraction exhibits 'peak' - the increase of the laser intensity transmitted through aperture and 'valley' - the lowering of the intensity. In Ref. [3] it was shown that the difference between the "peak" and the "valley" normalized transmittance  $\Delta T_{p-v}$  can provide information on the value of the real part  $\chi_{real}^{(3)}$  of the third order nonlinear susceptibility. The real part  $\chi_{real}^{(3)}$  can be obtained as [3]:

$$\chi_{real}^{(3)} = \frac{cn_0^2}{160\pi^2} \gamma \quad (1.14)$$

$$n_2 = \frac{n_0 c}{4\pi} \gamma \quad (1.15)$$

here  $c = 3 \cdot 10^{10}$  cm/s is the velocity of light in vacuum,  $n_0$  is a linear refraction index in the sample, and  $\gamma = \Delta n/I$  is a nonlinear refractive coefficient, where  $I$  is the light intensity in the focal point and  $\Delta n$  is connected with  $\Delta T_{p-v}$  as:

$$\Delta n = \frac{\sqrt{2}\lambda}{2\pi L_a} \frac{\Delta T_{p-v}}{0.406(1-S)^{0.25}} \quad (1.16)$$

here  $L_a$  is the effective interaction length,  $L_a = \alpha^{-1} (1 - \exp(-\alpha L))$ , where  $\alpha$  is a linear absorption coefficient (if any) of the sample with length  $L$ , and  $S$  is an normalized aperture size and  $\lambda$  is the wavelength of pump laser beam.

As an example of the sensitivity and application of this technique we will describe our experiments on investigation of nonlinearity of LiF crystal with  $F_2^-$  color centers (CC). Lithium fluoride crystal with  $F_2^-$  color centers (CC) is known as a laser crystal for 1.08 - 1.28  $\mu\text{m}$  spectral range operation and a nonlinear saturable absorber for neodymium lasers with 1.06  $\mu\text{m}$

wavelength. Our earlier investigation of nonlinearity in LiF:F<sub>2</sub><sup>-</sup> CC crystal was done using degenerate four wave mixing technique with the control of efficiency and quality of phase conjugation [4].

Here we describe the results on investigation of nonlinear refraction coefficient in LiF:F<sub>2</sub><sup>-</sup> color center crystal using Z-scan technique under irradiation with picosecond Nd<sup>3+</sup>:YAG laser. Electro-optically Q-switched and passively mode locked YAG:Nd laser (1064 nm) with pulse duration 35 ps and 10 Hz repetition rate was used as a light source in picosecond experiments. The laser beam was focused into LiF:F<sub>2</sub><sup>-</sup> CC samples 20 mm long with various initial transmission. The data sets of the "closed" by the "open aperture" measurements and the result of the division of the "closed" by the "open aperture" data for CC crystal with T<sub>o</sub>(1064 nm) = 40%, absorption coefficient  $\alpha_{1064} = 0.48 \text{ cm}^{-1}$  and pump pulse energy 5.5  $\mu\text{J}$  are shown in the Fig.1.4. It exhibits behavior typical to nonlinear medium with a positive third order nonlinearity, resulting in self focusing. The value of the real part of nonlinear susceptibility estimated from the unsaturated data was found to be  $\chi_{\text{real}}^{(3)} = 1.6 \times 10^{-11}$  esu in the above crystal. It was found that this value linearly depends on the concentration of F<sub>2</sub><sup>-</sup> CC and remains 10-20 times higher than that in pure LiF host material (Table 1.1). The positive nonlinear susceptibility can be described due to CC resonant nonlinearity.

SRS as a nonlinear process requires a high pump intensity to achieve SRS threshold and to obtain significant conversion efficiency. So in some cases it can be accompanied by other nonlinear processes. Previously it was shown that SRS of picosecond laser pulses in Ba(NO<sub>3</sub>)<sub>2</sub> crystal results in a wide cone of a scattered and pump light that was not observed with nanosecond pump previously [5]. As it was found in Ref. [6] the phase or transverse relaxation time T<sub>2</sub> of A<sub>g</sub> Raman mode at room temperature equals to 35 ps. Due to so long response time and delay, the use of a picosecond Nd<sup>3+</sup>:YAG pump laser results in a transient behavior of SRS. The threshold intensity of a transient SRS is higher than that for a steady state regime and depends on the ratio of the pump pulse duration and the phase relaxation time. It was found that for Nd<sup>3+</sup>:YAG pump laser with pulse duration 25 ps in order to reach the threshold conditions intensity must be increased ten times with respect to a steady state regime [5]. This results in the stimulation of fast accompanying nonlinear processes like self-focusing or some other with a quick response. The nonlinear change of the material refractive index due to high pump intensity can effectively be investigated with "Z-scan" technique.

A Q-switched and mode locked Nd:YAG laser (1064 nm) with a pulse duration of  $35 \pm 5$  ps and a repetition rate of 10 Hz was used as a light source in our Z-scan experiments. The spatial profile of the laser output in the far field was checked to be almost Gaussian. The beam was focused to provide a beam waist with the radius  $\omega_0 = 65 \mu\text{m}$ . The  $\text{Ba}(\text{NO}_3)_2$  crystal, 20 mm long, was placed on a positioning stage with a linear stepper motor driver controlled by a microprocessor system. A dichroic filter with high transmission at laser wavelength reflected all Stokes scattering radiation at the outlet of the crystal. A removable 50% transmittance aperture was placed in the far field in front of a photodiode.

By scanning the sample we analyzed the transmission of laser beam with picosecond pulse duration. When the crystal was close to the focal position and pump intensity was high the laser radiation was scattered into the Stokes components due to SRS process and reduction of transmitted beam was observed. Fig. 1.5(a) shows a normalized transmittance data without and with 50% aperture. The well in the upper curve corresponds to the SRS process which was observed visually in the scattered light. The "apertured" curve exhibit different behavior due to the sum of two nonlinear processes. The normalized result of the ratio of two data sets is presented at Fig. 1.5(b). It exhibits a behavior typical to a nonlinear medium with the positive third order nonlinearity resulting in a self-focusing of the pump beam.

Three sets of experimental data with the incident pulse energies of 0.021, 0.043 and 0.05 mJ results in a different change of refractive index values  $\Delta n$ :  $1.99 \cdot 10^{-6}$ ,  $4.47 \cdot 10^{-6}$  and  $4.98 \cdot 10^{-6}$ , correspondingly. The value of the real part of nonlinear susceptibility obtained from the above experiments was calculated to be  $\chi_{\text{real}}^{(3)} = (0.18 \pm 0.02) \cdot 10^{-13}$  esu.

This value corresponds to fast nonresonant electronic susceptibility energetically far from two photon Raman transition and practically without income from vibration nonlinearity because of short pump pulse duration  $\tau_{\text{pump}} \sim T_2$ . It is necessary to note that the nonlinearity of refractive index in barium nitrate crystal was observed only under irradiation with picosecond pulses. This can be due to higher threshold of pump intensity required to observe SRS. At the same time an electronic nature of a proposed nonlinear susceptibility is characterized by the short relaxation times of the excitation.

1. R. Adair, L. L. Chase, S. Payne, Nonlinear refractive index of optical crystals, Phys. Rev. B, **39**, 3337 (1989).
2. P. G. Zverev, J. T. Murray, R. C. Powell, R. J. Reeves, and T. T. Basiev, "Stimulated Raman scattering of picosecond pulses in barium nitrate crystals," Opt. Comm. **97** 59-64 (1993).

3. M. Sheik-Bahae, A. A. Said, T. H. Wei, D. J. Hagan, and E. V. Van Stryland, "Sensitive measurement of optical nonlinearities using a single beam," *IEEE J. Quantum. Electron.*, **QE-26**, 760-769 (1990).
4. T. T. Basiev, P. G. Zverev, S. B. Mirov, and S. Pal, *Proceedings of the SPIE 1500*, 65 (1991).
5. P. G. Zverev, J. T. Murray, R. C. Powell, R.J.Reeves, T.T.Basiev. "Stimulated Raman scattering of picosecond pulses in barium nitrate crystals." *Optics Commun.*, **97** (1993) 59.
6. P. G. Zverev, W. Jia, . Liu, T. T. Basiev, "Vibrational dynamic of Raman-active mode in barium nitrate crystal", *Optics Lett.*, **20** (1995) 2378.

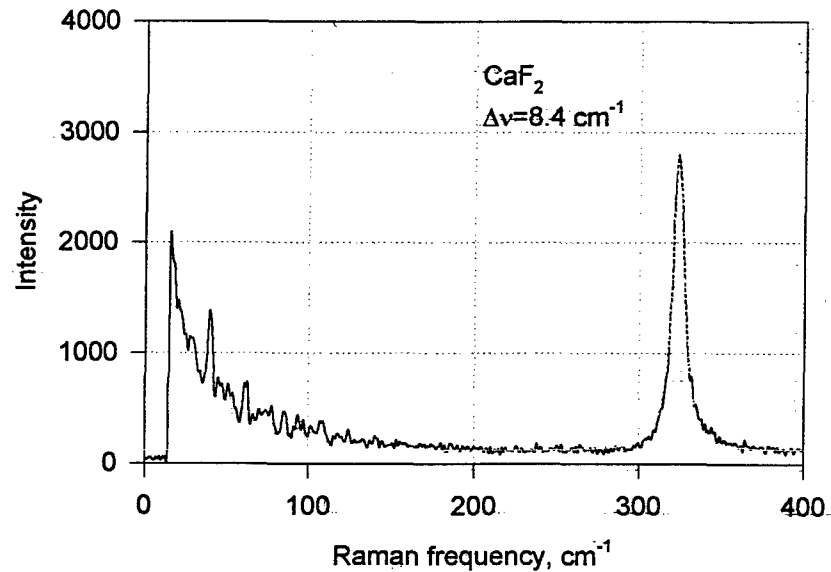


Fig. 1.1. Spontaneous Raman spectra of CaF<sub>2</sub> crystal

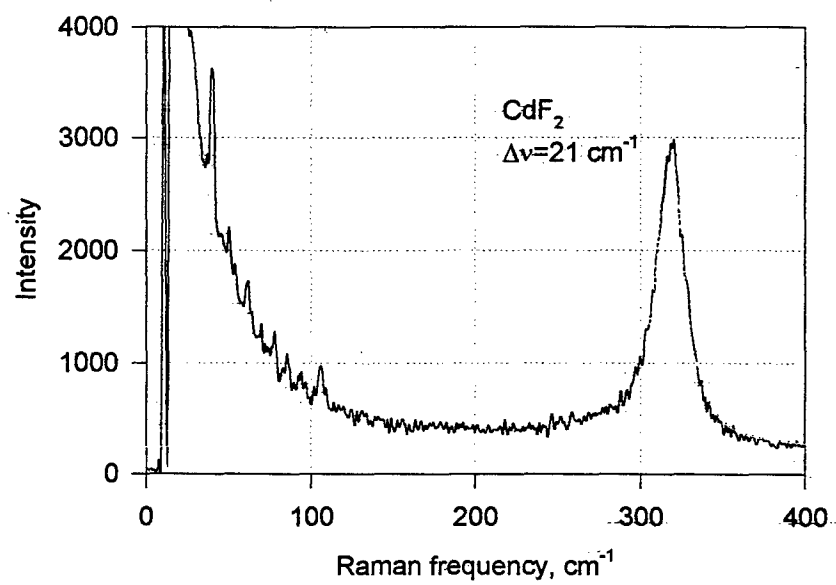


Fig. 1.2. Spontaneous Raman spectra of CdF<sub>2</sub> crystal.

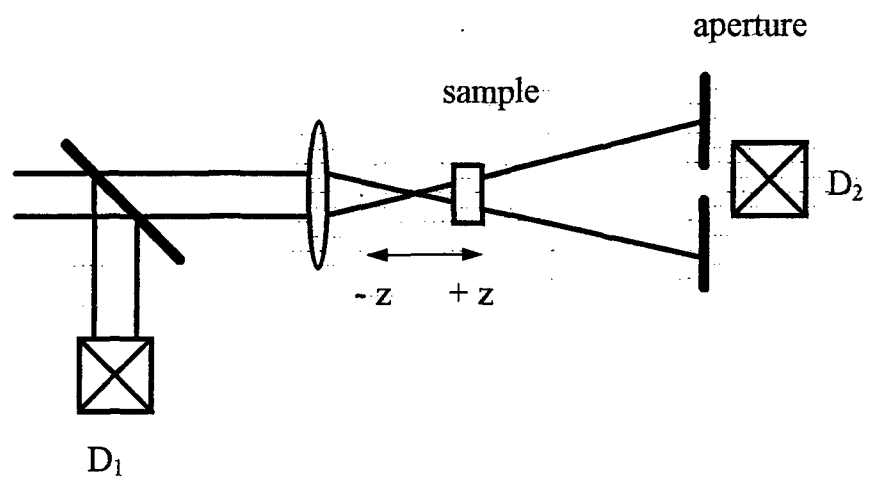


Fig. 1.3. Typical experimental setup for 'Z-scan' measurements.

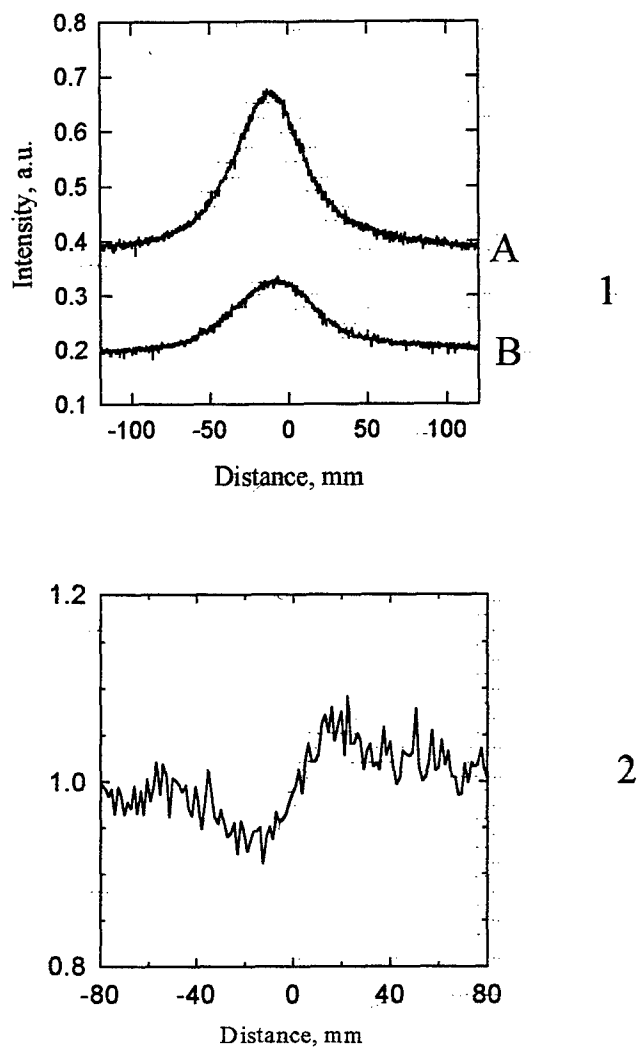


Fig.1.4. 'Z-scan' intensity dependence of transmitted laser light through  $\text{LiF:F}_2^-$  color center laser with 'open' (A) and 'closed aperture' (50% transmission) (B). The normalized result of division of the 'closed' by the 'open aperture' data sets. The behavior is typical to the medium with self focusing properties.

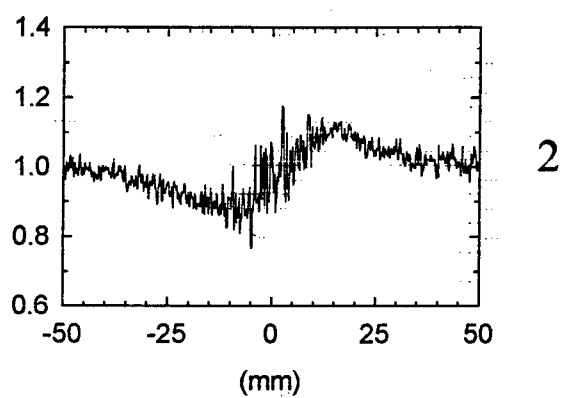
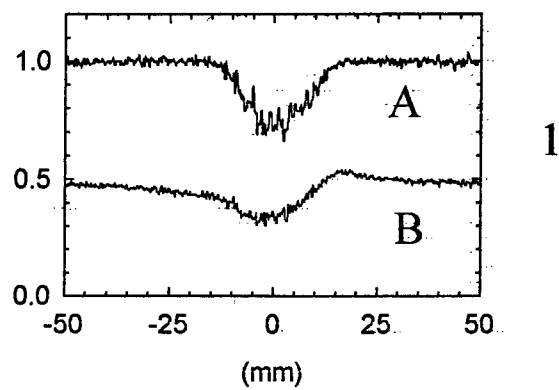


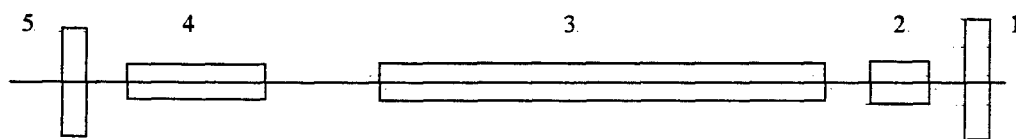
Fig. 1.5. 'Z-scan' in Ba(NO<sub>3</sub>)<sub>2</sub> crystal. "Open" (A) and "closed" (B) aperture normalized transmission of Ba(NO<sub>3</sub>)<sub>2</sub> crystal (1) and the result of division of the "closed" by the "open" aperture data sets (2).

## 2. Optimization of the Raman Laser Intracavity Pumping

Like other nonlinear processes, such as second harmonic generation, intracavity Raman lasers provide an effective means for shifting the frequency and enhancing both brightness and efficiency of solid-state lasers. Specifically, intracavity Raman lasers can be used to generate intense pulses of light that are Stokes shifted from the pump laser frequency, to produce very short output pulses, to provide high quantum conversion efficiency into the shifted frequencies, to serve as a power limiter to protect the damage of the pump laser gain medium and intracavity optics, to yield Stokes frequency shift output with low beam divergence [1-5].

Intracavity Raman laser includes Raman active media placed inside the pump laser cavity. Pump laser can be with active or passive Q-switching. To provide the highest conversion efficiency pump laser mirrors must be HR at the pump wavelength. Cavity mirrors can have special dichroic coatings to provide consequent oscillation at the first or the second or the third Stokes components.

Let's consider the optical cavity consisting of YAG:Nd active media, nonlinear Raman crystal and two mirrors one of which is totally reflecting for both the fundamental 1.064  $\mu\text{m}$  and Raman shifted radiation and the second is totally reflecting for 1.064  $\mu\text{m}$  radiation and is partially transmitting for Raman shifted radiation with longer wavelength. This scheme shown in Fig.2.1 models the intracavity pumped Raman laser. The temporal behavior of the



1. Totally reflecting mirror for both basic 1.064  $\mu\text{m}$  and Raman shifted radiation.
2. Q-switching element
3. YAG:Nd active medium.
4. Nonlinear Raman crystal.
5. Output mirror totally reflecting at 1.064  $\mu\text{m}$  and partially transmitting at Stokes wavelength.

Fig. 2.1.

system can be described by the set of differential equations as follows:

$$\begin{aligned}\frac{dn_3}{dt} &= n_0 W_{14} - n_3 \left( W_{32} + \frac{1}{\tau_3} + \sigma_{32} J \right) \\ \frac{dJ}{dt} &= \left[ \sigma_{32} n_3 - (g_R l_s J_s + \beta_{pas}) \right] c J \\ \frac{dJ_s}{dt} &= \left[ g_R l_s J - (\beta_{pas} + \beta_{us}) \right] c J_s,\end{aligned}$$

The numerical calculation of the mentioned system gives the temporal behavior of Raman gain in nonlinear crystal, temporal development of pump and Stokes pulses and can be applied to define the influence of such system parameters as cavity length, useful losses and Raman gain coefficient on the intensity, width and shape of the output Stokes pulse.

For convenience the above mentioned system of differential equations can be modified by averaging along the resonator length with substituting the population of the energy levels involved by gain coefficients:

$$\begin{aligned}\frac{dK_U}{dt} &= K_0 W_{14} - K_U \left( W_{14} + \frac{1}{\tau_3} + \sigma_{32} J \right) \\ \frac{dJ}{dt} &= \left[ K_U - (g_R l_s J_s + \beta_{pas}) \right] \frac{1}{t_{rez}} J \\ \frac{dJ_s}{dt} &= \left[ g_R l_s J - (\beta_{act} + \beta_{pas}) \right] \frac{1}{t_{rez}} J_s\end{aligned}$$

where  $K_u = n_3 \sigma_{32} l$  is the gain coefficient,  $K_0 = n_0 \sigma_{32} l$  is the maximum attainable gain coefficient taking place at the pump power enough to force all the available neodymium ions into radiative transitions,  $\sigma_{32}$  - emission cross section at 1.064  $\mu\text{m}$  lasing wavelength,  $l$  - the active medium length,  $\tau_{rez} = L/c$  - the photon cavity round trip time,  $L$  - cavity length,  $l_s$  - the length of  $\text{Ba}(\text{NO}_3)_2$  nonlinear crystal. The typical data for  $\text{Nd}^{3+}$  ions in YAG used in the calculations are: neodymium concentration  $n_0 = 5 \times 10^{19} \text{ cm}^{-3}$ , metastable level lifetime  $\tau_3 = 2.5 \times 10^{-4} \text{ s}$ , effective emission cross section at 1.064  $\mu\text{m}$  wavelength transition  $\sigma_{32} = 8.8 \times 10^{-19} \text{ cm}^2$ . The parameters of the cavity are assumed as follows: resonator length -  $L = 40 \text{ cm}$ , the active medium length -  $l = 10 \text{ cm}$ , the reflectivity of the output coupler -  $r = 30\%$ . The  $\text{Ba}(\text{NO}_3)_2$  crystal of the length of 5 cm and Raman gain coefficient of 11 cm/GW is supposed to be inserted in the cavity.

Assuming that at the starting time point the losses introduced into the cavity by Q-switch are very large (the Q-switch is closed) and the oscillations can not start ( $J=0$ ) equations are solved for the active medium gain increase due to flash lamp optical pumping ( $t_p = 100 \mu\text{s}$ ). At the next stage the pumping is set to zero ( $W_{14}=0$ ) and the intracavity losses are stepwise decreased (Q-switch is opened) so that oscillations can start ( $J \neq 0$ ). Then the

first equation describes the gain coefficient behavior  $K_u$ , the second - laser oscillations at  $1.064 \mu\text{m}$ , which play the role of intracavity pump for nonlinear crystal and the third - the interaction of the intracavity pump with the  $\text{Ba}(\text{NO}_3)_2$  Raman crystal.

The results of numerical calculation in approximation that intracavity passive losses are constant and equal to 5% are shown in the following Figs. All the modeled pulse dependencies are normalized on the maximum of intracavity pump  $I_{p \text{ in}}$ . The temporal behavior of intracavity pump  $1.064 \mu\text{m}$  radiation (dashed line) and intracavity Raman shifted Stokes radiation at  $1.197 \mu\text{m}$  wavelength (solid line) are presented at Fig.2.2. The output pulse of Stokes radiation is shown in Fig. 2.3.

1. P. G. Zverev and T. T. Basiev, "Barium nitrate Raman laser", *J. de Physique IV*, col.C4, 4, (1994) C4-599.
2. P. G. Zverev, T. T. Basiev, I. V. Ermakov, A. M. Prokhorov, "Stimulated Raman scattering in barium nitrate crystal in the external optical cavity", in *Laser Methods of Surface treatment and Modification*, SPIE - The International Society for Optical Engineering, 2498 (1994) 164.
3. T. T. Basiev, V. B. Sigachev, M. E. Doroshenko, P. G. Zverev, V. V. Osiko, A. M. Prokhorov, "Passive Q-switching of  $1.3 \mu\text{m}$  Nd-lasers with  $\text{Nd}^{2+}:\text{SrF}_2$  and  $\text{V}^{3+}:\text{YAG}$  crystalline saturable absorbers and application to Raman shifting to eye-safe region", in *Laser Methods of Surface treatment and Modification*, SPIE - The International Society for Optical Engineering, 2498 (1994) 171.
4. J. T. Murray, R. C. Powell, N. Peyghambarian, et al. "Generation of  $1.5 \mu\text{m}$  radiation through intracavity solid-state Raman shifting in  $\text{Ba}(\text{NO}_3)_2$  nonlinear crystals", *Opt. Lett.*, 20 (1995) 1017.
5. J. T. Murray, R. C. Powell, N. Peyghambarian, et al. "Eye-safe solid-state intracavity Raman laser", *Proceedings of Advanced Solid-State Lasers Conference*, B.H.Chai and S.A.Payne, eds. 24 (1995) 267.

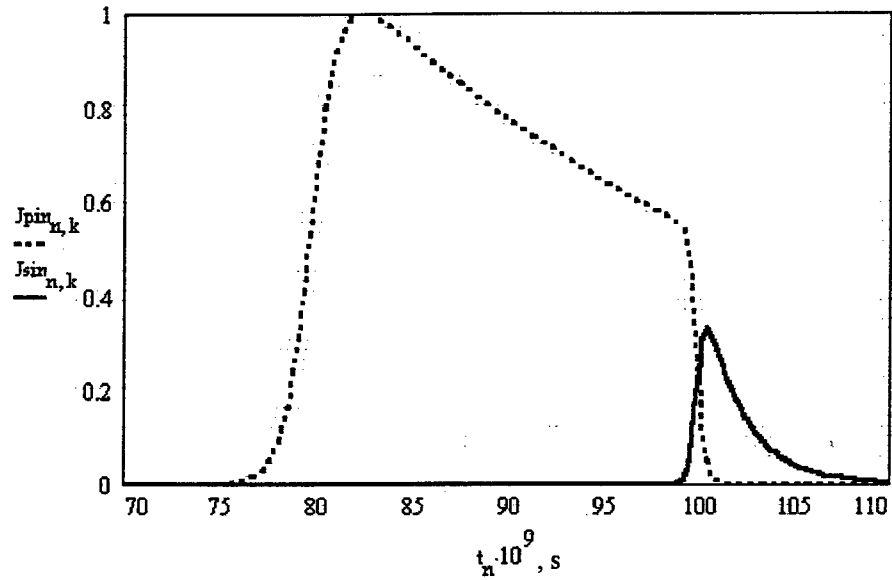


Fig. 2.2. Calculated temporal behavior of the intracavity pump pulse at 1.064  $\mu\text{m}$  wavelength (dashed line) and the SRS intracavity pulse (solid line) at 1.197  $\mu\text{m}$ .

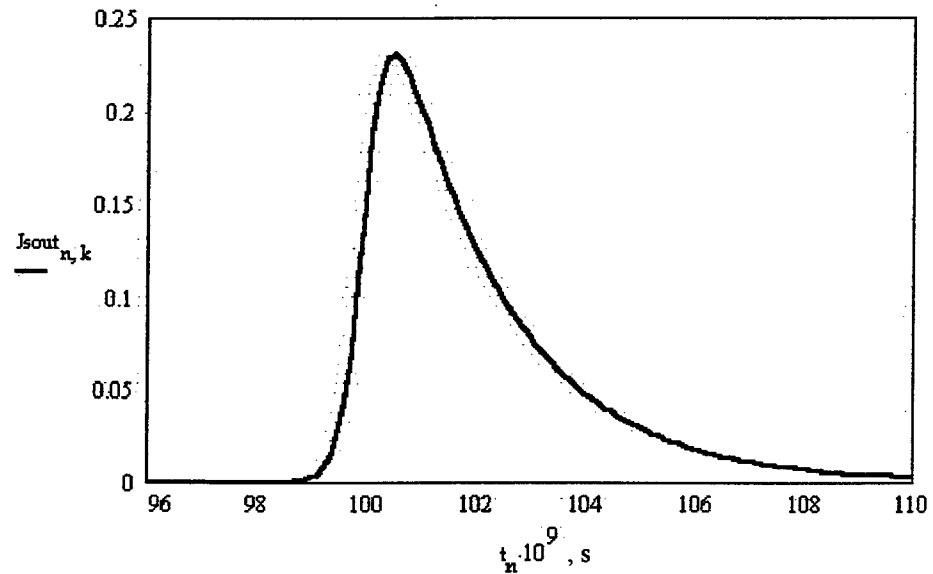


Fig. 2.3. The temporal behavior of the output Raman shifted Stokes pulse.

The influence of the cavity output mirror's reflectivity on the shape and width of the output pulse are shown in the Fig. 2.4. It can be seen from the Fig. 2.4 that the value of the output mirror reflectivity has a pronounced optimum for output mirror reflectivity about 30% though the half pulse width at half maximum has the tendency for constant grow with the increase of the output mirror reflectivity. The dependence of the temporal behavior of

the output SRS pulse on the value of Raman gain is shown in Fig. 2.5. The increase of Raman gain results in increase of the pulse intensity with simultaneous shortening of the pulse duration.

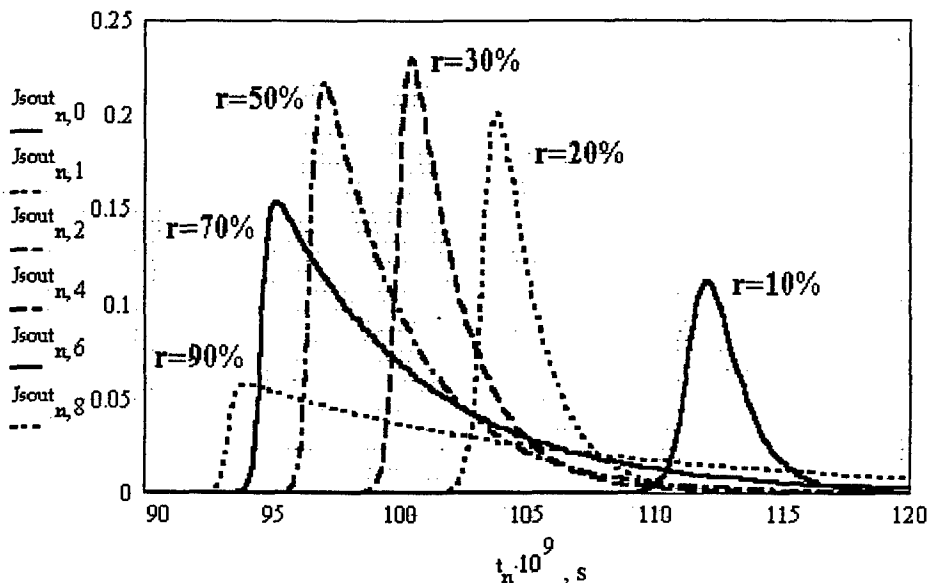


Fig. 2.4. The temporal behavior of the Raman shifted output pulse for different output mirror reflectivities .

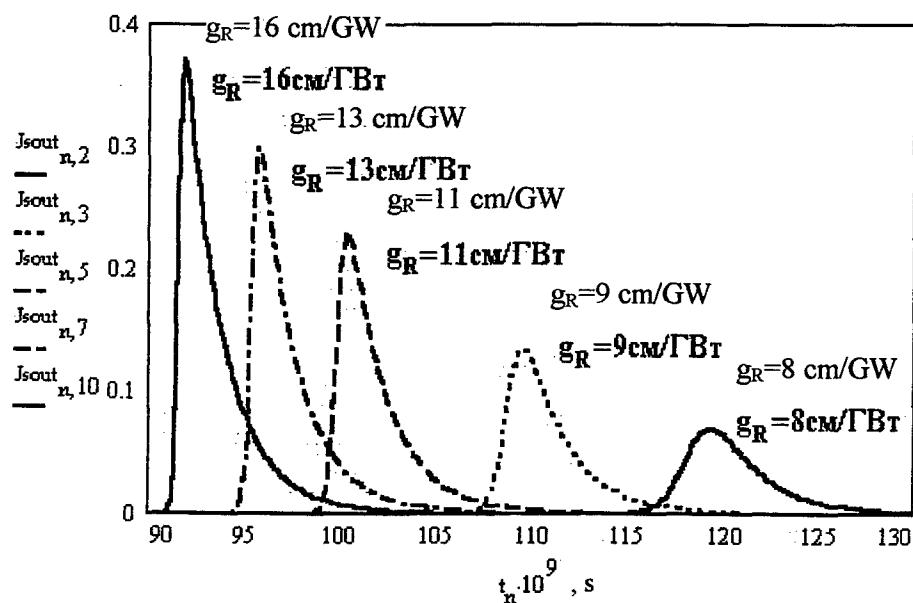


Fig. 2.5. The influence of Raman gain coefficient on the intensity and shape of output Raman shifted pulse

The dependence of the pulse width on the cavity length is presented in Fig. 2.6. For shorter resonator lengths the starting of SRS oscillations is observed earlier and the width of the pulse is decreased as can be seen in the figure.

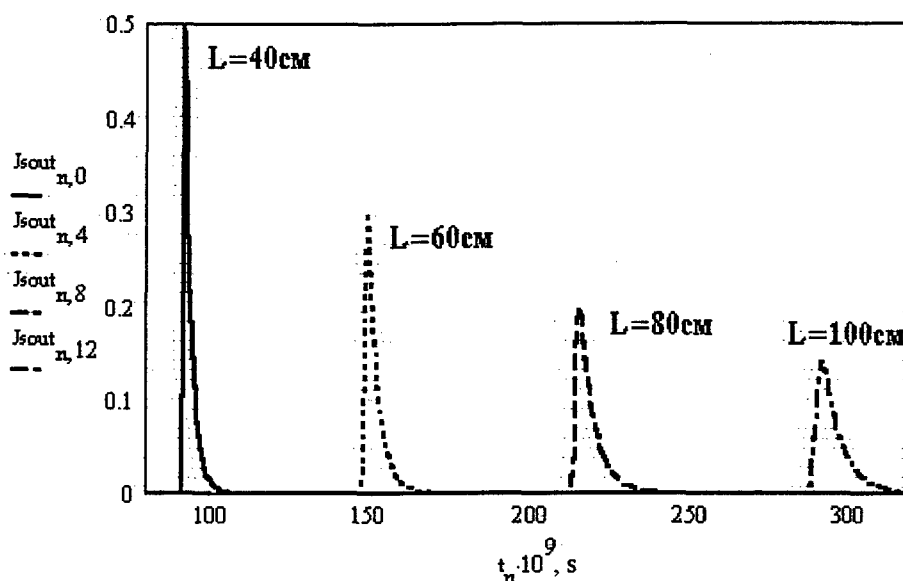


Fig.2.6. The calculated dependence of temporal behavior of the output Raman shifted pulse on the cavity length.

So the theoretical modeling of intracavity Raman laser showed that the intensity and width of the output pulse are influenced by parameters of the laser cavity and the Raman nonlinear media. The results of the modeling were checked experimentally, using the passively Q-switched YAG:Nd laser with  $\text{LiF:F}_2^-$  color center crystal as a saturable absorber. The initial transmittance of the saturable absorber was optimized during the Q-switch experiments to be 34%. The measured dependence of the output pulse shape and intensity on the value of the output mirror reflectivity is shown in Fig.2.7 for the cavity length of 70 cm. As was predicted by the theory the experimental dependence has a clearly seen optimum for output mirror reflectivity about 55% resulting in maximizing the pulse intensity and shortening the pulse width. The influence of the cavity length on the shape and intensity of the Raman shifted pulse is shown in Fig. 2.8. The modeled behavior of the pulse is proved by experimental observations, as the pulse intensity increases and its width decreases with the shortening of the cavity length.

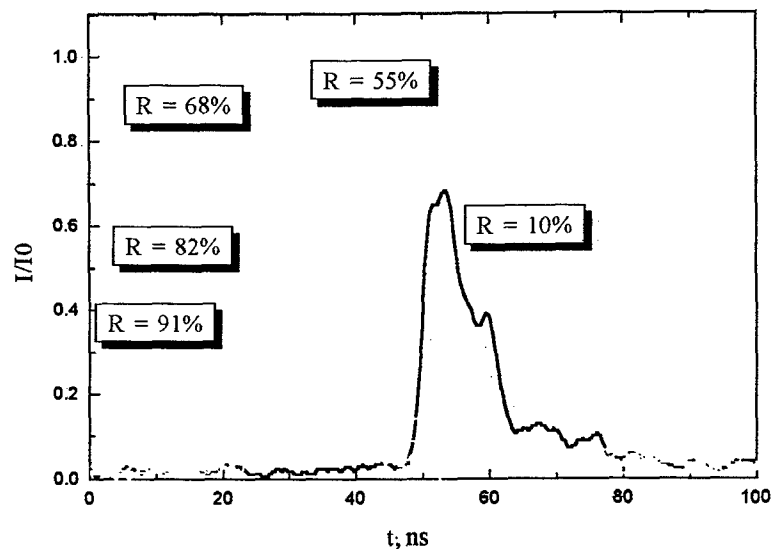


Fig. 2.7. Experimentally observed changes of the  $\text{Ba}(\text{NO}_3)_2$  Raman shifted output pulses for different output mirror's reflectivities under  $\text{LiF}:\text{F}_2^-$  passively Q-switched YAG:Nd intracavity laser pumping.

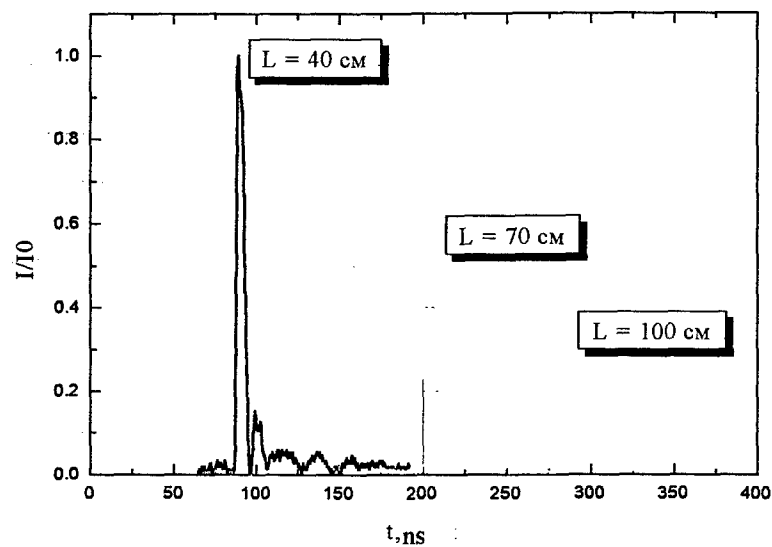


Fig.2.8. The observed influence of the cavity length on the temporal behavior of the output Raman shifted pulse.

Qualitative and quantitative agreement between results of rate equation calculations and experimental data of YAG:Nd -  $\text{Ba}(\text{NO}_3)_2$  intracavity pumped Raman laser systems proved the possibility to use this rate equation approach for calculation and optimization of solid-state Raman laser under intracavity pumping of high power iodine laser.

### 3. Spontaneous Raman spectroscopy of crystals.

#### 3.1. Experimental setup

The experiments on spontaneous Raman spectroscopy utilized two experimental setups. In the first one the excitation used a cw argon ion laser, working at 488 nm wavelength. The laser intensity at the sample was about 1 W. Raman spectrum was recorded by double-spectrometer "Spex-1403" in backwards scattering scheme. The spectral resolution of the system was  $0.2 \div 1.0 \text{ cm}^{-1}$ . The plasma discharge lines of argon laser were cut by an additional pre-monochromator. To compensate the self polarization of spectrometer, a polarization scrambler was placed in front of the entrance slit.

The second installation infrared Raman spectrometers was assembled to work in the infrared spectral region. It was based on IR SDL-1 double monochromator with S-1 photomultiplier and a powerful (0.5W) collimated CW diode laser ADLAS with temperature tuning and stabilization was assembled to measure IR Raman spectra with 812 nm wavelength pumping for narrow band gap material testing where argon and dye laser lines cannot be used due to strong band to band absorption. This installation successfully worked and provided the possibility to measure spontaneous Raman spectra in the samples which were not transparent in the visible spectral range. The main drawback of this setup was the very wide spectral width of the diode pump laser, which complicated the separation of closely located Raman lines.

For longer wavelengths the pumping with  $\text{Nd}^{3+}:\text{YLF}$  ( $\lambda_p = 1.047 \text{ }\mu\text{m}$ ) and  $\text{Nd}^{3+}:\text{YAG}$  ( $\lambda_p = 1.064 \text{ }\mu\text{m}$ ) was used. While the main problem in this case was connected with low sensitivity of photomultipliers in the IR. The best Raman spectra were obtained in the anti-Stokes Raman spectroscopy scheme where the pump beam wavelength  $\lambda_p$  corresponded to minimum sensitivity of S-1 photocathode and Raman scattered light has higher frequency and shorter wavelength, which corresponds to higher S-1 photocathode sensitivity. This spectrometer is based on DFS-12 high resolution double monochromator with S1 photocathode photomultiplier and the gated boxcar integrator PAR-162/164. Two Nd:YAG lasers ( $\lambda=1.064\mu\text{m}$ ), one with low repetition rate of 12.5 - 50 pulses per second and high peak power of about 1 MW, and the second with high repetition rate of  $10^4$  pulses per second and medium peak power of about 1 kW, were used. To improve sensitivity of the Raman shifted light registration, the third, Nd:YLF laser working at  $\lambda=1.047\mu\text{m}$  was used.

Single crystal as well as polycrystal samples were investigated in our experiments. To compare integral and peak scattering cross sections in different crystals the plane-parallel samples were made from single crystals with the thickness either 0.7 or 2 mm. An available diamond single crystal had slope facets and 0.7 mm thickness.

The exciting laser intensity and spectrometer slit width had constant values in different sets of measurements, focusing of exciting radiation and collimating of scattered light were the same in all the experiments. Since the Raman scattering was excited by a polarized beam, for some samples we made several experiments with different orientation of the sample crystallographic axes with respect to the direction of electrical vector  $E$  of the exciting beam. The conditions of the Raman scattering excitation of our measurements were very close to those of Raman lasers with longitudinal pumping.

The registered Raman spectra were analyzed with software fitting program which allowed to obtain values for Raman linewidth, peak and integral cross sections. The accuracy of the Raman linewidth was determined by the spectral resolution of the system and the widths of the slits. Except narrow lines ( $\Delta\Omega_R < 1 \text{ cm}^{-1}$ ), the spectral resolution was about 10% of the measured linewidth value.

The peak cross section value  $\Sigma_{peak}$  was measured with the accuracy of 10% for broad lines, while for narrow lines it became higher (~20%) due to spectral resolution limitation. While the accuracy for  $\Sigma_{int}$  was about 10% for narrow lines and increased to 20-40% due to uncertainty of the spectrum background level.

Since the diamond sample exhibited one of the most intensive Raman lines, the values of  $\Sigma_{int}$  and  $\Sigma_{peak}$  for other investigated materials were normalized to those of the diamond. In the following sections we will compare spontaneous Raman spectra and values of their integral and peak cross sections of different groups of perspective Raman materials.

### 3.2. Tungstate crystals

Potassium gadolinium tungstate  $\text{KGd}(\text{WO}_4)_2$  (KGW) is well known as an effective Raman material. It has  $(\text{WO}_4)$  molecular ionic complex which was found to exhibit SRS-active oscillations. Analogous properties can be found in other tungstate crystals with  $\text{Me}_x(\text{WO}_4)_y$  chemical formula. So the number of available tungstate crystals were included into our consideration.

KGW crystal doped with neodymium ions was proposed as Raman active material in 1985 [1, 2]. This crystal is also well known as a laser active material [3]. That's why an interesting way is to use it as a multi functional active element that is to obtain SRS in the matrix of laser active material. The previous investigation of crystallographic structure of KGW crystal showed that it has two independent directions  $n_m$  and  $n_g$  perpendicular to the optical axis. And for the radiation passing along the optical axis with polarization parallel to  $n_m$  the Raman frequency equals  $901 \text{ cm}^{-1}$ , while for radiation parallel to  $n_g$  it is  $767 \text{ cm}^{-1}$ . At 1064 nm pumping Raman gain was found to be the same for both lines  $6 \text{ cm/GW}$  that is 1.8 times smaller than that for  $\text{Ba}(\text{NO}_3)_2$  crystal. This was proved in the experiments on SRS of radiation from tunable color center laser [4], where SRS in  $\text{Ba}(\text{NO}_3)_2$  crystal has two times lower threshold and higher conversion efficiency (60%) than that in  $\text{KGd}(\text{WO}_4)_2$  crystal (30%). The possibility to switch the Raman shift from  $767 \text{ cm}^{-1}$  to  $901 \text{ cm}^{-1}$  by rotating polarization of the pump beam was demonstrated in [5].

Authors of [1] observed simultaneous laser and SRS oscillation in pulsed periodic nanosecond laser baser on  $\text{KGd}(\text{WO}_4)_2$  doped with  $\text{Nd}^{3+}$  ions. The laser resonator was formed by an HR plane mirror and an output coupler with 50% or 70% reflectivity at 1067 nm wavelength. Solid state phototrop filter based on gallium-scandium-gadolinium garnet doped with chromium was used as a passive Q-switch. At 25 J pumping to flash lamp the oscillation at 1067 nm was obtained with 7.5 ns time duration and energy 18 mJ. The duration of Stokes shifted 1180 nm radiation was 2.5 ns.

Simultaneous operation of  $\text{Nd}^{3+}:\text{KGd}(\text{WO}_4)_2$  and  $\text{Nd}^{3+}:\text{KY}(\text{WO}_4)_2$  crystals as laser active elements and SRS converters in picosecond time scale was demonstrated in [6]. Stable oscillation of 7-9 picosecond pulses in the train were observed in both laser media under 18 J flash lamp pumping. The average pulse energy in a single mode regime was 5 mJ and of each pulse - about 0.6 mJ. SRS oscillation was observed simultaneously with the laser pulses. The authors analyzed the temporal shape of the scattered light and ratio between Stokes and laser pulse energies with respect to the number of the pulse in the train. In the beginning of the train the duration and

efficiency of the first Stokes component was 6 ps and 2.5% while in the middle of the pulse the duration of the first Stokes was reduced to 1 ps and conversion efficiency was increased up to 40%. For shorter pulses second and third Stokes components oscillation with efficiencies 1.3% and 0.1% were observed. Thus, authors [6] showed that it is possible to choose the duration of the scattered light from 0.9 ps to 6.0 ps by selecting the appropriate pulse from the train. It was noted that because of the short transverse relaxation time this types of crystal can be successfully used for SRS of picosecond pulses.

Spontaneous Raman spectroscopy measurements allowed us to compare perspectives of different tungstate materials, to investigate their behavior at high temperatures, found phase transitions and predict dominant relaxation mechanisms of SRS-active modes.

### *Comparison of different tungstate crystals*

The first class where we were looking for promising crystals for powerful Raman lasers were tungstates. All investigated tungstates crystals can be divided into two groups: "simple" tungstates with scheelite structure of  $C_{4h}^6$  space symmetry, and "double" tungstates.

Raman spectra of "simple" tungstate crystals with one type of cations: calcium, strontium and barium are shown in Fig. 3.1. Each has one very intense  $A_{1g}$  line about 910 - 925  $cm^{-1}$  which corresponds to the internal symmetrical valent vibration in  $[WO_4]$  tetrahedron group. Table 3.1 shows data on internal Raman frequency shift and Raman mode linewidth in these crystals together with maximum frequency of external lattice mode at two temperatures.

From Table 3.1 follows that the increase of cation radius in the row  $Ca^{2+} \rightarrow Sr^{2+} \rightarrow Ba^{2+}$  results in the increase of internal vibronic mode frequency  $\Omega_R$  and decrease of its linewidth. In the first approximation the frequency of  $A_{1g}$  internal mode of tetragonal group must be determined by interactions inside the tetragonal groups [7]. The sort of cations ( $Ca^{2+}$ ,  $Sr^{2+}$ , or  $Ba^{2+}$ ) can influence on this  $A_{1g}$  frequency only by changing the size of the crystal unit cell and by covalence cation effect [7]. The moving on the series of tungstates  $Ca^{2+} \rightarrow Sr^{2+} \rightarrow Ba^{2+}$  increases the unit cell and interionic distance inside the molecular group. The degree of covalence bond between the cation and molecular group usually decreases within the series  $Ca^{2+} \rightarrow Sr^{2+} \rightarrow Ba^{2+}$ . These two factors must decrease the frequency of  $A_{1g}$  vibration for  $Sr^{2+}$  and  $Ba^{2+}$  in comparison with  $Ca^{2+}$ . As it was seen from Table 3.1 the opposite result was registered in our experiments. This anomalous phenomenon can be explained by decreasing of interaction between internal and external Raman modes in scheelite structure in the series of  $Ca^{2+} \rightarrow Sr^{2+} \rightarrow Ba^{2+}$  tungstates. Such interaction decreasing together with increasing internal Raman mode frequency  $\Omega_R$  and decreasing maximum

lattice mode frequency  $\omega_{lat}^{max}$  could be responsible for slowing down of dephasing processes and decreasing of homogeneous linewidth. The last feature is of special importance as it was shown above the steady state SRS gain coefficient is inversely proportional to the linewidth value. For the same value of integral Raman scattering cross section for Ca, Sr, and Ba tungstates, decreasing of the linewidth by the factor 2.2 will increase the peak scattering intensity and Raman gain coefficient by the same factor of 2.2.

Investigation of Raman spectra of simple tungstates at liquid nitrogen temperature showed that spectral profiles of these lines can be very well fitted by Lorentzian curve shape and their Raman linewidths were reduced by a factor of two (Table 3.1). At the same time the position of the line remains practically constant in this temperature range. This shows that for large  $Ba^{2+}$  ion the linewidth in tungstate is smaller than that for smaller  $Ca^{2+}$  - tungstate.

Table 3.1. Spectral parameters of Raman lines in "simple" tungstate crystals.

	Molecular group	$\Omega$ $cm^{-1}$		$\Delta\Omega$ $cm^{-1}$		$\omega_{lat}^{max}$ , $cm^{-1}$
		77	300	77	300	
CaWO <sub>4</sub>	WO <sub>4</sub>	910.18	910.27	3.63	6.95	274
SrWO <sub>4</sub>	WO <sub>4</sub>		921.5		3	240
BaWO <sub>4</sub>	WO <sub>4</sub>	924.3	924	0.97	1.63	194

The complex tungstate series includes cation substances with alkali (Na and K) and rare earth (TR = Gd, Y, Yb, Lu, etc.) ions such as NaTR(WO<sub>4</sub>)<sub>2</sub> and KTR(WO<sub>4</sub>)<sub>2</sub>. The NaTR(WO<sub>4</sub>)<sub>2</sub> crystals have sheelite structure similar to that of a "simple" tungstate. Statistical distribution of Na<sup>+</sup> and TR<sup>3+</sup> ions over the same lattice sites results in variation of [WO<sub>4</sub>] complex surroundings due to the tungstate lattice host distortions. This causes A<sub>1g</sub> Raman line inhomogeneous broadening up to 3-7 times larger than that in simple tungstates ( spectra of NaY(WO<sub>4</sub>)<sub>2</sub> and BaWO<sub>4</sub> in Fig. 3.2 ). The KTR(WO<sub>4</sub>)<sub>2</sub> tungstates series has a sheelite structure at temperature above 1000 °C. It transforms into the monoclinic structure with cooling. K<sup>+</sup> and TR<sup>3+</sup> ions occupy definite positions in the monoclinic tungstate ordered structure. Contrary to the sheelite structure,

the edge shared  $[\text{WO}_6]$  octahedrons form molecular groups in the monoclinic tungstates [8] with Raman spectra considerably different from those of sheelite tungstates. Two intensive Raman lines corresponding to  $[\text{WO}_6]$  complex vibrations in the spectra of monoclinic tungstates are registered (spectrum of  $\text{KGd}(\text{WO}_4)_2$  in Fig. 3.2).

As we have seen above the important parameter to characterize of SRS-active nonlinear material is the values of  $\Sigma_{peak}$  and  $\Sigma_{int}$ . The comparative data measured in all our experiments are presented in Table 3.2. Since the diamond sample exhibited one of the most intensive Raman lines, the values for other crystals were normalized to those of the diamond.

Since the steady state Raman gain coefficient is defined by the peak cross section  $\Sigma_{peak}$  the highest gain after the diamond is expected to be in barium and sodium nitrate crystals. In spite the fact that the integral cross sections of SRS-active vibronic modes for nitrate Raman crystals are approximately 2 ÷ 3 times less than for tungstates,  $\text{Ba}(\text{NO}_3)_2$  and  $\text{NaNO}_3$  have high gain due to the narrowest SRS-active lines. Their linewidth values were measured in our experiments to be as small as  $\Delta\Omega_{\text{Ba}(\text{NO}_3)_2} \approx 0.4 \text{ cm}^{-1}$  and  $\Delta\Omega_{\text{NaNO}_3} \approx 1 \text{ cm}^{-1}$  at room temperature which are correspondingly 7 and about 2 times less than that in the diamond.

Authors [9] assigned narrow linewidth of SRS-active mode in  $\text{Ba}(\text{NO}_3)_2$  crystal to lower probability of vibronic relaxation due to the absence of the three phonon splitting relaxation process for this mode. The peak cross section  $\Sigma_{peak}$  of the Raman mode in  $\text{Ba}(\text{NO}_3)_2$ , measured in our experiments, exhibits high value (60% of that in the diamond), that is twice higher than in  $\text{KGd}(\text{WO}_4)_2$  crystal. Due to larger linewidth  $\text{NaNO}_3$  crystal has lower value of  $\Sigma_{peak}$  of only 44 %. Natural calcite demonstrates a smaller value of  $\Sigma_{peak}$  that is only about 10%.

Both "simple" sheelite tungstate crystals such as  $\text{M}(\text{WO}_4)$  (here M is Ca, Sr, or Ba) and «complex» monoclinic tungstates  $\text{KTR}(\text{WO}_4)_2$  have high integral Raman scattering cross section  $\Sigma_{int}$ . But due to larger spectral broadening 5,4 ÷ 15  $\text{cm}^{-1}$  complex tungstates exhibit lower values of peak cross sections from 8% to 29% depending on the crystal and orientation. For our experiments crystals of  $\text{SrWO}_4$  and  $\text{PbWO}_4$  tungstates were not available as a bulk single crystal for comparative intensity measurements and we prepared them in powder form. Due to the narrow linewidth in  $\text{SrWO}_4$  crystal (Table 3.2) one can predict values of  $\Sigma_{peak}$  as high as 30% in this material which is higher than in other tungstates and closer to those in nitrates. The peak Raman scattering cross section  $\Sigma_{peak}$  measured in  $\text{BaWO}_4$  crystal equals to 52% of that in diamond, that is close to values observed in  $\text{Ba}(\text{NO}_3)_2$  crystal and much higher than those in  $\text{KGd}(\text{WO}_4)_2$  crystal.

Integral cross sections for 900 and 770  $\text{cm}^{-1}$  lines in double tungstates are quite high (about 50% those of diamond), but their line broadening is big (5 - 20  $\text{cm}^{-1}$ ). That is why the peak cross section is not as high as that of nitrates. A way to improve this is to find, synthesize, and study a tungstate crystal with a very small line broadening at room temperature. During the reported period we synthesized and studied a number of tungstates and found out among them crystals with high frequency isolated Raman lines:  $\text{LiIn}(\text{WO}_4)_2$  and  $\text{NaIn}(\text{WO}_4)_2$ . The first crystal was synthesized in polycrystalline form and the second one was grown as a single crystal.

As one can see from Fig. 3.3 and Table 3.2,  $\text{LiIn}(\text{WO}_4)_2$  crystal exhibits one high intensive Raman line at a high frequency of 920  $\text{cm}^{-1}$  and a pair of low frequency lines at  $\nu = 75$  and 95  $\text{cm}^{-1}$ . Unfortunately, the spectral broadening of the high frequency Raman line with  $\nu_R = 920 \text{ cm}^{-1}$  is not very small ( $\Delta\nu_R = 8 \text{ cm}^{-1}$ ) and even a little higher than  $\Delta\nu_R = 5.4 \text{ cm}^{-1}$  of  $\text{KGd}(\text{WO}_4)_2$  crystal (see Table 3.2). For this reason we can expect a lower peak cross section for steady state stimulated Raman scattering in this material. Different features are shown by  $\text{NaIn}(\text{WO}_4)_2$  single crystal. Its Raman spectra demonstrates an intensive isolated vibronic Raman line at the highest for tungstate series frequency  $\nu = 977 \text{ cm}^{-1}$  and a couple of less intensive low frequency peaks at 93  $\text{cm}^{-1}$  and 130  $\text{cm}^{-1}$  (Fig. 3.4). All the three lines show a strong polarization dependence and very small spectral line broadening of  $\sim 1.4 \text{ cm}^{-1}$  at room temperature, which is much smaller than that for  $\text{KGd}(\text{WO}_4)_2$  and  $\text{LiIn}(\text{WO}_4)_2$  crystals (see Table 3.2). This feature of the  $\text{NaIn}(\text{WO}_4)_2$  crystal allows us to expect the stimulated Raman scattering peak cross section of this material to be several times higher in comparison with the well known  $\text{KGd}(\text{WO}_4)_2$  Raman crystal.

1. A. M. Ivanuk, M. A. Ter-Pogosyan, P. A. Shaverdov, V. D. Belyaev, V. L. Ermolayev, H. P. Tikhonova. "Picosecond light pulses under intracavity stimulated Raman scattering in the active element of neodymium laser." *Optika i Spektroskopiya*, **59** (1985) 950 (in Russian).
2. K. Andryunas, Y. K. Vishchakas, V. Kabelka, I. V. Mochalov, A. A. Pavlyuk, G. T. Petrovskii and V. P. Syrus, "SRS-self conversion of  $\text{Nd}^{3+}$  laser emission in tungstate crystals" *JETP Lett.* **42** (1985) 410.
3. A. A. Kaminskii, S. E. Sarkisov, A. A. Pavlyuk, V. V. Lubchenko. "Anisotropy of luminescence properties of laser crystals  $\text{KGd}(\text{WO}_4)_2$  and  $\text{KY}(\text{WO}_4)_2$  with  $\text{Nd}^{3+}$  ions". *Neorganicheskie materialy*, **16** (1980) 720 (in Russian).
4. T. T. Basiev, V. N. Voitsekovskii, P. G. Zverev, F. V. Karpushko, A. V. Lubimov, S. B. Mirov, V. P. Morozov, I. V. Mochalov, A. A. Pavluik, G. V. Sinitsin, V. E. Yakobson, "Conversion of tunable radiation from a laser utilising an  $\text{LiF}$  crystal containing  $\text{F}_2^-$  colour centres by stimulated Raman scattering in  $\text{Ba}(\text{NO}_3)_2$  and  $\text{KGd}(\text{WO}_4)_2$  crystals," *Kvantovaya elektronika*, **14** (1987) 2452; *Sov. J. Quantum Electronics*, **17** (1987) 1560.
5. V. A. Berenberg, S. N. Karpukhin, I. V. Mochalov. "SRS of nanosecond pulses in  $\text{KGd}(\text{WO}_4)_2$  crystal". *Kvantovaya elektronika*, **14** (1987) 1849 (in Russian).

6. K. Andrunas, A. Barila, Yu. Vischakas, I. V. Mochalov, G. T. Petrovski, V. Syrus: "Temporal parameters of picosecond pulses under SRS self conversion of laser radiation." *Optika i Spektroskopiya*, **64** (1988) 397 (in Russian).
7. A.N. Lasarev, A.P. Mirgorodskii, and I.S. Ignatiev, „*Vibronic spectra of complex oxides*“, Leningrad: Nauka (1975) (in Russian).
8. Yu. K. Vishikov, I. V. Mochalov, A. V. Mikhailov, R. F. Klevtsova, and A. V. Lyubimov, „Crystal structure and Raman scattering in crystals of  $\text{KGd}(\text{WO}_4)_2$ “, *Litovskii fizicheskii journal*, **28**, 224-234 (1988).
9. P. G. Zverev, W. Jia, H. Liu, and T. T. Basiev, „Vibrational dynamic of the Raman-active mode in barium nitrate crystal“, *Opt. Lett.* **20**, 2378-2380 (1995).

Table 3.2. Spontaneous Raman scattering parameters of tungstate crystals.

Material	Lattice space group	Molecular group	Raman freq. $\Omega_R$ ( $cm^{-1}$ )	Raman line width $\Delta\Omega_R$ ( $cm^{-1}$ )	Integral cross section $\Sigma_{int}$ (a.u.)	Peak intensity $\Sigma_{peak}$ (a.u.)	Scattering geometry of excitation	
							K	E
Diamond	$O_h^7$		1332.9	2.7	100	100	//C <sub>3</sub>	$\perp$ C <sub>3</sub>
Ba(NO <sub>3</sub> ) <sub>2</sub>	$T_h^6$	[NO <sub>3</sub> ]	1048.6	0.4	21	63	//C <sub>4</sub>	//C <sub>4</sub>
CaWO <sub>4</sub>	$C_{4h}^6$	[WO <sub>4</sub> ]	910.7	4.8	47	18.6	$\perp$ C <sub>4</sub>	//C <sub>4</sub>
SrWO <sub>4</sub> *	$C_{4h}^6$	[WO <sub>4</sub> ]	921.5	3	-	-		
BaWO <sub>4</sub>	$C_{4h}^6$	[WO <sub>4</sub> ]	925	1.63	47	64	$\perp$ C <sub>4</sub>	//C <sub>4</sub>
PbWO <sub>4</sub> *	$C_{4h}^6$	[WO <sub>4</sub> ]	904	5.6	-	-	-	-
NaGd(WO <sub>4</sub> ) <sub>2</sub> *	-	-	919	14**	-	-	-	-
NaY(WO <sub>4</sub> ) <sub>2</sub> *	-	-	918	15**	-	-	-	-
Sc <sub>2</sub> (WO <sub>4</sub> ) <sub>3</sub> *	-	-	1024	15	-	-	-	-
In <sub>2</sub> (WO <sub>4</sub> ) <sub>3</sub> *	-	-	1023	13	-	-	-	-
NaIn(WO <sub>4</sub> ) <sub>2</sub> *	-	-	977	1.4	-	-	-	-
LiIn(WO <sub>4</sub> ) <sub>2</sub> *	-	-	920	8	-	-	-	-
NaSr(WO <sub>4</sub> ) <sub>2</sub> *	-	-	924	2.5	-	-	-	-
Na <sub>2</sub> WO <sub>4</sub> *	$O_h^7$		929.2	1.8	-	-	-	-
KGd(WO <sub>4</sub> ) <sub>2</sub>	$C_{2h}^6$	[WO <sub>6</sub> ]	901	5.4	54	25	$\perp$ C <sub>2</sub>	$\perp$ C <sub>2</sub>
--	--	--	901	5.4	43	22	$\perp$ C <sub>2</sub>	//C <sub>2</sub>
--	--	--	768	6.4	19	8.2	$\perp$ C <sub>2</sub>	$\perp$ C <sub>2</sub>
--	--	--	768	6.4	65	29	$\perp$ C <sub>2</sub>	//C <sub>2</sub>
KY(WO <sub>4</sub> ) <sub>2</sub>	--	--	905.6	7	50	24	$\perp$ C <sub>2</sub>	$\perp$ C <sub>2</sub>
--	--	--	905.6	7	45	22	$\perp$ C <sub>2</sub>	//C <sub>2</sub>
--	--	--	767.4	8.4	20	9	$\perp$ C <sub>2</sub>	$\perp$ C <sub>2</sub>
--	--	--	767.4	8.4	64	24	$\perp$ C <sub>2</sub>	//C <sub>2</sub>
KYb(WO <sub>4</sub> ) <sub>2</sub>	--	--	908	7.4	48	24	$\perp$ C <sub>2</sub>	$\perp$ C <sub>2</sub>
--	--	--	908	7.4	48	24	$\perp$ C <sub>2</sub>	//C <sub>2</sub>
--	--	--	757	15**	25**	13.8**	$\perp$ C <sub>2</sub>	$\perp$ C <sub>2</sub>
--	--	--	757	15**	70**	25**	$\perp$ C <sub>2</sub>	//C <sub>2</sub>

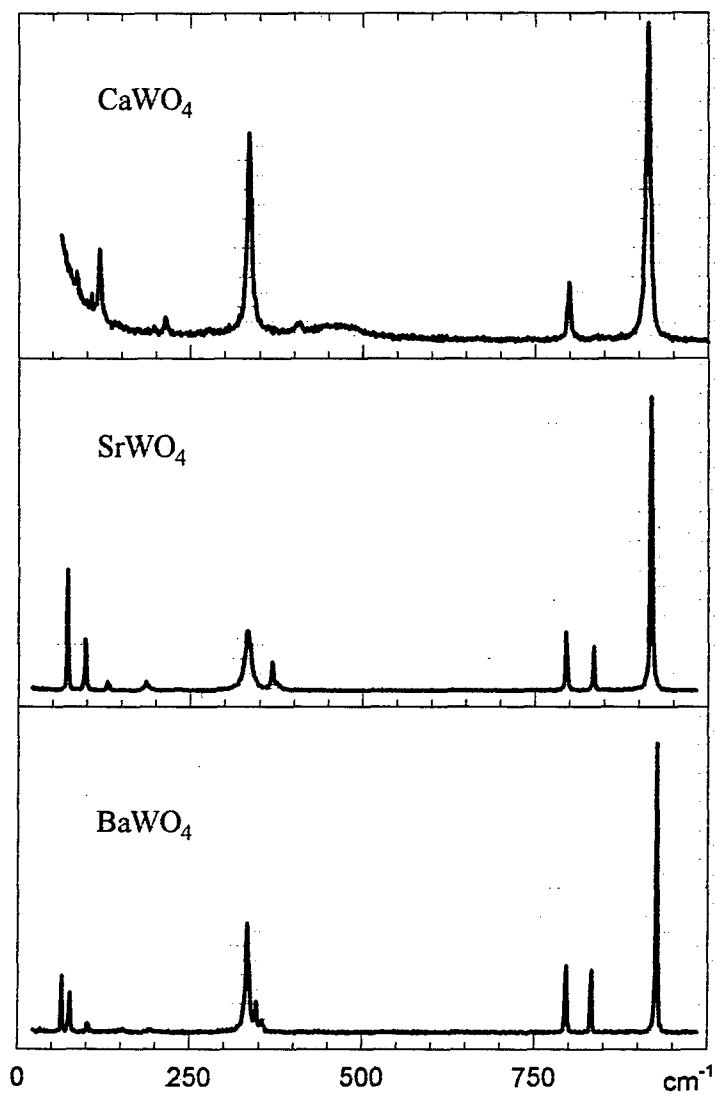


Fig. 3.1. Unpolarized spontaneous Raman spectra of "simple" tungstate crystals with sheelite structure:  $\text{CaWO}_4$  and  $\text{BaWO}_4$  single crystals, and  $\text{SrWO}_4$  powdered sample. The geometry of excitation for  $\text{CaWO}_4$  and  $\text{BaWO}_4$  samples was  $\mathbf{K} \perp C_4$ ,  $\mathbf{E} // C_4$ .

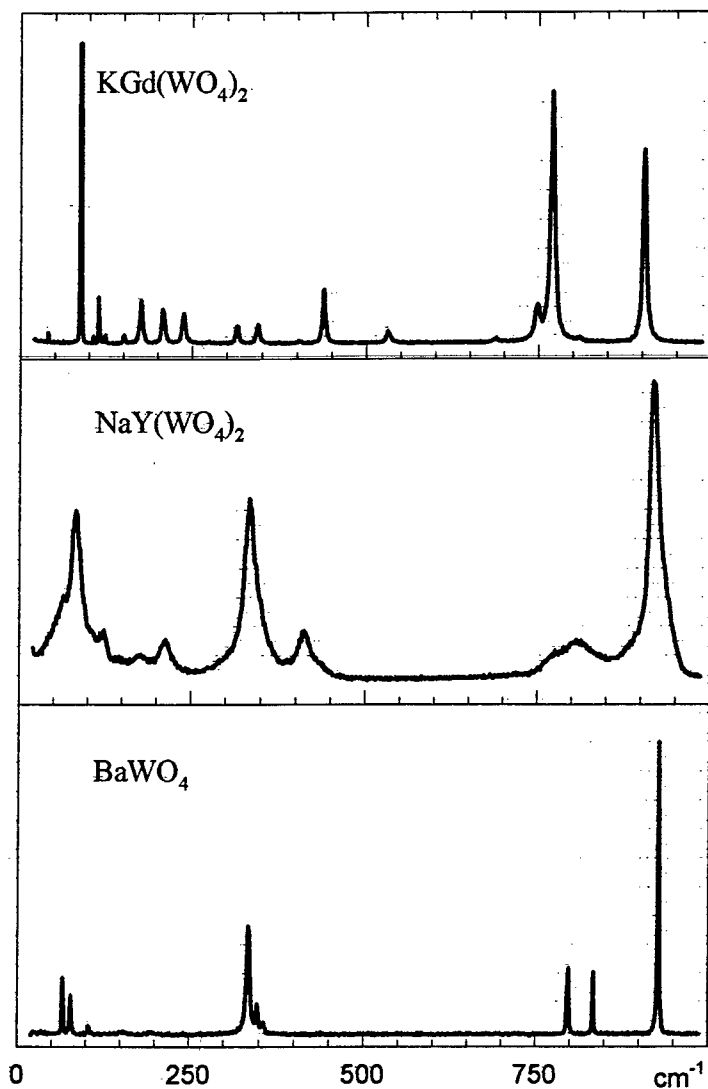


Fig. 3.2. Unpolarized spontaneous Raman spectra of tungstates. Spectrum of  $\text{NaY}(\text{WO}_4)_2$  disordered double tungstate has much broader Raman lines than  $\text{BaWO}_4$  due to inhomogeneous broadening. The Raman spectrum of  $\text{KGd}(\text{WO}_4)_2$  single crystal which has monoclinic structure is different from those of „simple“ tungstates and under geometry of excitation as  $\mathbf{K} \perp \mathbf{C}_2$ ,  $\mathbf{E} // \mathbf{C}_2$  exhibits two intensive lines at 767 and 901  $\text{cm}^{-1}$ .

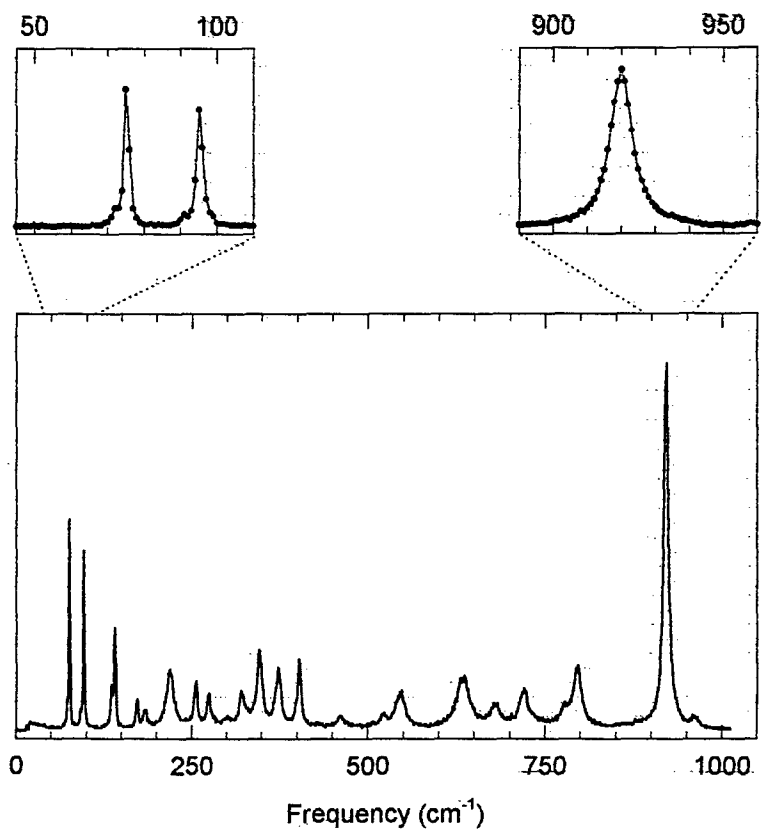


Fig. 3.3. Spontaneous Raman spectra of  $\text{LiIn}(\text{WO}_4)_2$  crystal

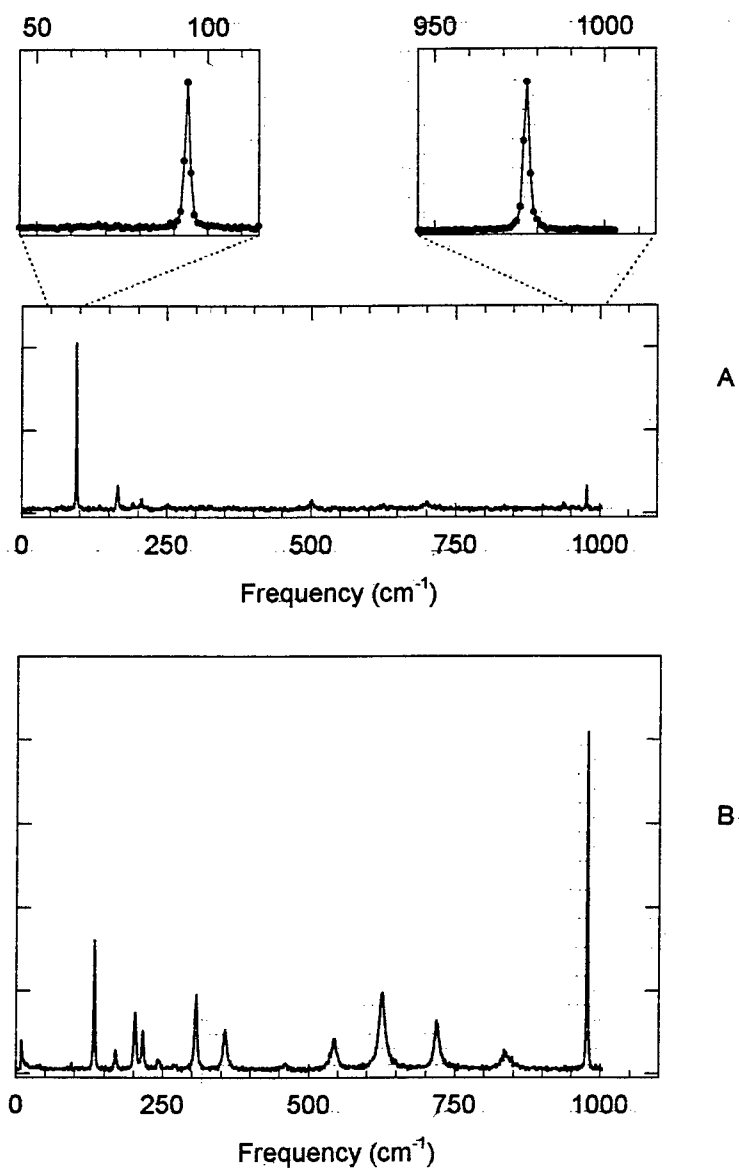


Fig. 3.4. Spontaneous Raman spectra of NaIn(WO<sub>4</sub>)<sub>2</sub> crystal.

### *Phase transitions in double tungstate crystals*

In order to find the best composition and modification the phase transitions in different double tungstate single crystals  $\text{KGd}(\text{WO}_4)_2$ ,  $\text{KYb}(\text{WO}_4)_2$ ,  $\text{KY}(\text{WO}_4)_2$ ,  $\text{NaGd}(\text{WO}_4)_2$ ,  $\text{NaLa}(\text{WO}_4)_2$ ,  $\text{NaY}(\text{WO}_4)_2$ , and  $\text{KLa}(\text{WO}_4)_2$ , have been studied by high-temperature Raman scattering (HTRS) technique.

According to [1], the lattice cell of  $\text{KGd}(\text{WO}_4)_2$  low-temperature modification is a base-centered  $C/2c$  ( $C_{2h}^6$ ) and contains 4 molecular units. As the unit cell has a multiplicity factor equal to 4, the calculation of the number of vibration modes was carried out in assumption of two molecular units in the lattice cell. Using data on position symmetry of atoms in  $\text{KGd}(\text{WO}_4)_2$  structure [1], the number and symmetry of vibration modes in this lattice should be defined as

$$\Gamma = 17A_g + 19B_g + 17A_u + 19B_u$$

As the  $C_{2h}^6$  lattice of interest has a center of inversion, the Raman spectra must contain only vibrations  $17A_g + 19B_g$ . To identify spontaneous Raman (SR) spectral lines for single crystals  $\text{KGd}(\text{WO}_4)_2$ ,  $\text{KYb}(\text{WO}_4)_2$ , and  $\text{KY}(\text{WO}_4)_2$ , the spectra were recorded on oriented single crystals in backward scattering geometry at 300 K. Polarization vectors of the exciting and scattered light were parallel to main axes of the optical indicatrix, that let us to avoid birefringence.

Fig. 3.5 shows polarized spontaneous Raman spectra of  $\text{KGd}(\text{WO}_4)_2$  single crystal, observed in geometry  $\mathbf{z}(\mathbf{yy})\mathbf{z}$  and  $\mathbf{z}(\mathbf{yx})\mathbf{z}$  at  $T=300\text{K}$ . The crystal is oriented so that y axes is parallel to the crystallographic axis [010] of the crystal. Similar Raman spectra were also recorded for  $\text{KYb}(\text{WO}_4)_2$  and  $\text{KY}(\text{WO}_4)_2$  single crystals.

We identified all  $17A_g$  and  $19B_g$  vibrations in three double tungstate crystals. The frequencies of these vibrations are given in Table 3.3. The presented data confirm that  $\text{KGd}(\text{WO}_4)_2$ ,  $\text{KYb}(\text{WO}_4)_2$ , and  $\text{KY}(\text{WO}_4)_2$  crystals have  $C_{2h}^6$  symmetry of the lattice cell, which was earlier determined only by X-ray diffraction analysis.

As one can see from Table 3.3, there are small variations in line frequencies with changing the sort of Ln cation in  $\text{KLn}(\text{WO}_4)_2$  crystal (Ln denotes either Gd, or Y, or Yb elements), usually within  $0 - 16 \text{ cm}^{-1}$ . However, in the high-frequency area ( $600 - 1100 \text{ cm}^{-1}$ ), which is characterized by the most intensive lines, the shape of Raman spectra is considerably changed due to these frequency shifts. Fig. 3.6 shows polarized Raman spectra of  $\text{KGd}(\text{WO}_4)_2$  and  $\text{KYb}(\text{WO}_4)_2$  in geometry  $\mathbf{z}(\mathbf{yy})\mathbf{z}$  and  $\mathbf{z}(\mathbf{yx})\mathbf{z}$  in the region of  $600 - 1100 \text{ cm}^{-1}$ . The  $3A_g$  and  $2B_g$  vibrations are of interest in this spectral region, which are marked by numbers 1 - 5 in Fig. 3.6 and in Table 3.3. Lines 2, 4, and 5 shift slightly (about  $0 - 8 \text{ cm}^{-1}$ ) with changing the type of Ln cation, while the frequency shifts of lines 1 and 3 reach  $16 \text{ cm}^{-1}$ . As a result,  $A_g$  vibrations 1 and 2 in  $\text{KYb}(\text{WO}_4)_2$

merge together into one wide band, while frequency difference of these two vibrations in  $\text{KGd}(\text{WO}_4)_2$  is  $20 \text{ cm}^{-1}$ . An effective SRS generation has been obtained on  $A_g$  vibration 2 in the crystal  $\text{KGd}(\text{WO}_4)_2$  [1]. Due to the peculiar transformation of the Raman spectrum of  $\text{KYb}(\text{WO}_4)_2$  in this frequency region, the conditions of SRS generation in this crystal can differ from those in  $\text{KGd}(\text{WO}_4)_2$ . For  $z(yx)z$  scattering polarization the 4-th line at  $810 \text{ cm}^{-1}$  has higher peak intensity and is expected to be dominant in SRS experiments while in  $\text{KGd}(\text{WO}_4)_2$  crystal the most intense is  $767 \text{ cm}^{-1}$  mode.

As shown above, the Raman spectra of low-temperature modification of  $\text{KGd}(\text{WO}_4)_2$ ,  $\text{KYb}(\text{WO}_4)_2$ , and  $\text{KY}(\text{WO}_4)_2$  tungstates are suited to  $C_{2h}^6$  monoclinic structure. In this structure, [W-O] complexes form an octahedron, which is typical for wolframite structure, where potassium and rare-earth ions are positioned regularly and the lattice structure is ordered. It is known that at heating the double tungstates  $\text{KLn}(\text{WO}_4)_2$  (Ln is Gd, Y, or Yb) a phase transformation occurs, which can be caused by either transition order-disorder or transformation into other phase modification with the ordered structure. This phase transition was studied earlier by DTA method, and the high-temperature modification was identified by X-ray diffraction in the samples quickly quenched down to room temperature. The HTRS method allowed us to study this phase transition *in situ* at the transition temperature for the first time (Figs. 3.7 and 3.8). It was found that the low-temperature monoclinic configuration of  $\text{KGd}(\text{WO}_4)_2$ ,  $\text{KYb}(\text{WO}_4)_2$ , and  $\text{KY}(\text{WO}_4)_2$ , in which W has the octahedron neighboring, transforms into the high-temperature form with tetrahedral [W-O] complex and the ordered distribution of K and Ln ions over the lattice sites. The  $\text{KGd}(\text{WO}_4)_2$  high-temperature structure can be saved at room temperature by quick quenching, while the  $\text{KYb}(\text{WO}_4)_2$  high-temperature modification cannot be realized at  $T=300 \text{ K}$  by this technique. Hence, the HTRS for the first time allowed us to get information about  $\text{KYb}(\text{WO}_4)_2$  high-temperature structure (Fig. 3.8), which in contradiction with the data of previous papers turned out to be similar to that of  $\text{KGd}(\text{WO}_4)_2$  and  $\text{KY}(\text{WO}_4)_2$ .

To determine if the  $\text{KLn}(\text{WO}_4)_2$  structure transforms to disordered scheelite structure during the phase transition, we studied Raman spectrum temperature variations of a series of double tungstates  $\text{NaLn}(\text{WO}_4)_2$  (Ln is La, Gd, Y) and  $\text{KLa}(\text{WO}_4)_2$ . The disordered scheelite structure is frozen in these tungstates down to room temperature. We found that the random distribution of Na, or K, or La ions over cation sites leads to nonuniform broadening and splitting of  $A_{1g}$ -valence symmetrical vibration of  $[\text{WO}_4]$  tetrahedron due to variation of its cation surrounding in the region  $900 - 930 \text{ cm}^{-1}$  (Fig. 3.6). This phenomenon is most pronounced in  $\text{NaLa}(\text{WO}_4)_2$ , where the  $A_{1g}$ -vibration splits into 7 components with  $A_{1g}$ -symmetry (Fig. 3.6).

This peculiarity of  $A_{1g}$ -vibration behavior keeps up to the melting point. The effect of  $A_{1g}$ -vibration non-uniform splitting was not observed at the phase transition of the tungstate series  $KLn(WO_4)_2$ . By contrast, at the phase transition in these crystals, the high-frequency line was recorded to narrow down and to shift considerably to the frequency of  $[WO_4]$  octahedron symmetrical vibration. This proves the change of W coordination from 6 to 4 and the ordered character of the high-temperature structure of double tungstates  $KLn(WO_4)_2$ .

The HTRS method gives an opportunity to trace the formation of  $[W-O]$  groups in the double tungstates  $K(Na)Ln(WO_4)_2$  not only in the crystalline state but also in the melt. For this purpose, we previously measured vibration spectra of melts of simple alkali tungstates  $K_2WO_4$  and  $Na_2WO_4$  and rare-earth tungstates  $Gd_2(WO_4)_3$  and  $La_2(WO_4)_3$ . HTRS spectra of these melts, first recorded in polarized light in VH and HH geometry, were identified to belong to separate  $[WO_4]$  complexes in isotropic medium (Fig. 3.7). It was found that the  $A_1$  valence vibration frequency is minimum in  $K_2WO_4$  and  $Na_2WO_4$  melts and shifts by 20-25  $cm^{-1}$  to high-frequency region in melts of  $Gd_2(WO_4)_3$  and  $La_2(WO_4)_3$ . This is explained by influence of the basic cation valency on the force constants of the anion  $[WO_4]$ . We also have observed that the presence of two cation types has different effect on  $A_1$  vibration frequency of  $[WO_4]$  in the sheelite crystal structure and in the melts of double alkali-rare-earth tungstates. In the crystalline state, this frequency is determined by concentration ratio of cations, which is 1:1. In the melt, this frequency is defined by ratio of valence bonds. Since this ratio is 3:1, the frequency of  $A_1$  valence vibration of  $[WO_4]$  in the melts of the double tungstates is only 2-5  $cm^{-1}$  lower than that for melts of single-component tungstates  $Ln_2(WO_4)_3$  (Figs. 3.7 and 3.8). Using the identified Raman spectra of the separate  $[WO_4]$  complexes in melts, we for the first time studied *in situ* the process of melting-crystallization in double tungstates  $KGd(WO_4)_2$ ,  $KYb(WO_4)_2$ , and  $KY(WO_4)_2$ . It was found that  $KGd(WO_4)_2$  melts congruently at 1110 C, and this melt contains the isolated  $[WO_4]$  tetrahedral complexes. By contrast,  $KYb(WO_4)_2$  melts incongruently at 1115 C, and its melt contains a finely divided solid phase in addition to the melted state with  $[WO_4]$  complexes, that is revealed by shape and complete depolarization of the Raman spectra (Fig. 3.9). From the  $KYb(WO_4)_2$  Raman spectra recorded at higher temperatures, we for the first time measured the liquidus temperature, 1290 C, above which a homogenous melted phase with  $[WO_4]$  complexes is formed.

1. Yu. K. Vishchakas, I. V. Mochalov, A. V. Mikhaylov, R. F. Klevtsova, and A. V. Lyubimov, „Crystal structure and Raman scattering in  $KGd(WO_4)_2$  crystals,“ *Litovskii Phys. Sb.*, 28(2), 224-234 (1988).

Table 3.3.

Frequency ( $\text{cm}^{-1}$ ) and symmetry of Raman lines in  $\text{KGd}(\text{WO}_4)_2$ ,  $\text{KY}(\text{WO}_4)_2$ , and  $\text{KYb}(\text{WO}_4)_2$  single crystals at 300 K. The lines marked in brackets by numbers (1) - (5) correspond to those shown in Fig. 2.

$\text{KGd}(\text{WO}_4)_2$	$\text{KY}(\text{WO}_4)_2$	$\text{KYb}(\text{WO}_4)_2$	Sym.	$\text{KGd}(\text{WO}_4)_2$	$\text{KY}(\text{WO}_4)_2$	$\text{KYb}(\text{WO}_4)_2$	Sym.
78	81	65	$A_g$	297	302	299	$B_g$
86	88	88	$A_g$	314	316	317	$A_g$
100	108	104	$B_g$	342	346	345	$A_g$
113	120	114	$A_g$	349	360	351	$B_g$
113	108	114	$A_g$	372	378	380	$B_g$
121	133	131	$A_g$	401	408	404	$A_g$
130	110	119	$B_g$	410	406	402	$B_g$
141	132	133	$B_g$	437	444	449	$A_g$
149	133	131	$A_g$	528	531	530	$B_g$
165	127	132	$B_g$	530	532	515	$A_g$
173	180	177	$A_g$	684	686	681	$B_g$
191	225	225	$B_g$	686	687	688	$A_g$
206	223	218	$A_g$	748	752	757	$A_g$ (1)
219	204	206	$B_g$	758	770	774	$B_g$ (3)
235	237	237	$A_g$	768	764	760	$A_g$ (2)
251	287	260	$B_g$	809	809	810	$B_g$ (4)
273	281	289	$A_g$	901	905	908	$A_g$ (5)
278	287	260	$B_g$	931	933	935	$B_g$

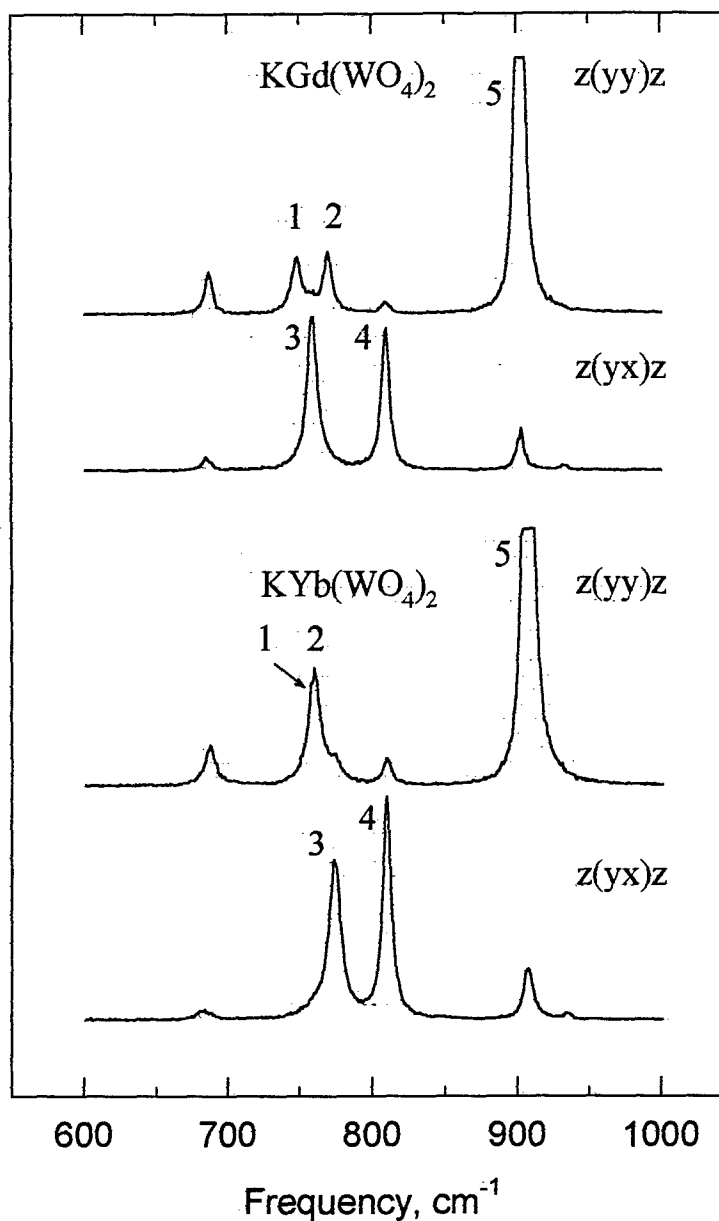


Fig. 3.5. Raman spectra of some tungstate crystals at 300 K temperature.  $\text{KGd}(\text{WO}_4)_2$  - oriented single crystal of  $C_{2h}^6$  symmetry at two scattering geometry  $z(yy)z$  - for  $A_g$  vibronic mode and  $z(yx)z$  - for  $B_g$  vibronic mode.  $\text{NaGd}(\text{WO}_4)_2$  and  $\text{NaLa}(\text{WO}_4)_2$  - polycrystals, synthesized from melt with a structure of disordered sheelite. Arrows mark the splitting of  $A_g$  vibration of  $(\text{WO}_4)$  tetrahedron.

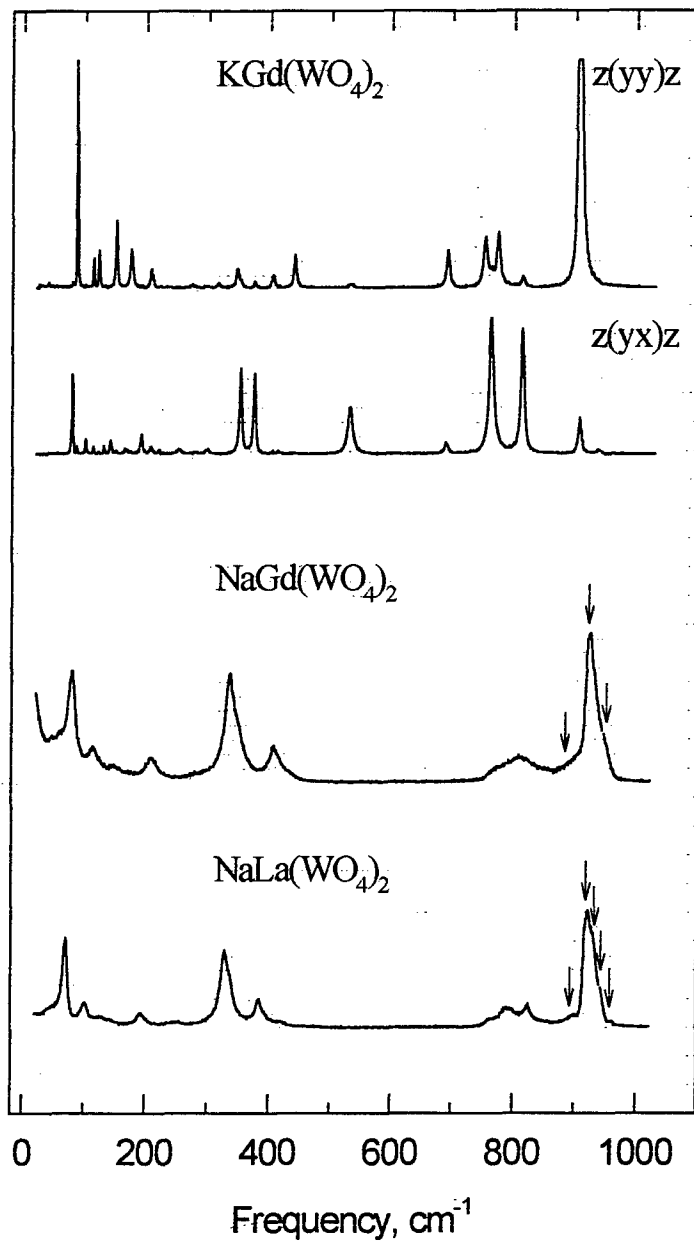


Fig. 3.6. Polarized Raman spectra of oriented single crystals  $\text{KGd}(\text{WO}_4)_2$  and  $\text{KYb}(\text{WO}_4)_2$  in the spectral region from 600 to 1000  $\text{cm}^{-1}$ . With z(yy)z scattering geometry for  $A_g$  vibronic mode and z(yx)z - for  $B_g$  vibronic mode. 1 - 5 arrows denote the vibrons according to the Table.

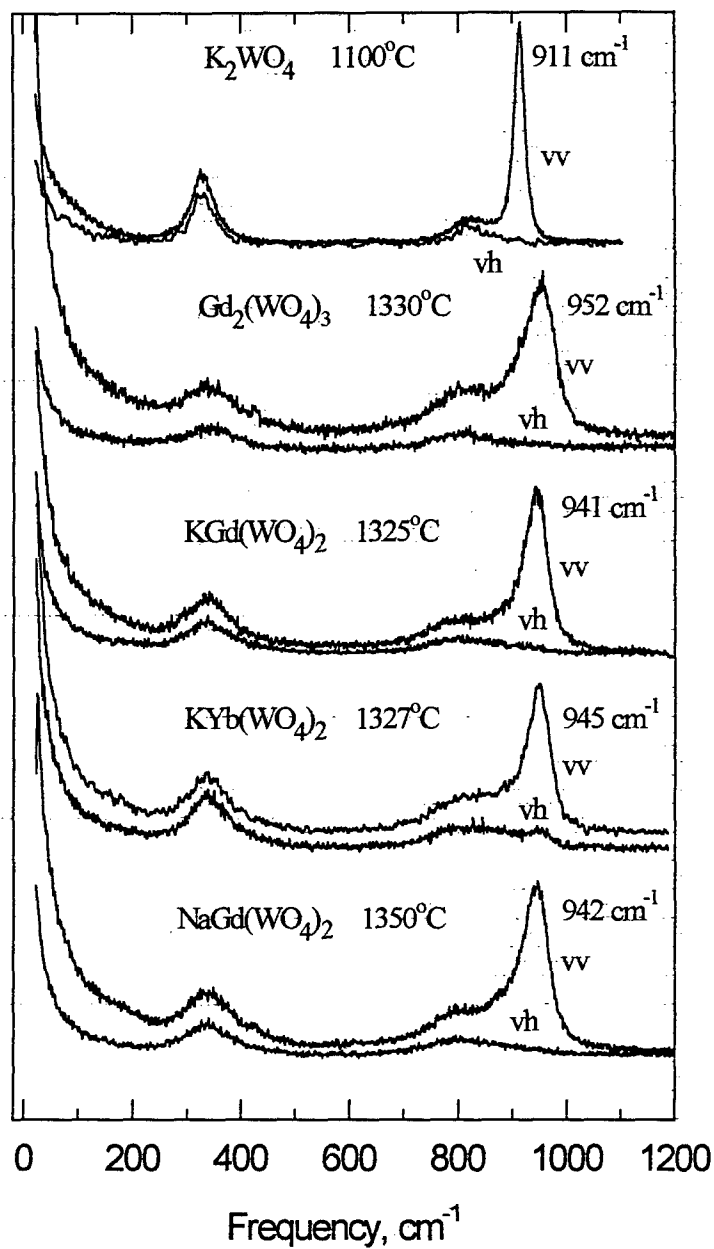


Fig. 3.7. Polarized Raman spectra of some tungstates above the melting point in vv and vh scattering geometries. The frequencies of internal stretching  $A_g$  modes are designated.

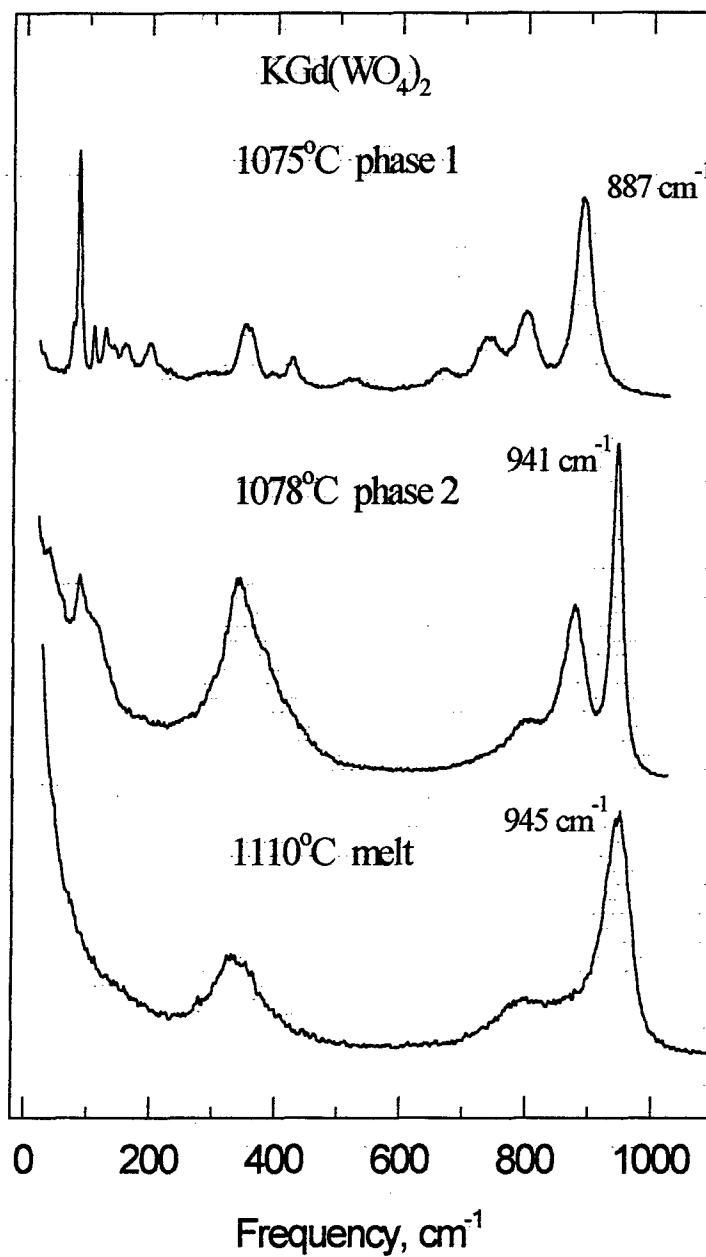


Fig. 3.8 The change of Raman spectra at phase transformations in  $\text{KGd}(\text{WO}_4)_2$  crystal.

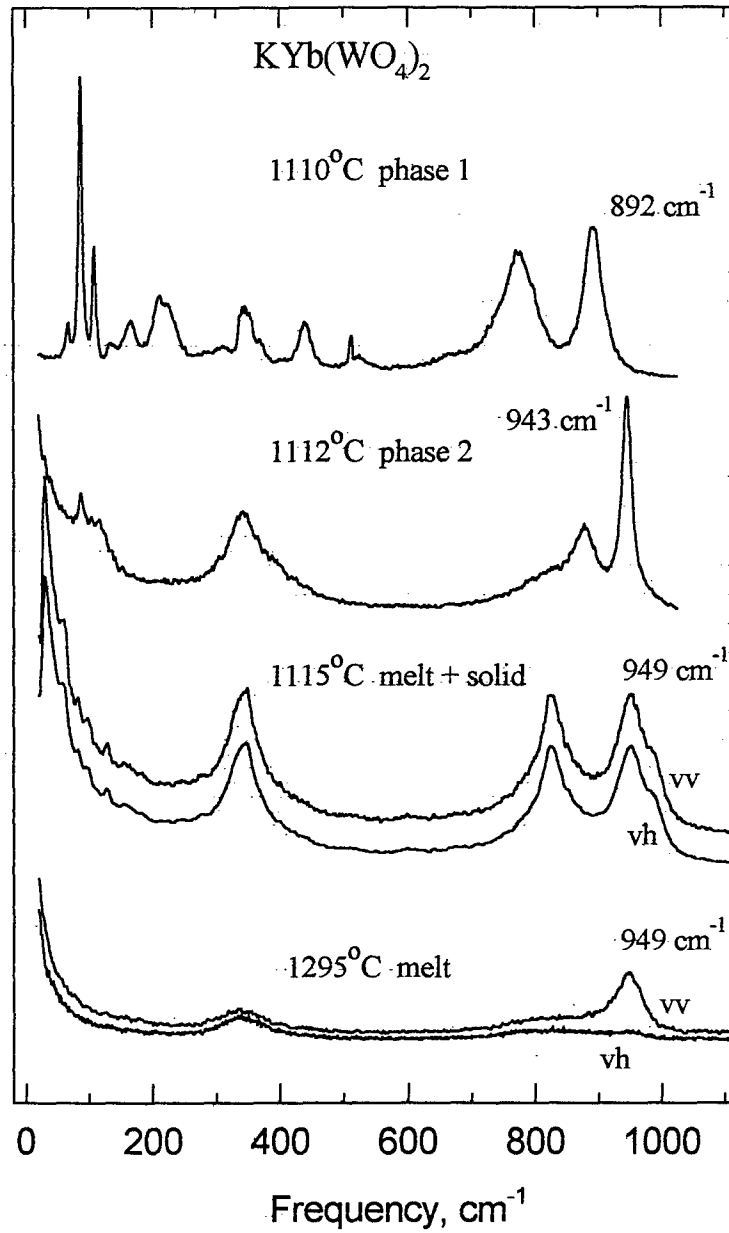


Fig. 3.9 The change of Raman spectra at phase transformations in  $\text{KYb}(\text{WO}_4)_2$  crystal. Polarized Raman spectra *vv* and *vh* are demonstrated for two phase regions at  $1115^\circ\text{C}$  and for homogeneous melt at  $1295^\circ\text{C}$ .

### *Line broadening of SRS-active mode in KGW crystal*

As we mentioned before the Raman gain coefficient which characterizes Raman properties of nonlinear media is inversely proportional to the linewidth of Raman transition. In case of homogeneous broadening the linewidth is a fundamental characteristic of a certain material and is determined by vibronic relaxation mechanisms due to the phonon-phonon coupling in the medium. Thus, precise measurements of Raman mode linewidth and its temperature dependence is very important to characterize Raman properties of the crystal.

The spontaneous Raman scattering spectra of  $\text{KGd}(\text{WO}_4)_2$  crystal at room temperature are shown in Fig. 3.10. The most intense SRS-active vibronic modes corresponds to 901 and 767  $\text{cm}^{-1}$  energies. From Fig. 3.10 one can see also some intense external lattice phonons with 80-250  $\text{cm}^{-1}$  energy.

Below the results on spontaneous Raman spectroscopic study of SRS-active mode in  $\text{KGd}(\text{WO}_4)_2$  crystal with temperature changing are presented. They provided us a new information about a dominant relaxation mechanisms of the high frequency vibronic excitation. The line broadening of 901  $\text{cm}^{-1}$  Raman mode was investigated in the temperature range from 77 to 1300 K. At higher temperature the phase transition and melting of the crystal was observed. Fig. 3.11 presents spontaneous Raman spectra of this mode for three temperatures. One can see that the linewidth is strongly increase with crystal temperature. The temperature dependence of FWHM of 901  $\text{cm}^{-1}$  mode is shown in Fig. 3.12.

It is known that high frequency SRS-active vibrations in molecular ionic crystals belonged to molecular ion (internal vibrations) and isolated from lattice phonons (external vibrations). The number of possible relaxation channels of internal modes is limited and could be interpreted in terms of multiphonon decay mechanism. In case of  $\text{KGd}(\text{WO}_4)_2$  crystal high frequency internal modes correspond to the oscillation of  $(\text{WO}_6)$  molecular group.

Previously there were a number of publications on the vibration relaxation study of internal modes in some molecular ionic crystals, like  $\text{CaCO}_3$  [1, 2],  $\text{K}_2\text{SO}_4$  [3],  $\text{NaNO}_3$  [4],  $\text{Ba}(\text{NO}_3)_2$  [5]. The obtained results for different molecular ionic crystals have shown that the temperature dependence of the homogeneous line broadening provides fundamental information on the dominant mechanism leading to vibrational relaxation [1-4]. The review on detailed theory of relaxation processes in molecular crystals can be found for example in [6]. The main result of this theory is that the full bandwidth  $\gamma_i$  for an internal vibron  $\Omega_i$  in an ideal crystal equals to the sum of several contributions, each arising from a specific depopulation or dephasing mechanism:

$$\gamma_i = \gamma_i^{(3d)} + \gamma_i^{(3u)} + \gamma_i^{(4d)} + \gamma_i^{(4u)} + \gamma_i^{(4u)'} + \gamma_i^{(4dp)} + \gamma_i^{(4dp)'} \quad (5)$$

where the superscript specifies the relaxation mechanism and the number of phonons involved. In particular "d" stands for down conversion process, "u" - for up-conversion, "dp" - for dephasing. In the real crystal there can be also additional relaxation processes connected with impurities and dislocations.

The simplest depopulation process is a *three phonon splitting process*, when one high frequency vibration  $\Omega_i$  is annihilated with emitting two lower energy phonons  $\Omega_j$  and  $\Omega_k$ , so that the energy conservation law  $\Omega_i = \Omega_j + \Omega_k$ . This process contributes to the linewidth as follows:

$$\gamma_i^{(3d)} = 36 \pi \hbar^{-2} \sum_{jk} |B_{ijk}|^2 [(n_j + 1)(n_k + 1) - n_j n_k] \delta(\Omega_i - \Omega_j - \Omega_k) \quad (6)$$

where  $n_i = (\exp \{ \hbar \omega_i / kT \} - 1)^{-1}$  is the corresponding phonon occupation number.

The *three phonon up-conversion process*, which corresponds to the fusion of a  $\Omega_i$  phonon with another one  $\Omega_j$  with producing of a higher energy vibration  $\Omega_k$  so that  $\Omega_k = \Omega_i + \Omega_j$  contributes to the linewidth with the following term:

$$\gamma_i^{(3u)} = 72 \pi \hbar^{-2} \sum_{jk} |B_{ijk}|^2 [(n_j)(n_k + 1) - n_k(n_j + 1)] \delta(\Omega_i + \Omega_j - \Omega_k) \quad (7)$$

The *four phonon splitting process* corresponds to annihilation of a high frequency vibration  $\Omega_i$  with emitting three lower energy phonons  $\Omega_j$ ,  $\Omega_k$ , and  $\Omega_m$ , so that  $\Omega_i = \Omega_j + \Omega_k + \Omega_m$ . This process contributes to linewidth as follows:

$$\gamma_i^{(4d)} = 192 \pi \hbar^{-2} \sum_{jkm} |B_{ijk}|^2 [(n_j + 1)(n_k + 1)(n_m + 1) - n_j n_k n_m] \delta(\Omega_i - \Omega_j - \Omega_k - \Omega_m) \quad (8)$$

There are two possibilities of *four phonon up-conversion process*: the fusion of the  $\Omega_i$  phonon with another  $\Omega_j$  with producing a two phonon state, so that  $\Omega_i + \Omega_j = \Omega_k + \Omega_m$ . This process is described by the following expression:

$$\gamma_i^{(4u)} = 576 \pi \hbar^{-2} \sum_{jkm} |B_{ijk}|^2 [n_j(n_k + 1)(n_m + 1) - (n_j + 1)n_k n_m] \delta(\Omega_i + \Omega_j - \Omega_k - \Omega_m) \quad (9)$$

And the second one is the fusion of the  $\Omega_i$  phonon with two other phonons  $\Omega_j$  and  $\Omega_k$  with producing a higher frequency phonon  $\Omega_m$ , so that  $\Omega_i + \Omega_j + \Omega_k = \Omega_m$ . This process is described by the following expression:

$$\gamma_i^{(4u)'} = 576 \pi \hbar^{-2} \sum_{jkm} |B_{ijk}|^2 [n_j n_k (n_m + 1) - (n_j + 1)(n_k + 1)n_m] \delta(\Omega_i + \Omega_j + \Omega_k - \Omega_m) \quad (10)$$

From the above expressions one can see that the main difference between splitting and up-conversion processes is their contribution to low temperature bandwidth. At low temperature (T=0 K) all phonon occupation numbers are equal to zero and all up-conversion processes

become negligible as they require the thermal bath to be populated. The splitting process is the only nonzero relaxation process at low temperature.

Another four phonon relaxation process is a pure *dephasing process* involving the interaction of excited vibron  $\Omega_i$  with the thermally excited lower energy lattice phonons  $\Omega_j$  and  $\Omega_k$ . In this case these low frequency phonons scatter on high frequency vibration what can be presented as an immediate absorption and emission of phonons with the same energy but with different phases or wave numbers. The corresponding equation will be as follows:

$$\gamma_i^{(4dp)} = 576 \pi \hbar^{-2} \sum_{jk} |B_{ijk}|^2 n_j (n_k + 1) \delta(\Omega_j - \Omega_k) \quad (11)$$

The probability of this process is also negligible at low temperature (T~0 K). In the similar way it is possible to consider a higher phonon processes and to derive the corresponding equations that describe line broadening. These equations will have higher order of multiplication of phonon numbers and correspondingly lower probabilities. Nevertheless as in some cases these processes can be important to describe high temperature data.

All the above relaxation processes were considered in our analysis of temperature line broadening of SRS-active mode in  $\text{KGd}(\text{WO}_4)_2$  crystal. It was also necessary to keep in mind the probable influence of the inhomogeneous broadening due to random cation distribution and crystal disorder.

As it was shown above the only relaxation process that can have a non-zero probability at zero temperature is a splitting process. Using spontaneous Raman spectra we can predict the following three phonon splitting process with the excitation of lower energy internal Raman vibron ( $767 \text{ cm}^{-1}$ ) and a lattice phonon with  $134 \text{ cm}^{-1}$ , that is  $\Omega_{901} \rightarrow \Omega_{767} + \omega_{134}$ . The dashed curve A in Fig. 3.12 corresponds to the temperature dependence described as follows (here we assume that inhomogeneous broadening is negligible):

$$\Delta\Omega_{901}(T) = 3.5 \{ (n_{767} + 1) (n_{134} + 1) - n_{767} n_{134} \} \quad (12)$$

One can see that this curve goes higher than the room temperature point. This can be explained by the fact that inhomogeneous broadening is partially included in the first low temperature point. The exact value of inhomogeneous broadening can be obtained only by detailed investigation of low temperature data by direct measurements of longitudinal and transverse relaxation time of the vibron (see for example [5]). In order to take this into account we fit two lower temperature points with above dependence plus temperature independent inhomogeneous broadening term. The dashed curve B in Fig. 3.12 corresponds to the temperature dependence described as:

$$\Delta\Omega_{901}(T) = 1 + 2.8 \{ (n_{767} + 1) (n_{134} + 1) - n_{767} n_{134} \} \quad (13)$$

Here the first term can be considered as the fixed linewidth due to inhomogeneous broadening. One can see that curve B well describes the line broadening at the temperatures 77 and 300 K. At higher temperature the discrepancy between the curve B and experimental points becomes significant.

Another way to fit all experimental points including high temperature data was to use only a four phonon pure dephasing process:  $\Omega_{901} + \omega_{87} \rightarrow \Omega_{901} + \omega_{87}$  (C curve). It has a stronger temperature dependence and at low temperature its value goes to zero. One can predict that the nonzero linewidth at lowest temperature point can be due to the constant value of inhomogeneous broadening.

The best fit with four phonon dephasing process is shown with dashed curve C and described by the following equation:

$$\Delta\Omega_{901}(T) = 3.5 + 0.28 (n_{87} + 1) n_{87} \quad (14)$$

We can see that this dependence describes well only the highest temperature data but has large discrepancy with intermediate points. The solid line D corresponds to the sum of two relaxation process, which includes three phonon splitting process, and four phonon pure dephasing process together with inhomogeneous part of broadening. The total temperature dependence is now described as

$$\Delta\Omega_{901}(T) = 1 + 2.7 \{ (n_{767} + 1) (n_{134} + 1) - n_{767} n_{134} \} + 0.13 (n_{87} + 1) n_{87} \quad (15)$$

From comparison of this last expression with one describing phonon splitting process (13) we can say that it plays dominant role at  $T \leq 300$  K. It is necessary to note that proposed relaxation mechanism for high temperature is not the only one possible channel. At higher temperature the probabilities of different phonon modes become considerable and many various relaxation mechanisms and their combinations can participate in the damping of  $A_g$  Raman mode. The observed nature of the relaxation of SRS-active vibron in KGW is similar to those in other molecular ionic crystals and due to phonon-phonon coupling inside this group.[1, 2, 5]

The shift of vibron frequencies with temperature has been observed in different media. The theory of frequency shift in crystal can be found in [7, 8]. For phonon frequency one can write

$$\Omega_i(T) = \Omega_i(0) + \Delta\Omega_i^{ah}(T) + \Delta\Omega_i^{se}(T) \quad (17)$$

where  $\Omega_i(0)$  represents the harmonic frequency at 0 K. The temperature dependence arises from two processes. The first one  $\Delta\Omega_i^{ah}(T)$  is due to the thermal expansion of the lattice, that

tends to lowering of the force constants, and the cubic anharmonic coupling contribute to the downshift of the phonon frequency with heating the sample.

The second process described as  $\Delta\Omega_i^{se}(T)$  is determined by the effects of the anharmonic terms in the expansion of the potential in terms of displacement. It appears in the self-energy term which is dependent on the temperature. It was shown that usually this term results in the increase of phonon frequency with increasing the temperature and its value is usually less than that for the first process.

The temperature dependence of SRS-active mode frequency in  $\text{KGd}(\text{WO}_4)_2$  crystal is shown in Fig. 3.13. Phonon energies are slowly decreased with increasing the temperature. From these data we can propose that in  $\text{KGd}(\text{WO}_4)_2$  crystal the frequency shift of internal vibron is mostly due to lattice expansion and can be described in terms of Gruneisen parameter theory [7, 8].

Thus, the temperature measurement of line broadening and shifting in  $\text{KGd}(\text{WO}_4)_2$  crystal and the above analysis have shown that the relaxation mechanisms of SRS-active mode in  $\text{KGd}(\text{WO}_4)_2$  crystal more probable consists of the sum of two channels: three phonon splitting and four phonon dephasing processes. There is also a distinctive impact of inhomogeneous broadening of this mode. These results in the rather high broadening of SRS-active line and limiting SRS gain coefficient in  $\text{KGd}(\text{WO}_4)_2$  at high temperature. Decreasing the temperature of the crystals and improvement of its quality can lead to the SRS gain increasing. There is a small reduction of the mode frequency at temperatures above 300 K. But these data can be important for developing Raman lasers, to know exact value of frequency shift and, correspondingly, precise position of the shifted wavelength.

1. R. Righini, L. Angeloni, E. Castellucci, P. Foggi, S. Califano, and D. A. Dows, *Croat. Chem. Acta*, **61**, 495 (1988).
2. P. J. Delfyett, R. Dorsinville, and R. R. Alfano, "Multiphonon dephasing of the  $1086\text{ cm}^{-1}$  mode in calcite," *Phys. Rev. B*, **39**, 3845-3853 (1989).
3. L. Angeloni, R. Righini, E. Castellucci, P. Foggi, and S. Califano, "Temperature-dependent decay of vibrational excitons in  $\text{K}_2\text{SO}_4$  crystal measured by picosecond time-resolved CARS," *J. Phys. Chem.* **92**, 983-988 (1988).
4. L. Angeloni, R. Righini, "Anomalous temperature dependence of the vibrational exciton lifetime in  $\text{NaNO}_3$  crystal," *Chem. Phys. Lett.* **154**, 115-120 (1989).
5. P. G. Zverev, W. Jia, H. Liu, T. T. Basiev, "Vibrational dynamic of the Raman-active mode in barium nitrate crystal", *Optics Lett.*, **20**, 2378 (1995).
6. S. Califano and V. Schettino, "Vibrational relaxation in molecular crystals," *Int. Rev. Phys. Chem.* **7**, 19 (1988).
7. S. S. Mitra, in "Optical properties of solids," ed. S. Madelmann and S. S. Mitra, New York: Plenum, p.333 (1969).
8. J. Kalus, "Temperature dependence of phonon-frequencies and linewidths for weakly anharmonic molecular crystals," *J. Chimie Physique*, **82**, 137-152 (1985).

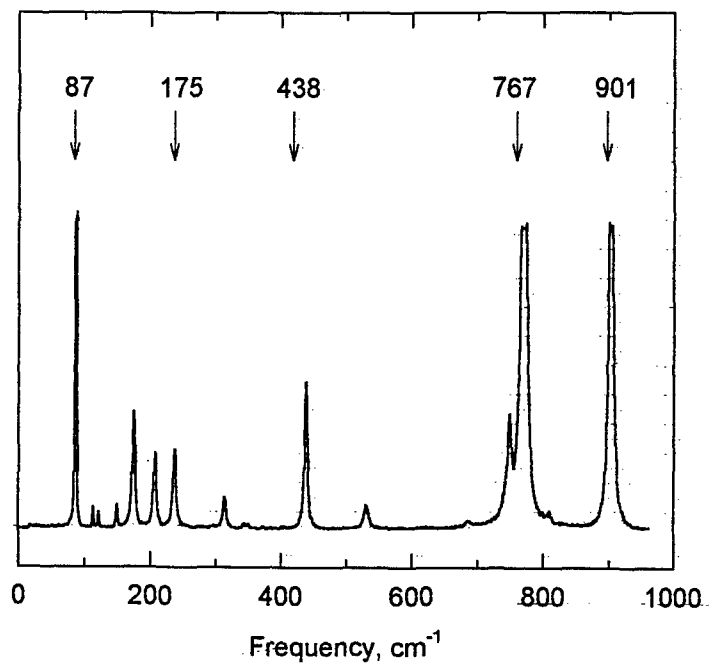


Fig. 3.10. Spontaneous Raman spectra of KGd(WO<sub>4</sub>)<sub>2</sub> crystal.

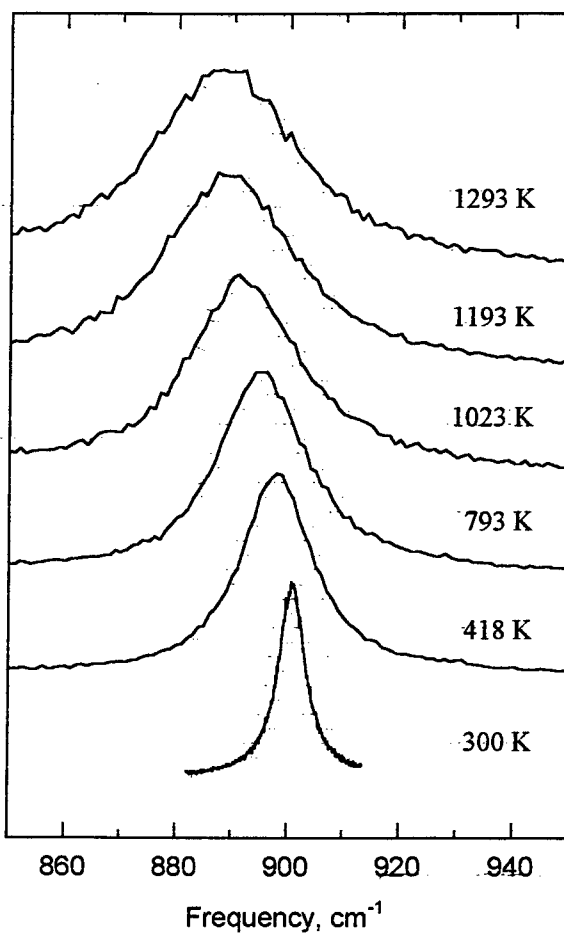
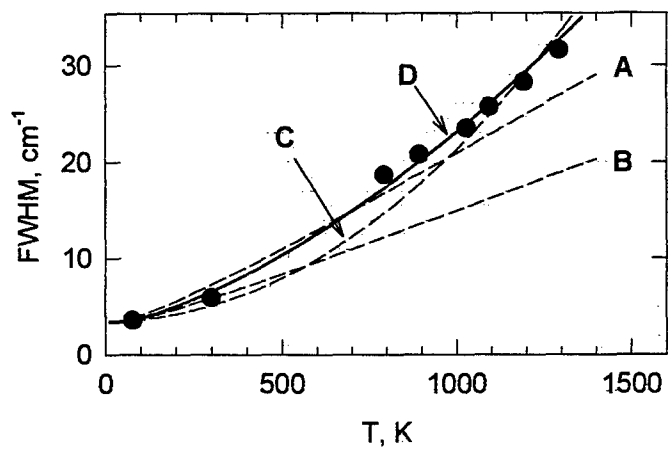


Fig. 3.11. Spontaneous Raman spectra of  $A_g$  mode ( $901 \text{ cm}^{-1}$ ) in  $\text{KGd}(\text{WO}_4)_2$  crystal vs crystal temperature. Line broadening and frequency shift is observed.



A -  $G = 3.5 \cdot \{(n_{761} + 1)(n_{140} + 1) - n_{761} \cdot n_{140}\}$

B -  $G = 1 + 2.3 \cdot \{(n_{761} + 1)(n_{140} + 1) - n_{761} \cdot n_{140}\}$

C -  $G = 3.5 + 0.28 \cdot (n_{88} + 1) \cdot n_{88}$

D -  $G = 1 + 2.7 \cdot \{(n_{761} + 1)(n_{140} + 1) - n_{761} \cdot n_{140}\} + 0.13 \cdot (n_{88} + 1) \cdot n_{88}$

Fig. 3.12. Raman linewidth of  $A_g$  mode ( $901 \text{ cm}^{-1}$ ) in  $\text{KGd}(\text{WO}_4)_2$  crystal vs crystal temperature. Curves A - D results of fit with different relaxation mechanisms.

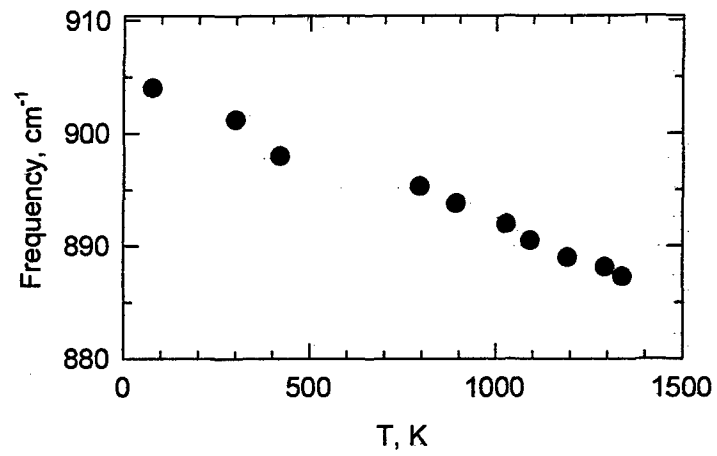


Fig. 3.13. Frequency shift of SRS-active  $A_g$  mode in  $\text{KGd}(\text{WO}_4)_2$  crystal.

### 3.3. Spontaneous Raman spectroscopy of molybdate crystals

Molybdates as perspective Raman materials were investigated in our experiments. Analogous to tungstate we will divide into two types: "simple" molybdates with scheelite structure and "double" molybdates. First we will consider "simple" molybdates. Unpolarized spontaneous Raman scattering spectra of  $\text{CaMoO}_4$ ,  $\text{SrMoO}_4$  and  $\text{BaMoO}_4$  crystals under excitation perpendicular to  $C_4$  axis ( $\mathbf{K} \perp C_4$ ) with the radiation polarized along  $C_4$  ( $\mathbf{E} // C_4$ ) are shown in Fig. 3.14. From Table 3.4 one can see that molybdate crystals exhibit similar behavior as tungstate crystals. In the range of metal ion substitutes  $\text{Ca}^{2+} \rightarrow \text{Sr}^{2+} \rightarrow \text{Ba}^{2+}$ , Raman frequency is slightly increased and its linewidth is strongly narrowed from  $\text{CaMoO}_4$  ( $5.0 \text{ cm}^{-1}$ ) to  $\text{SrMoO}_4$  ( $3 \text{ cm}^{-1}$ ) and  $\text{BaMoO}_4$  ( $2.1 \text{ cm}^{-1}$ ) together with maximum lattice phonon frequency decreasing. Hence, we can predict 1.7 times increase in Raman gain for  $\text{SrMoO}_4$  crystal and 2.4 times increase for  $\text{BaMoO}_4$  with respect to that in  $\text{CaMoO}_4$ . The predicted perceptiveness and high Raman gain in barium molybdate was proved by the peak cross section value measured as high as 62 %, the same as for the best nitrates  $\text{Ba}(\text{NO}_3)_2$ .

Table 3.4. Frequencies  $\Omega_R$  and linewidths  $\Delta\Omega_R$  of SRS active internal  $A_{1g}$  vibronic mode and maximal external lattice mode frequencies  $\omega_{\text{lat}}^{\text{max}}$  in molybdate crystals with scheelite structure.

Material	Lattice space group	Molecular group	Raman freq. $\Omega_R$ ( $\text{cm}^{-1}$ )	Raman line width $\Delta\Omega_R$ ( $\text{cm}^{-1}$ )	$\omega_{\text{lat}}^{\text{max}}$ , $\text{cm}^{-1}$	Integral cross section $\Sigma_{\text{int}}$ (a.u.)	Peak intensity $\Sigma_{\text{peak}}$ (a.u.)	Scattering geometry of excitation	
								K	E
$\text{CaMoO}_4$	$C_{4h}^6$	$[\text{MoO}_4]$	879.3	5.0	266	64	34	$\perp C_4$	$// C_4$
$\text{SrMoO}_4$	"-"	"-"	887.7	2.8	232	55	51	$\perp C_4$	$// C_4$
$\text{BaMoO}_4$	"-"	"-"	892.4	2.1	186	49	62	$\perp C_4$	$// C_4$

We also investigated "double" or mixed molybdate crystals. Two types of cations in the mixed molybdates are statistically occupied the cationic sites of the lattice, and can cause the different variations of environments of  $[\text{MoO}_4]$  molecular groups. In this connection the Raman spectra of such mixed molybdates differs essentially from that one for simple molybdates such as  $\text{SrMoO}_4$ . Fig. 3.15 demonstrates the spectra of simple molybdates and mixed  $\text{NaLa}(\text{MoO}_4)_2$ ,  $\text{KLa}(\text{MoO}_4)_2$ . These spectra were registered using oriented single crystals with scattering

geometry which displays three  $A_{1g}$  - totally symmetric oscillations. The highest frequency line in the region of  $900\text{ cm}^{-1}$  is assigned to  $A_{1g}$  stretching valence vibrations of  $[\text{MoO}_4]$  tetrahedron ( $\nu_1$ ) in the sheelite lattice structure. The similarity of the spectra of mixed and simple molibdates was observed. The existence of two types of cations in mixed molibdates resulted in essential inhomogeneous broadening and splitting of  $A_{1g}$  line of  $\nu_1$   $[\text{MoO}_4]$  vibration. This effect is caused by different environments of  $[\text{MoO}_4]$  tetrahedron in the lattice. This phenomenon is much stronger for  $\text{KLa}(\text{MoO}_4)_2$  single crystal in comparison with  $\text{NaLa}(\text{MoO}_4)_2$ . Strong decrease of the peak intensity of  $\nu_1$  vibration for  $\text{KLa}(\text{MoO}_4)_2$  single crystal take place. Six Raman lines with  $A_{1g}$  symmetry were registered in the region of  $900\text{ cm}^{-1}$  for  $\text{KLa}(\text{MoO}_4)_2$ . Only one  $A_{1g}$  line was registered for simple molibdate in this region. It should be noted that the existence of inhomogeneous environment of  $[\text{MoO}_4]$  group did not influence strongly the integral Raman scattering cross section of  $\nu_1$  oscillation. If we compare the mixed and simple molibdates (see Table 3.5) the sum value of squares under all six  $A_{1g}$   $\nu_1$  vibrations in  $\text{KLa}(\text{MoO}_4)_2$  was (66%) nearly the same as that for  $\text{SrMoO}_4$  (55%).

The second type of mixed molibdates  $\text{KY}(\text{MoO}_4)_2$  demonstrates Raman spectrum which differs from that one for sheelite molibdates (Fig. 3.16). This spectrum was similar to monoclinic tungstates such as  $\text{KY}(\text{WO}_4)_2$ ,  $\text{KGd}(\text{WO}_4)_2$ . Opposite to mixed molybdates  $\text{KLa}(\text{MoO}_4)_2$  and  $\text{NaLa}(\text{MoO}_4)_2$  Raman spectrum of  $\text{KY}(\text{MoO}_4)_2$  consists of narrow lines. Two types of cations in this molibdate are inserted in different but definite cationic positions in monoclinic host lattice which is constructed from  $[\text{MoO}_6]$  octahedrons. There is a difference in Raman spectrum of  $\text{KY}(\text{MoO}_4)_2$  from  $\text{KY}(\text{WO}_4)_2$ . High frequency Raman line in  $\text{KY}(\text{MoO}_4)_2$  shifted  $50\text{-}100\text{ cm}^{-1}$  to higher frequency region in comparison with the same line for  $\text{KY}(\text{WO}_4)_2$ . Moreover there is essential narrowing of the highest frequency line in  $\text{KY}(\text{MoO}_4)_2$  up to  $1.6\text{ cm}^{-1}$  in comparison with the width of  $7\text{ cm}^{-1}$  for the same line in  $\text{KY}(\text{WO}_4)_2$ . Relative measurements for peak and integral Raman scattering cross sections for  $\text{KY}(\text{MoO}_4)_2$  and  $\text{KY}(\text{WO}_4)_2$  is still complicated due to poor quality of the studied crystal.

Table 3.5. Spontaneous Raman characteristics of molybdate crystals.

<i>Sample</i>	$\Omega$ <i>cm</i> <sup>-1</sup>	$\Delta\Omega$ <i>cm</i> <sup>-1</sup>	$\Sigma_{integ}$	$\Sigma_{peak}$
KLa(MoO <sub>4</sub> ) <sub>2</sub>	898	15*	63	
	324	14		
NaLa(MoO <sub>4</sub> ) <sub>2</sub>	891	22		
	318	12.7		
SrMoO <sub>4</sub>	887.2	2.8	55	51
	327	10.8		
KY(MoO <sub>4</sub> ) <sub>2</sub>	868	9		
	948	1.6		
KY(WO <sub>4</sub> ) <sub>2</sub>	774	7.8	64	24
	907	6.1		
CaWO <sub>4</sub>	910.7	4.8	47	18.6

\* - line with inhomogeneous broadening.

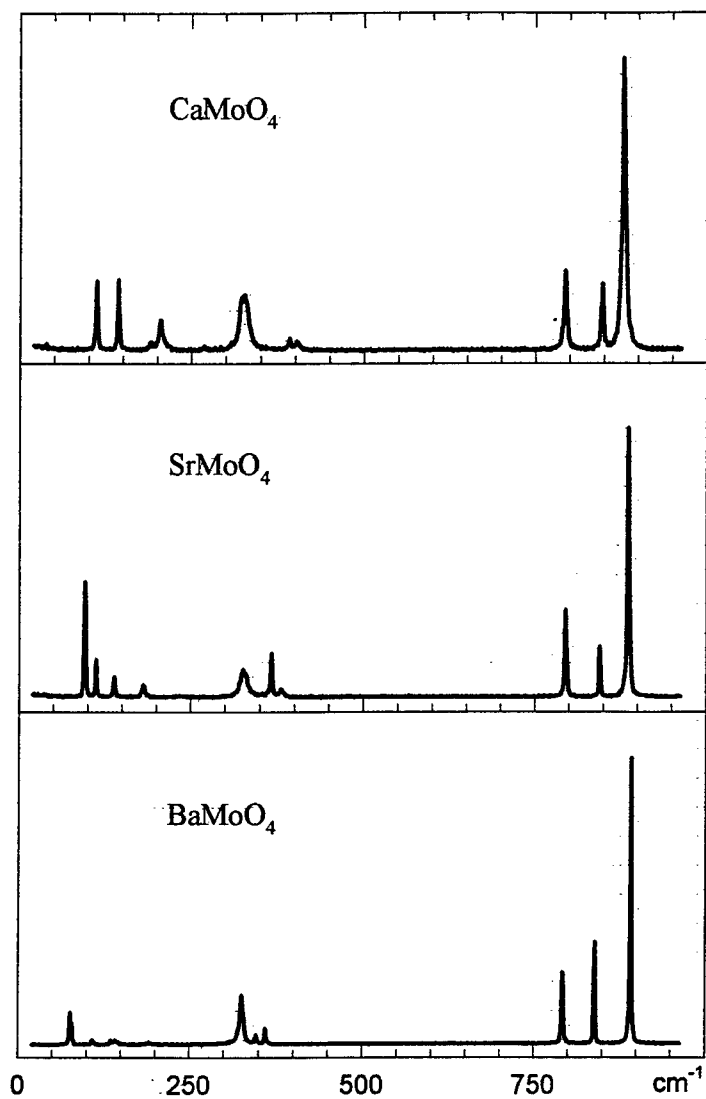


Fig. 3.14. Unpolarized spontaneous Raman spectra of  $\text{CaMoO}_4$ ,  $\text{SrMoO}_4$  and  $\text{BaMoO}_4$  single crystals. Scattering geometry of excitation was  $\mathbf{K} \perp C_4$ ,  $\mathbf{E} // C_4$ .

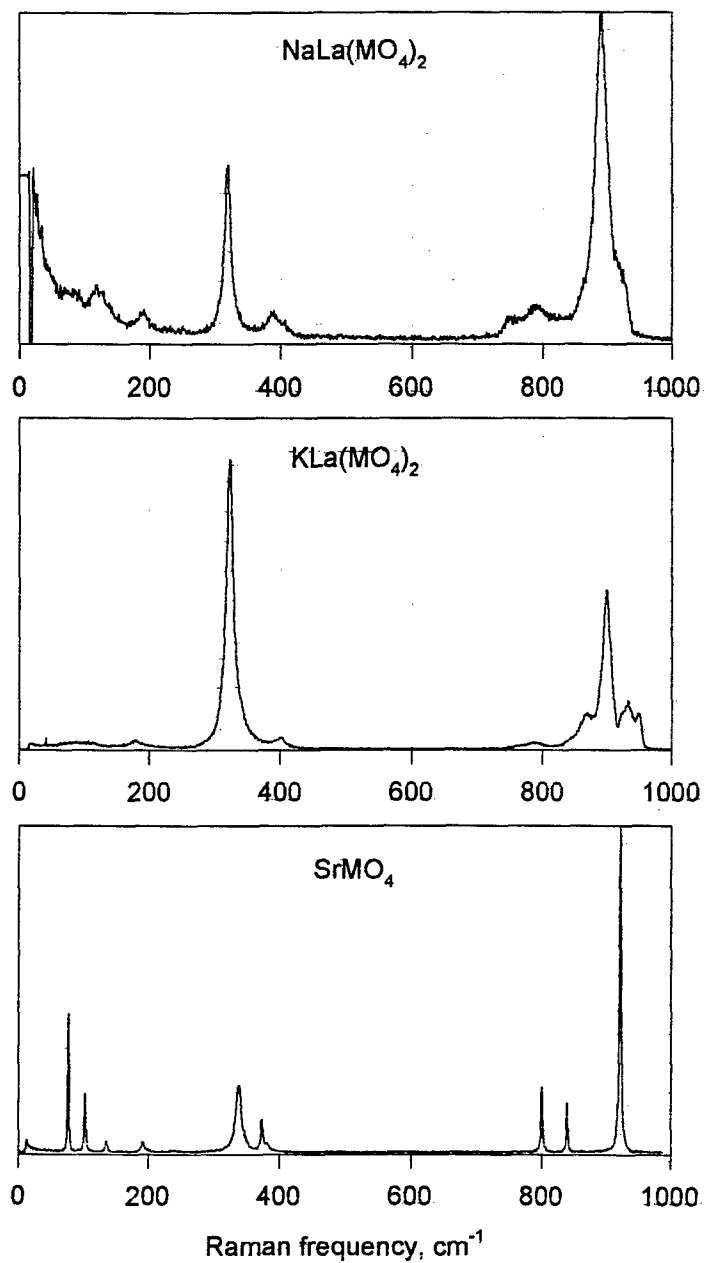


Fig. 3.15. Spontaneous Raman spectra of "double" molybdates

$\text{NaLa}(\text{MoO}_4)_2$  and  $\text{KLa}(\text{MoO}_4)_2$  and simple  $\text{SrMoO}_4$ .

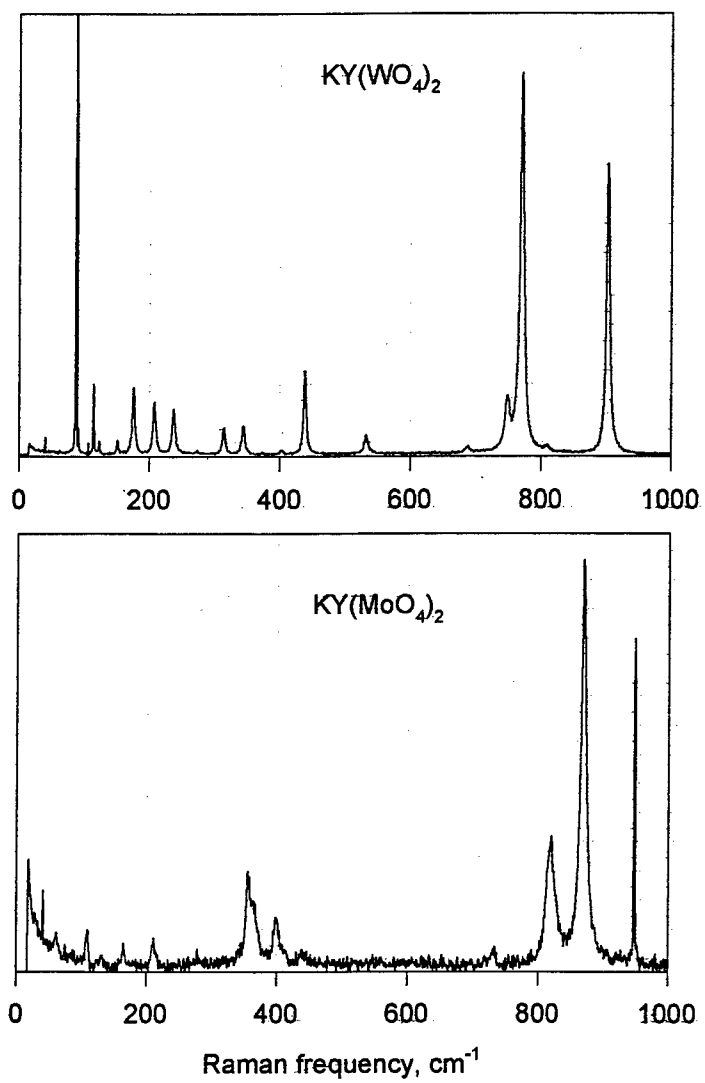


Fig. 3.16. Spontaneous Raman spectra of  $KY(MoO_4)_2$  and  $KY(WO_4)_2$ .

### 3.4. Simple oxide crystals

A major difference between oxides and previously discussed fluorides is much higher average hyperpolarizabilities of oxygen (see Table 3.6). One of the most important features among oxides that their hyperpolarizabilities varies by about an order of magnitude from  $\text{Al}_2\text{O}_3$  to  $\text{SrO}$  with anion-cation separation increasing (Table 3.6). For the oxides with low lying empty 3d shell cations like  $\text{Ti}^{4+}$ ;  $\text{Sc}^{3+}$  or low lying filled *d* shells cations like  $\text{Zn}^{2+}$ ,  $\text{Ga}^{3+}$  hyperpolarizabilities even much higher for the same anion-cation separations.

It allows to expect much stronger Raman scattering cross section for Ga, Sc, Y and Er oxides in comparison with  $\text{Al}_2\text{O}_3$  which was proved in our previous research on  $\text{Y}_2\text{O}_3$  crystals Raman scattering. Even stronger increasing we can expect for  $\text{ZnO}$  and  $\text{TiO}_2$  crystals.

Table 3.6. Nonlinear refractive index  $n_2$  and anion-cation separation in some simple oxide crystals [1].

Sample	Anion-Cation Separation (Å)	Hyperpolarizability, $\gamma(\text{M}_x\text{F})$ ( $10^{-39}$ esu)
$\text{Al}_{2/3}\text{O}$	1.91	248
$\text{Ga}_{2/3}\text{O}$	2.00	887
$\text{Sc}_{2/3}\text{O}$	2.11	920
$\text{Y}_{2/3}\text{O}$	2.27	945
$\text{Er}_{2/3}\text{O}$	2.26	1040
$\text{Si}_{1/2}\text{O}$	1.61	510
$\text{Ti}_{1/2}\text{O}$	1.96	2520
$\text{BeO}$	1.65	436
$\text{SrO}$	2.58	2290
$\text{ZnO}$	1.98	4850

Below we outline spontaneous Raman spectroscopic study for these two crystals in comparison with some other simple oxides and garnets.

$\text{ZnO}$  crystal has a wurzite structure of  $\text{C}_{6v}^4$ . Raman spectrum of this crystal consists of only two strong lines (see Fig. 3.17). Comparative data are presented in Table 3.7. As one can see  $\text{ZnO}$  has thermoconductivity a little less than for  $\text{Al}_2\text{O}_3$  and  $\text{Y}_2\text{O}_3$  but higher than for all other oxides:  $\text{SiO}_2$ , garnets and  $\text{TiO}_2$ . Raman line broadening not big, and not small, similar to  $\text{CaWO}_4$  and

KGW. Integral and peak cross section is higher than for  $Y_2O_3$  and garnets but much less than for  $TiO_2$ .

$TiO_2$  crystal has rutile structure of  $D_{4h}^{14}$  space group. This crystal provides a wide transparency spectral range of 0.43 - 6.2  $\mu m$  and quite high thermoconductivity  $k = 12.6$  W/m-K, which is 10 times higher than that for nitrates and a few times higher than for tungstates and niobates. Rutile is insoluble in water and has the Knupp hardness of 879 kg/mm<sup>2</sup>.

Factor group analysis predicts four Raman active vibrations with symmetry  $A_{1g} + B_{1g} + B_{2g} + E_g$ . Polarized Raman spectra shown in Fig. 3.18. reliably identify  $\nu(E_g) = 449$   $cm^{-1}$  and  $\nu(A_{1g}) = 612$   $cm^{-1}$  Raman lines. The intensity of  $A_{1g}$  vibration mode depends strongly on the geometry of the scattering. It has the highest value when vector  $\mathbf{K}$  of excitation laser beam is perpendicular to tetragonal c-axis of the crystal and polarization vector  $\mathbf{E}$  is parallel to it. The 90° rotation of  $\mathbf{E}$  vector caused the strong (by a factor of 8-10) decreasing intensity of  $A_{1g}$  line. The Raman spectrum of  $TiO_2$  consists of broad lines with the width of 30-40  $cm^{-1}$ . Integral and peak cross section of the strongest  $A_{1g}$  Raman mode are presented in the Table 3.7. Integral cross section one of the highest 159% and has practically the same value as the strongest line of 632 for  $LiNbO_3$  (166%) and 60% higher than the reference data of diamond. Due to strong line broadening the peak cross section (10%) is much than that in diamond (100%), tungstates, iodate and niobates but still much higher than for all other simple oxides with high thermoconductivity.

Fig. 3.19 presents spontaneous Raman spectra of  $TiO_2$  and  $LiIO_3$  crystals measured at room and liquid nitrogen temperatures. One can see that lowering the temperature results in approximately twice reduction of the Raman mode linewidth from  $\Delta\Omega(300K)=34.4$   $cm^{-1}$  to  $\Delta\Omega(77K)=16.4$   $cm^{-1}$ . As a result the peak intensity is twice increased and one should expect the peak cross section from 10% up to 20% at liquid nitrogen temperature which is close to values obtained in calcite and tungstate materials. Similar behavior is observed in  $LiIO_3$  crystal the linewidth of 826  $cm^{-1}$  mode is narrowed from  $\Delta\Omega(300K)=25$   $cm^{-1}$  to  $\Delta\Omega(77K)=16$   $cm^{-1}$  and the peak cross section is increased 1.4 times from 25% to 35% of that in diamond.

#### References:

1. R. Adair, L. L. Chase, S. Payne, Nonlinear refractive index of optical crystals, Phys. Rev. B, **39**, 3337 (1989).

Table 3.7. Spontaneous Raman characteristics and thermo-conductivity of oxide crystals at room temperature.

<i>Sample</i>	$\Omega$ <i>cm<sup>-1</sup></i>	$\Delta\Omega$ <i>cm<sup>-1</sup></i>	$\Sigma_{integ}$	$\Sigma_{peak}$	Thermo conduct., W/K m
Al <sub>2</sub> O <sub>3</sub>	418.6	2.0	0.05	0.07	35
SiO <sub>2</sub>	464.5	7.0	2.2	1.2	14
Y <sub>2</sub> O <sub>3</sub>	378.6	4.0	3.3	2.16	27
Y <sub>3</sub> Al <sub>5</sub> O <sub>12</sub>	783	8	3.0	1.0	13
Lu <sub>3</sub> Al <sub>5</sub> O <sub>12</sub>	796	11	2.8	0.7	13
ZnO	438	6.0	7.14	2.7	21
TiO <sub>2</sub>	612	49 (24)*	159	10 (20)*	8 - 12
LiNbO <sub>3</sub>	632	27	166	18	4.6
LiIO <sub>3</sub>	826	5 (3.3)*	54	25(35)*	

\* the values in brackets were measured at 77 K temperature

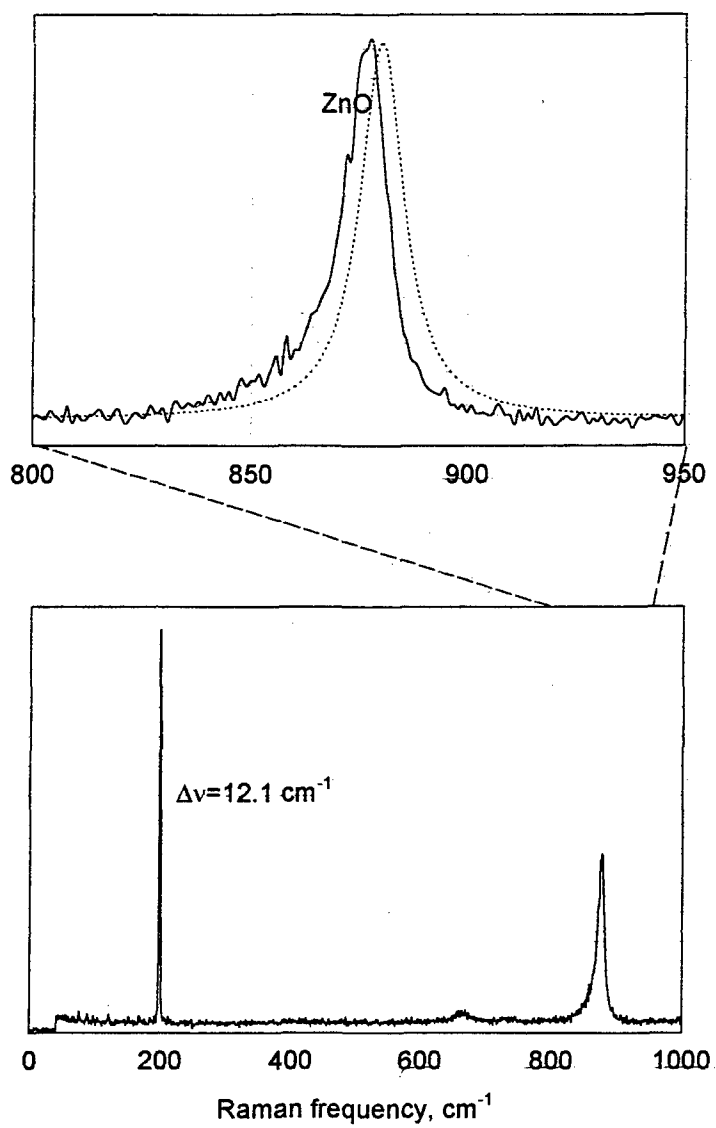


Fig. 3.17. Spontaneous Raman spectrum of ZnO crystal and curve fit of the most intensive line.

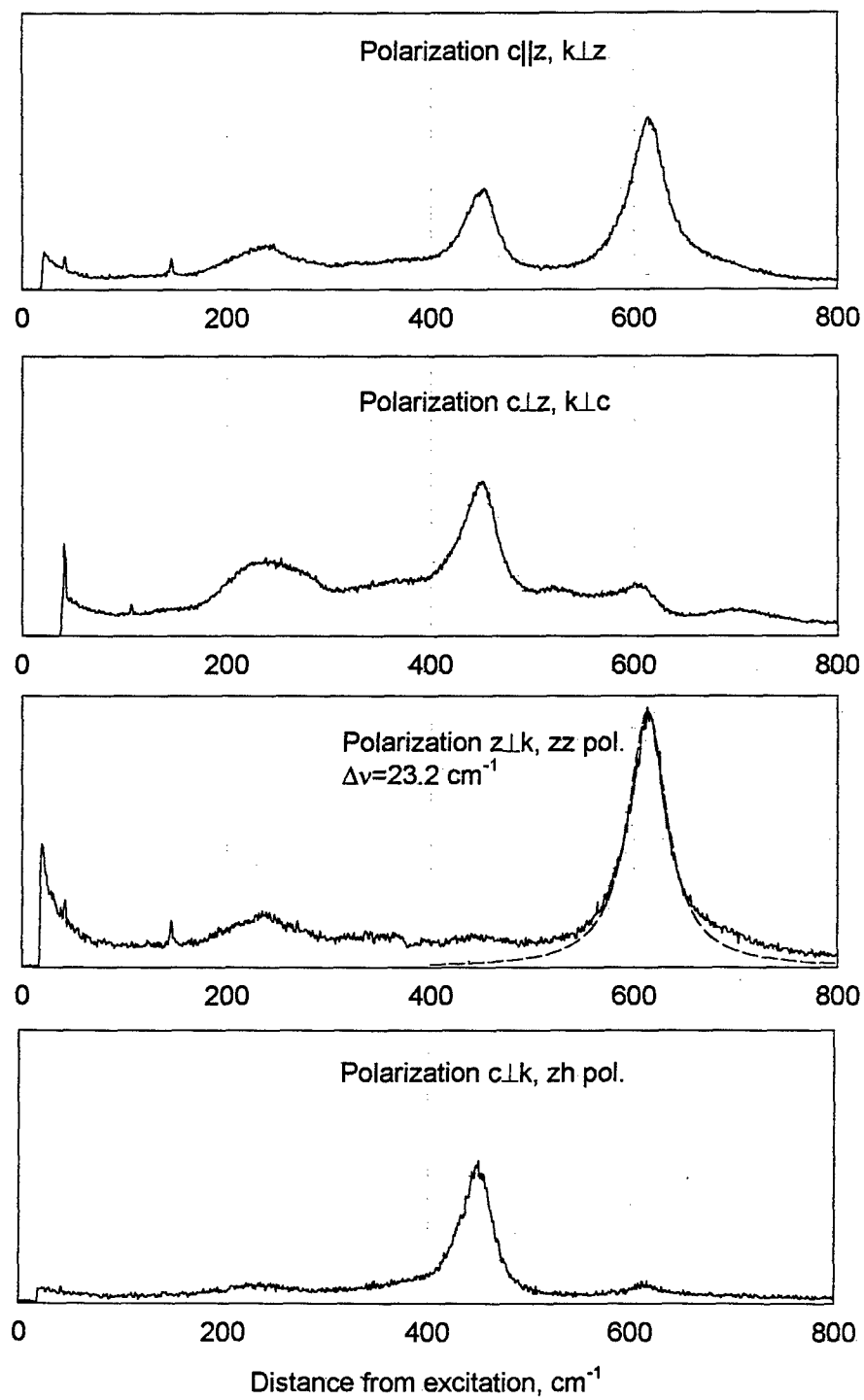


Fig. 3.18. Spontaneous Raman spectra of  $\text{TiO}_2$  crystal with different orientation and polarization and results of curve fit.

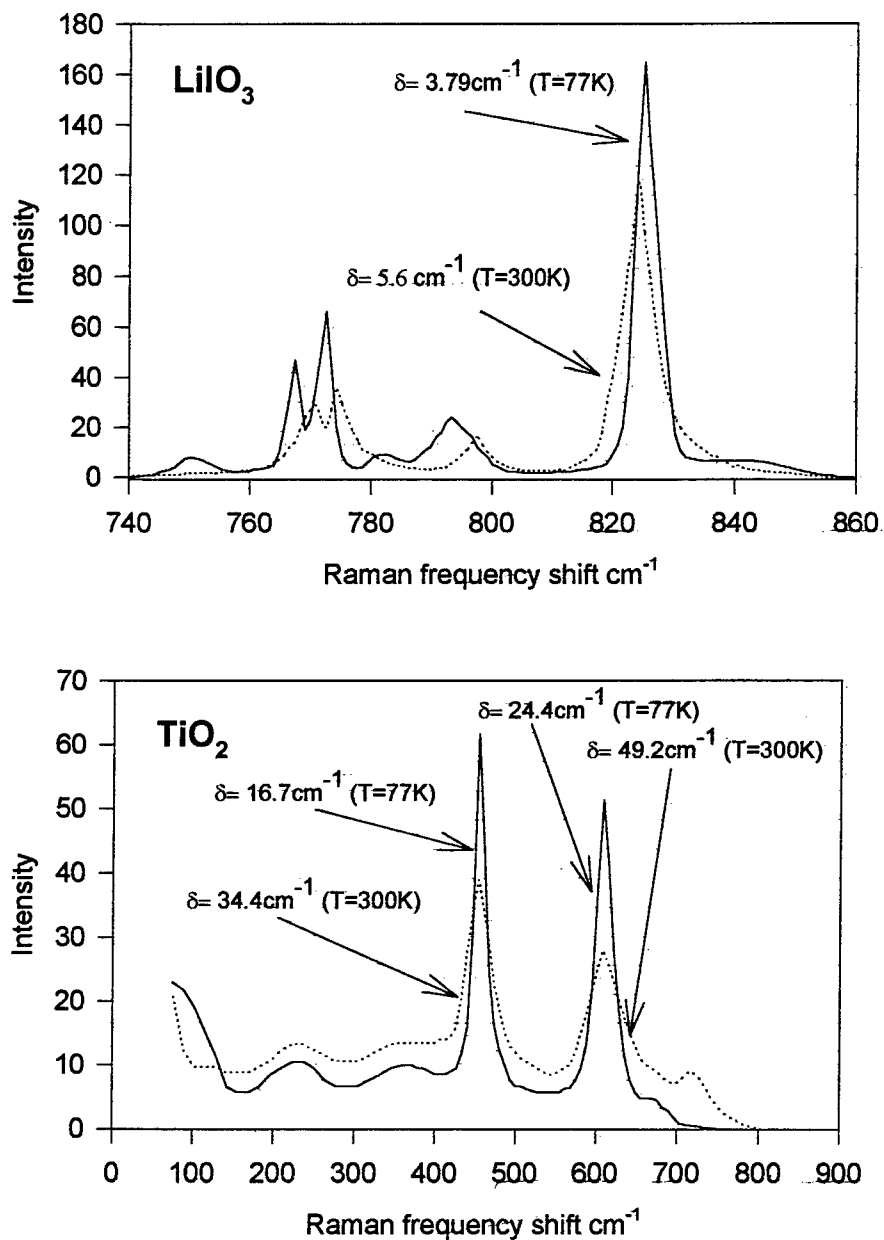


Fig. 3.19. Spontaneous Raman spectra of  $\text{LiIO}_3$  and  $\text{TiO}_2$  crystal at room and liquid nitrogen temperature.

### 3.5. Semiconductor crystals for Raman lasers

From the literature data and our preliminary study we have found that GaP semiconductor crystal with nondirect band-to-band transition and wide transparency spectral range (0.53 - 16  $\mu\text{m}$ ) is one of the most promising Raman materials. It possesses a high thermoconductivity of 140 W/m·K and a strong Raman active vibronic LO mode with frequency  $\Omega_R = 404 \text{ cm}^{-1}$  and a very narrow Raman line (spectral width  $\Delta\nu_R = 1.5 \text{ cm}^{-1}$ ). Our results have shown that the integral Raman scattering cross section in GaP is 70% higher than that in diamond and peak cross section is 160% higher. But as one can find in Ref. [1], optical quality of GaP strongly depends on impurity absorption in transparency region. While trying to reach the highest Raman gain, one must estimate maximum pump density in order not to damage the single crystal).

Another semiconductor crystal with wide transparency range 0.9-15  $\mu\text{m}$  promising for infrared Raman laser application is GaAs, which is widely used in optoelectronic and laser technology. Its thermoconductivity is also quite high of 81 W/m·K, and its spontaneous Raman scattering spectrum demonstrates high intensity Raman line with the frequency  $\Delta\nu_R = 296 \text{ cm}^{-1}$  and the small broadening  $\Delta\nu_R = 2.0 \text{ cm}^{-1}$ , only a little wider than that in GaP crystal.

The main feature which can limit GaAs application is a strong, allowed direct band-to-band transition close to the spectral range of interest 1.3 - 1.4  $\mu\text{m}$ , which can result in rather high linear and nonlinear absorption losses.

Below we will present and compare results on investigation of optical properties of three GaP crystal samples and three GaAs crystal samples. The samples were prepared from crystals produced in different growth processes and as we will see below they exhibit different parameters.

Figs. 3.20, 3.21 show transparency spectra of GaP and GaAs correspondingly measured by an SF-8 spectrophotometer. Its working spectral region spread from 350 nm till 1.8  $\mu\text{m}$ . One can see that the transparency region of GaP and GaAs samples spread from 0.6 and 1  $\mu\text{m}$  to IR, respectively. At the same time the transmission in the near IR spectral region is far from 100% due to Fresnel reflection and absorption losses. Below we will consider the reasons which results in the reduction of sample transmission in the near IR.

#### *Optical losses of semiconductor plane-parallel plate in near IR spectral region*

The long wavelength edge of band-to-band optical transition in GaP and GaAs semiconductor materials are located at about 600 and 900 nm respectively. This results in higher values of refractive index in comparison with other solid state dielectric materials. They are equal to 3.2 for GaP and 3.4 for GaAs crystals. This is the reason why semiconductor samples have higher value of Fresnel losses.

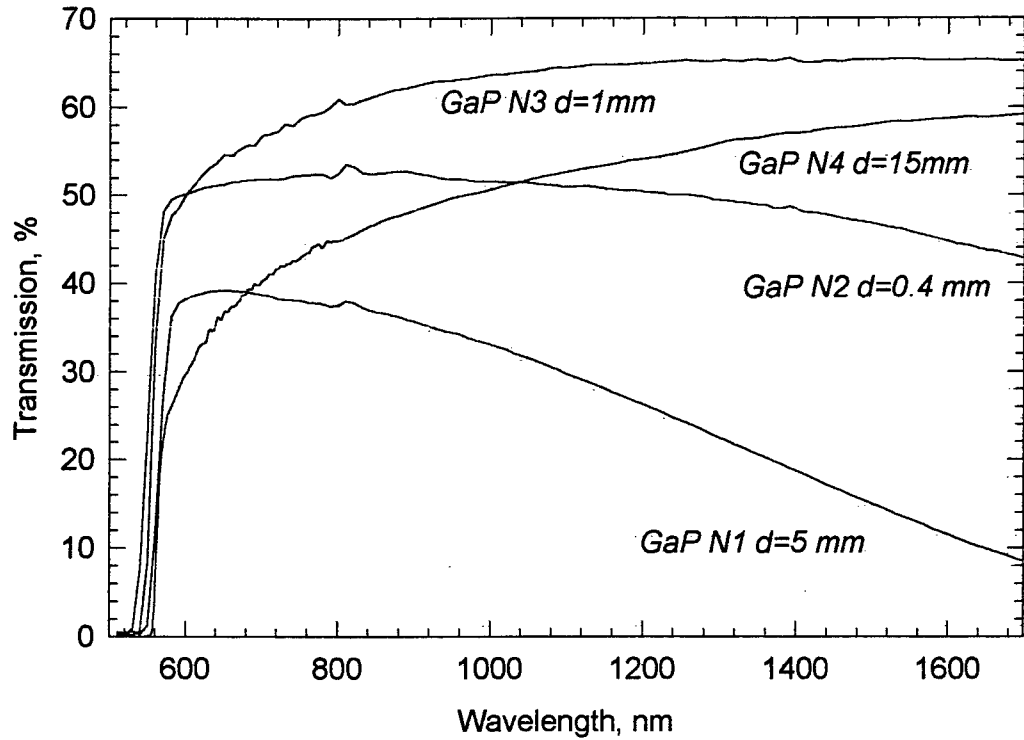


Fig 3.20. Transmission spectra of GaP crystal at T=300K

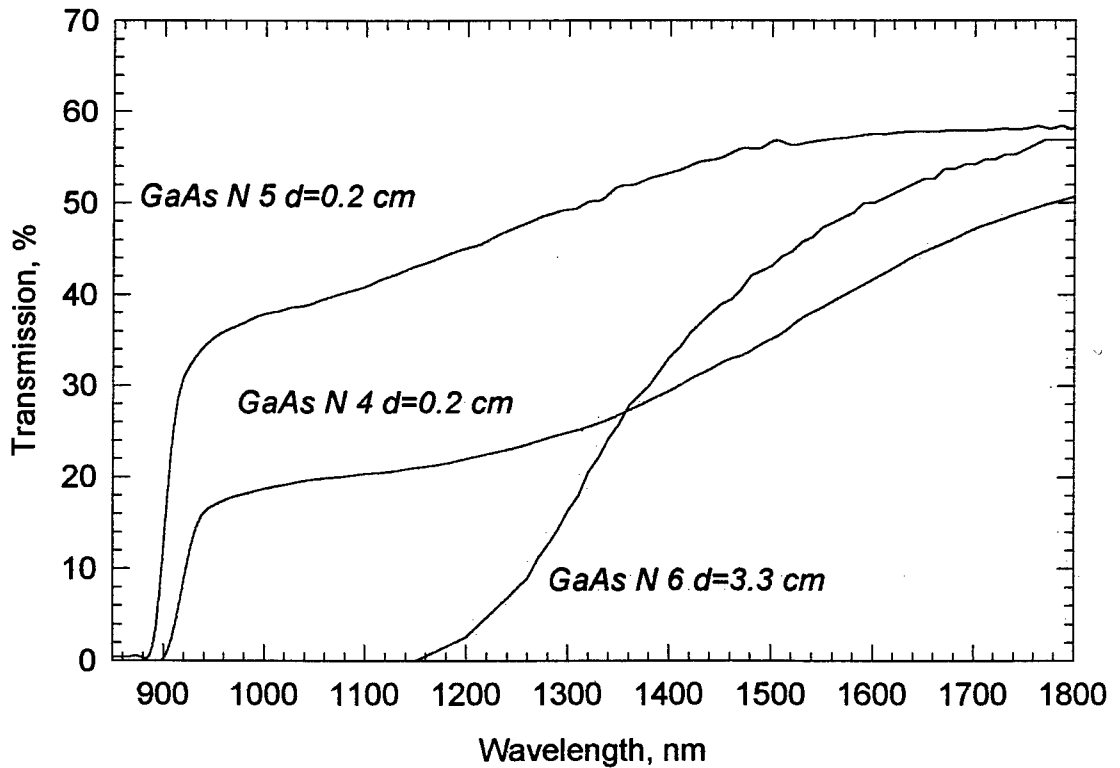


Fig 3.21. Transmission spectra of GaAS crystal at T=300K

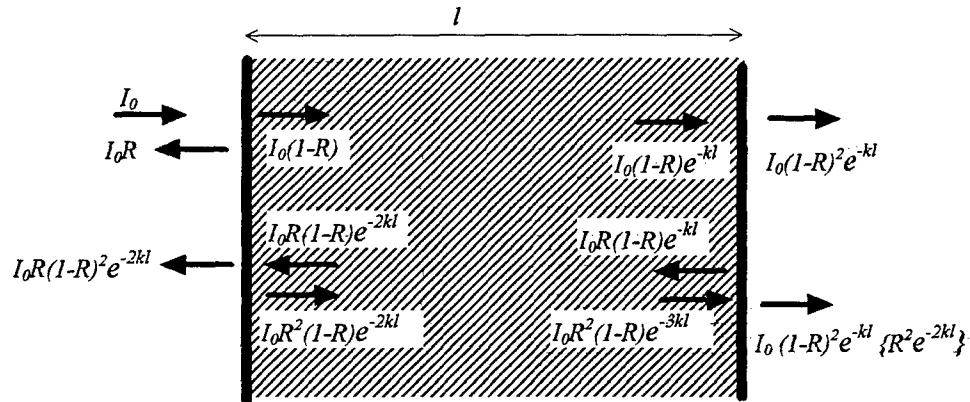
In order to take into account reflection losses correctly and calculate absorption and scattering losses in the bulk materials lets consider in details the transmission of plane parallel semiconductor plate. The reflection coefficient ( $R$ ) for perpendicular incidence light is determined by Frenel formula as:

$$R = \frac{|\sqrt{\varepsilon} - 1|^2}{|\sqrt{\varepsilon} + 1|^2} = \frac{(n-1)^2 + (k\lambda/4\pi)^2}{(n+1)^2 + (k\lambda/4\pi)^2} \quad (1)$$

Here  $\varepsilon$  is a dielectric susceptibility,  $k$  is absorption coefficient,  $n$  - refractive index of the medium, and  $\lambda$  - laser wavelength. For the typical values of absorption coefficient ( $k \approx 1 \text{ cm}^{-1}$ ) in the visible and near IR spectral regions ( $\lambda \sim 10^4 \text{ cm}$ ), the second sum terms in numerator and denominator in (1) can be neglected. In this case the reflection coefficient equals to

$$R = \left( \frac{n-1}{n+1} \right)^2 \quad (2)$$

Lets consider the transmission of the light through the plane parallel plate with reflection coefficient at the surfaces  $R$  and bulk medium transmission  $T = \exp(-kl)$  (here  $k$  is absorption coefficient and  $l$  is the thickness of the sample).



At high absorption in the medium or small reflection it is sufficient to consider only one pass through the sample. In this case the transmission of the sample equals to

$$T_{\Sigma} = (1-R)^2 e^{-(kl)} \quad (3)$$

and the reflection equals  $R_{\Sigma} = R$ . For the medium with low losses it is necessary to take into account the multiple transmission of the light through the sample. In case of noncoherent light and adding, the transmitted beam is described by the geometric progression as follows:

$$T_{\Sigma} = (1-R)^2 e^{-kl} + (1-R)^2 e^{-kl} \{R^2 e^{-2kl}\} + (1-R)^2 e^{-kl} \{R^2 e^{-2kl}\}^2 + \dots = (1-R)^2 e^{-kl} \sum_{n=0}^{\infty} \{R^2 e^{-2kl}\}^n$$

$$T_{\Sigma} = \frac{(1-R)^2 e^{-kl}}{1 - e^{-2kl} R^2} \quad (4)$$

Similar consideration of the reflected light gives the following expression:

$$R_{\Sigma} = R \left( 1 + \frac{(1-R)^2 e^{-2kl}}{1 - R^2 e^{-2kl}} \right) \quad (5)$$

In the medium with no absorption equations (4) and (5) become:

$$T_{\Sigma} = \left( \frac{1-R}{1+R} \right) \quad (6)$$

$$R_{\Sigma} = \frac{2R}{1+R} \quad (7)$$

One can easily see that in this case  $T_{\Sigma} + R_{\Sigma} = 1$ .

The obtained equations describe the case when the resultant light intensity equals to the sum of incoherent beam intensities, while in case of monochromatic radiation their interference must be taken into account and the sum of their electromagnetic field must be considered. In this case the transmission of the plate depends not only on the reflection and absorption coefficients of the substance, but also on the relation between the plate thickness and the radiation wavelength. In this case the transmission of the plate is determined by the equations of Fabri-Perrot etalon:

$$T_{FP}^{\min} = \frac{(1-R)^2 e^{-kl}}{(1 - e^{-kl} R)^2} \quad T_{FP}^{\max} = \frac{(1-R)^2 e^{kl}}{(1 + e^{-kl} R)^2} \quad (8)$$

In case of no absorption, the maximal transmission  $T^{\max} = 1$ , and minimal  $T^{\min} = (1-R)^2 / (1+R)^2$ .

*Table 3.8. Calculated reflection and transmission of GaP, GaAs and Si materials (in case of no absorption).*

Substance	$n$	$R = (n-1)^2 / (n+1)^2$	$R_{\Sigma}$	$T_1 = (1-R)^2$	$T_{\Sigma}$	$T_{FP}^{\min}$
GaP	3.2	0.27	0.43	0.53	0.57	0.32
GaAs	3.4	0.30	0.46	0.49	0.54	0.29
Si	3.5	0.31	0.47	0.48	0.53	0.28

The absorption spectra of investigated crystal samples are shown in Fig. 3.20, 3.21. The values of reflection and transmission of the samples measured with free running Nd<sup>3+</sup>:YAG laser working at 1.064 and 1.32  $\mu\text{m}$  wavelengths are presented in Table 3.9.

Table 3.9. Experimental data on reflection, transmission and absorption of investigated semiconductor samples.  $E$  - energy of incident laser beam.

Sample	thickness $d, \text{mm}$	$\lambda,$ $\mu\text{m}$	$R_{exp}$	$T_{exp}$	$A=1-(T+R)$	$E,$ $\text{mJ}$
GaP N1	5	1.064	0.29	0.30	0.41	8
		1.32	0.26	0.20	0.54	56.6
GaP N2	0.4	1.064	0.36	0.52	0.12	8
		1.32	0.38	0.48	0.14	56.6
GaP N3	1	1.064	0.37	0.60	0.03	8
		1.32	0.40	0.60	0.00	4.2
GaP N3B	15	1.064		0.52		
		1.032	0.4	0.57	0.03	37
GaAs N4	2	1.064	0.33	0.20	0.47	8
		1.32	0.32	0.25	0.43	61.6
GaAs N5	2	1.064	0.43	0.37	0.20	8
		1.32	0.39	0.42	0.19	61.6
GaAs N6	30	1.064	0.29	0.005	0.74	20
		1.32	0.31	0.18	0.52	35
GaAs N7a	1.5	1.064	0.37	0.32	0.31	8
		1.32	0.30	0.32	0.40	61.6
GaAs N7b	0.7	1.064	0.29	0.43	0.28	8
		1.32	0.28	0.42	0.30	61.6

Table 3.10. The absorption coefficient in investigated samples calculated from laser experiments

Sample	$\lambda=1.064 \mu\text{m}$	$\lambda=1.32 \mu\text{m}$
GaP N1	$1.1 \text{ cm}^{-1}$	$1.9 \text{ cm}^{-1}$
GaP N2	$2 \text{ cm}^{-1}$	$3.5 \text{ cm}^{-1}$
GaP N3	$<0.2 \text{ cm}^{-1}$	$<0.1 \text{ cm}^{-1}$
GaP N3B	$0.07 \text{ cm}^{-1}$	$0.03 \text{ cm}^{-1}$
GaAs N4	$4.5 \text{ cm}^{-1}$	$3.2 \text{ cm}^{-1}$
GaAs N5	$1.5 \text{ cm}^{-1}$	$0.6 \text{ cm}^{-1}$
GaAs N6	$1.5 \text{ cm}^{-1}$	$0.3 \text{ cm}^{-1}$

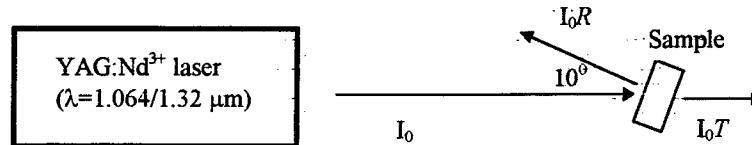
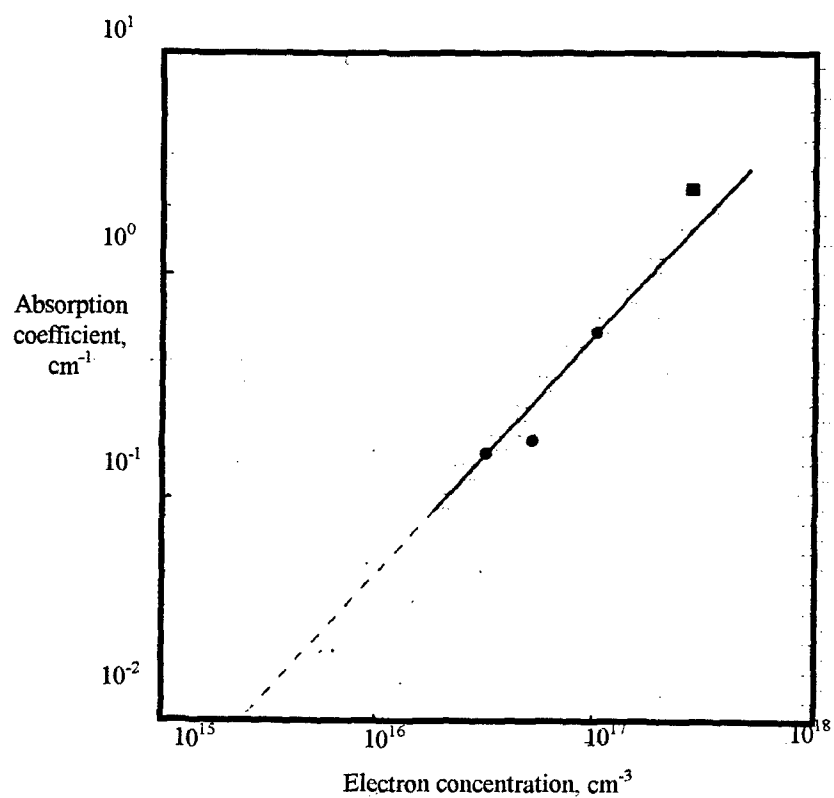


Fig. 3.22. Experimental setup for measuring reflection and transmission of investigated plane parallel plate samples using a free-running  $\text{Nd}^{3+}$ :YAG laser.

One can see that one of the best GaAs crystal (N6) has absorption coefficient of  $k(1.06)=1.5 \text{ cm}^{-1}$  and lower than that corresponds to the data presented in Ref. [1] for pure GaAs with carrier concentration  $N=10 \text{ cm}^{-3}$ . For  $1.3 \mu\text{m}$  wavelength of laser pumping the absorption losses could be even much less  $< 0.3 \text{ cm}^{-1}$ , which is the same order of magnitude as in GaP Raman laser material.

Our calculation of impurity concentration in GaP crystal from absorption coefficient data  $k(1.06)$  ( $0.07 \text{ cm}^{-1}$  for the best crystal GaP N3B) and dependence  $k=f(N)$  Fig. 3.23 from Ref. [2] allows to make the estimation  $N_1(\text{GaP}, N1) = 2 \cdot 10^{17} \text{ cm}^{-3}$ ,  $N_2(\text{GaP}, N2) = 3.5 \cdot 10^{17} \text{ cm}^{-3}$ ,  $N_{3B}(\text{GaP}, N3) = 2 \cdot 10^{16} \text{ cm}^{-3}$ . One can see that the concentration of parasitic impurities for GaP, N3B sample doesn't exceed  $10^{17} \text{ cm}^{-3}$ . Following [1] this is a required criteria for application of the certain sample for Raman laser development based on GaP crystal.



*Fig.3.23. Absorption coefficient as a function electron concentration in GaP.*

#### References

1. J.Nishizawa, K. Suto «Semiconductor Raman Laser», J.Appl.Phys.51(5), pp2429-2431, 1994)
2. K. Suto and J. Nishizawa «Semiconductor Raman Lasers» Artech House Optoelectronics Library, pp. 1-226 (1994).

#### 4. Investigation of Raman parameters of solid state materials by SRS amplification technique

There are a few different ways to investigate Raman properties of solid state materials: spontaneous Raman spectroscopy, coherent anti-Stokes Raman spectroscopy, SRS-amplification technique. Spontaneous Raman spectra measure the scattering of the laser light by spontaneous phonons in the crystal. As the value of this cross section is rather low and the phonon population in the excited state is limited the measured signal in spontaneous Raman scattering experiments is also rather weak and can be registered with high resolution only in visible spectra range. There are different types of laser active spectroscopic techniques developed for the Raman spectroscopy. Coherent anti-Stokes laser spectroscopy provide strong excitation of phonons with the energy which equals to the frequency difference between the two pump beams. The third probe beam exhibits Raman scattering at this intense phonon mode. Angular phase matching conditions are arrange between two pump and the probe beams to observe the scattered radiation. This technique has very high sensitivity but it is based on four wave mixing processes and has the limitation in solids due to strong non-resonant background.

Below we will consider two-photon SRS-amplification technique. It has no spectral range and background limitation and directly measure the main parameters required for developing Raman lasers. In this method, two laser beams are directed into a Raman active medium under investigation: a strong pump beam  $\nu_{pump}$  and a weak frequency tunable probe signal beam  $\nu_{probe}$ . The probe beam is amplified by the Raman effect if the frequency difference  $(\nu_{pump} - \nu_{probe})$  is close to the frequency of Raman vibration mode  $\Omega_R$  excited by pump laser:

$$I_s(\nu, l) = I_s(\nu, 0) \exp\{I_{pump} G(\nu_{pump} - \nu_{probe}) l\} \quad (4.1)$$

where  $I_s(\nu, 0)$  and  $I_s(\nu, l)$  are the intensities of the probe beam at the entry and exit from the medium;  $I_p$  is the intensity of the pump beam in the medium;  $G(\nu_{pump} - \nu_{probe})$  is the spectral Raman gain, proportional to the cross section of spontaneous Raman scattering at a frequency  $(\nu_{pump} - \nu_{probe})$  near the frequency of the Raman-active vibration  $\Omega_R$ ; and  $l$  is the length of the interaction region in a crystal. In the linear approximation, when we can assume that  $\{I_p G(\nu_{pump} - \nu_{probe}) l\} \ll 1$ , expression (4.1) can be written as follows:

$$I_s(\nu, l) = I_s(\nu, 0) [1 + I_p G(\nu_p - \nu) \cdot l] \quad (4.2)$$

It is evident from expression (4.2) that the change in the intensity of the probe beam at the exit from the crystal  $I_s(\nu, l)$  is then proportional to the spontaneous Raman scattering spectrum.

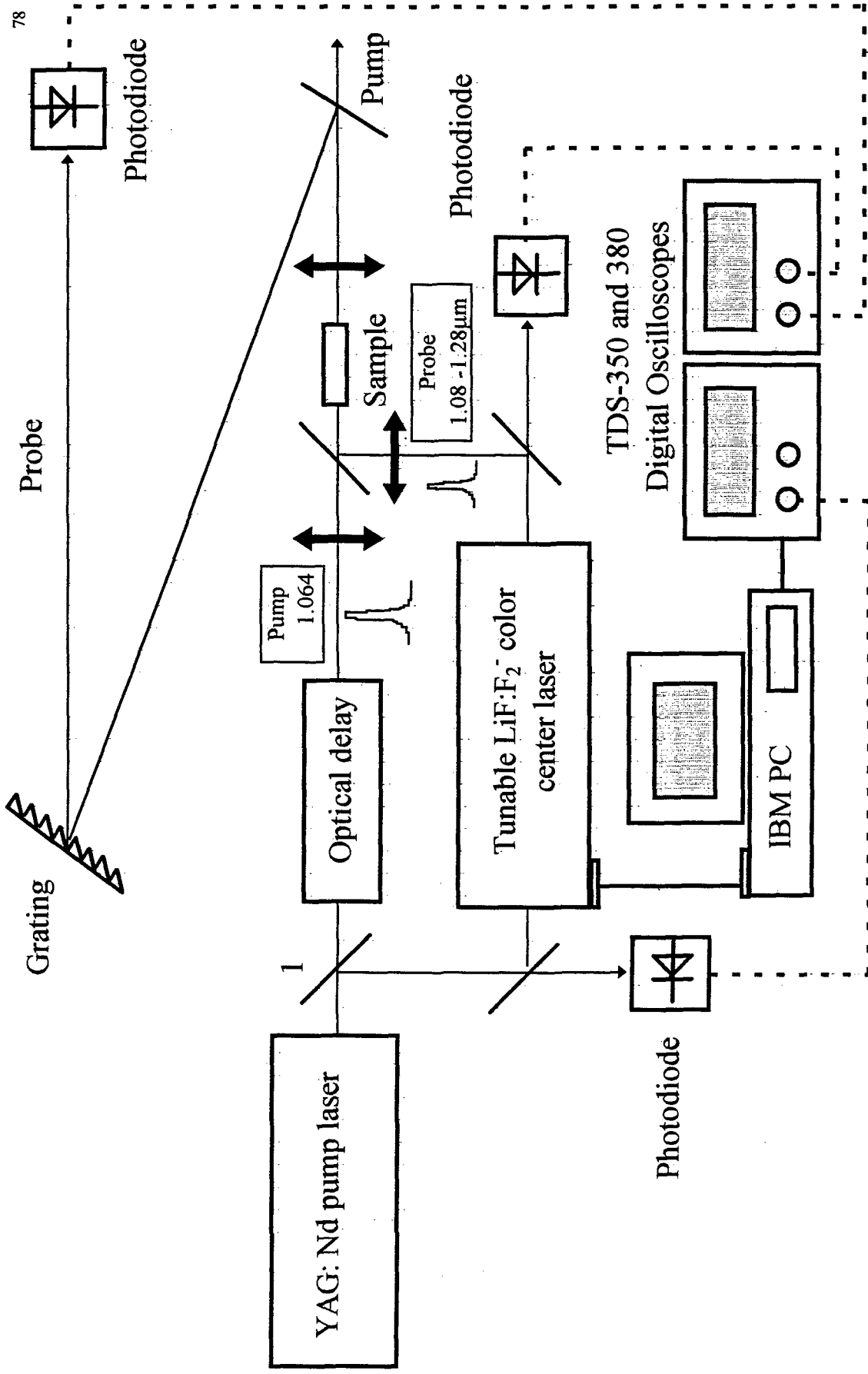


Fig.4.1 Setup for Raman scattering amplification measurements.

The experimental setup for SRS amplification has been developed. The schematic drawing, representing the setup is shown in Fig. 4.1. Specially designed passively Q-switched Nd:YAG laser consisting of the master oscillator and two stage double-pass amplifier with SBS phase conjugating mirror was used as a pump source for the whole scheme. The laser operated in a single transverse and longitudinal mode and delivered about 300 mJ in a 10 ns giant pulse with smooth Gaussian-like profile. The output radiation was split by the tilt mirror (1) into two beams. One beam was used to pump the tunable laser based on LiF crystal with  $F_2^-$  color centers and the second was passed through the optical delay line and used as a pump for the tested sample. The LiF: $F_2^-$  color center laser was used as a tunable source of probe beam for Raman amplification measurements. The laser was computer controlled and allowed to operate within 1.08-1.29  $\mu\text{m}$  wavelength range with the laser line width of 2  $\text{cm}^{-1}$  or 0.1  $\text{cm}^{-1}$  depending on whether the etalon was inserted inside the cavity or not. This allows to investigate SRS amplification coefficient of Raman modes with frequencies from 140 till 1600  $\text{cm}^{-1}$ . A unique feature of the LiF: $F_2^-$  color center laser is its high gain, so it is possible to generate tunable radiation practically simultaneously with the pump laser radiation. Therefore, an optical delay of 15-20 ns in the pump channel is sufficient for complete synchronization of the pump and probe beams. The pump and probe beams were focused inside the sample so that the pump beam diameter was at least twice as large as that for probe beam within the whole sample crystal length. The cross section of the pump beam inside the sample was adjusted for different crystals in accordance with their nonlinearity and damage threshold. The two beams cross sections and their intersection within the sample's volume were specially controlled. A set of neutral filters was applied to adjust the intensity of the pump beam. The probe beam intensity was then set to be more than two orders of magnitude lower than that for the pump beam.

The pump beam was extracted from the scheme by the tilt dichroic mirror (5) with high transmission at the pump wavelength and high reflectivity within the probe beam wavelength band. The resulting signal was sent to the grating, applied to additionally spectrally divide the pump and amplified probe beams, and the diffracted beam was measured by the photodiode. The temporal shape and temporal intersection of pump and probe pulses was controlled by measuring both signals in the grating's zero order diffraction maximum. The pump, reference and amplified pulses were simultaneously monitored by fast Ge pin-photodiodes and TDS-380 and TDS-350 digital oscilloscopes controlled by the computer via GPIB port. The specially designed computer program allowed the ratio of the amplified and reference signals to be calculated and displayed on-line. This setup was used to measure the gain spectra of various Raman materials and to

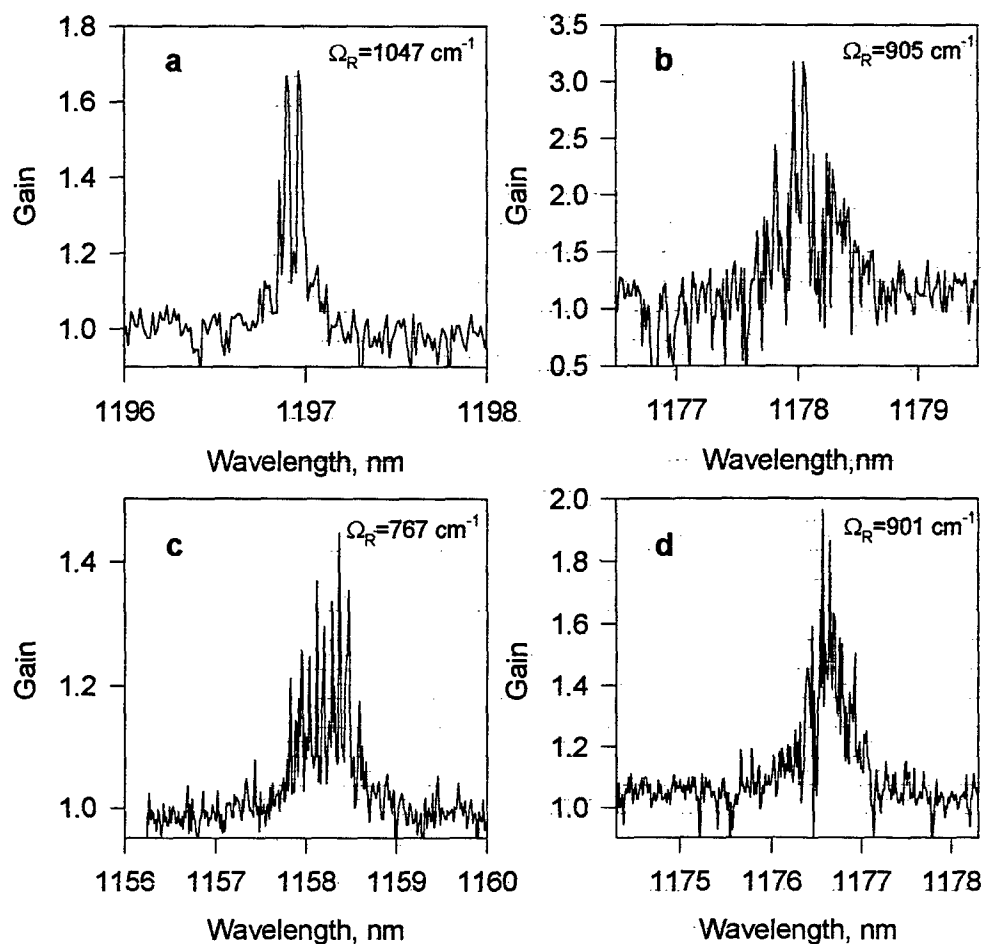


Fig. 4.2 Raman gain spectra of  $\text{Ba}(\text{NO}_3)_2$  (a),  $\text{KY}(\text{WO}_4)_2$  (b) and two different orientations of  $\text{KGd}(\text{WO}_4)_2$  (c,d) scanned with probe laser operating without intracavity etalon.

determine the value of gain coefficient in the maximum of the gain curve. For gain spectra measurements the probe beam wavelength was continuously scanned within the desired wavelength region and the value of pump, reference and amplified signals and also the ratio of the last two signals were recorded for two cases with sample's pump turned on and off. The ratio of the resulting spectra for these two cases then represented the gain spectra of the sample. For the gain coefficient measurements the wavelength of the probe laser was tuned to the center of the gain curve and the above mentioned signals were measured during a single shot. For statistics several measurements were made and only data with the same values of pump and probe signals were selected, diminishing the influence of initial conditions fluctuations.

The experimental setup was used for measuring of Raman amplification in various hosts. The Raman gain spectra of the most interesting lines in  $\text{Ba}(\text{NO}_3)_2$ ,  $\text{KGd}(\text{WO}_4)_2$  and  $\text{KYb}(\text{WO}_4)_2$  crystals are shown in Fig. 4.2. The spectra were scanned with probe  $\text{LiF:F}_2^-$  laser operating

without intracavity etalon, resulting in  $2 \text{ cm}^{-1}$  laser line width. Such regime occurred to be useful to determine the maximum of the gain curve however for crystals with narrow Raman lines the width is measured incorrectly and is determined by the laser line width. The spectral resolution limitation caused by the laser line width can be easily seen when Raman amplification spectra of  $\text{Ba}(\text{NO}_3)_2$  crystal (Fig. 4.2a) is considered. The line width of the measured spectra is in good coincidence with the width of the probe laser line, though the position of Raman line maximum is determined with good accuracy. Then the etalon can be inserted inside the cavity and the scan for narrow lines proceeded again. The maximum continuous scan range of the  $\text{LiF:F}_2^-$  laser with intracavity etalon is mechanically limited by  $10 \text{ cm}^{-1}$ , after that the scan is interrupted by computer to realign the etalon for further scan, so it's difficult to apply this mode of operation for search of gain maximum position when new Raman crystals are investigated.

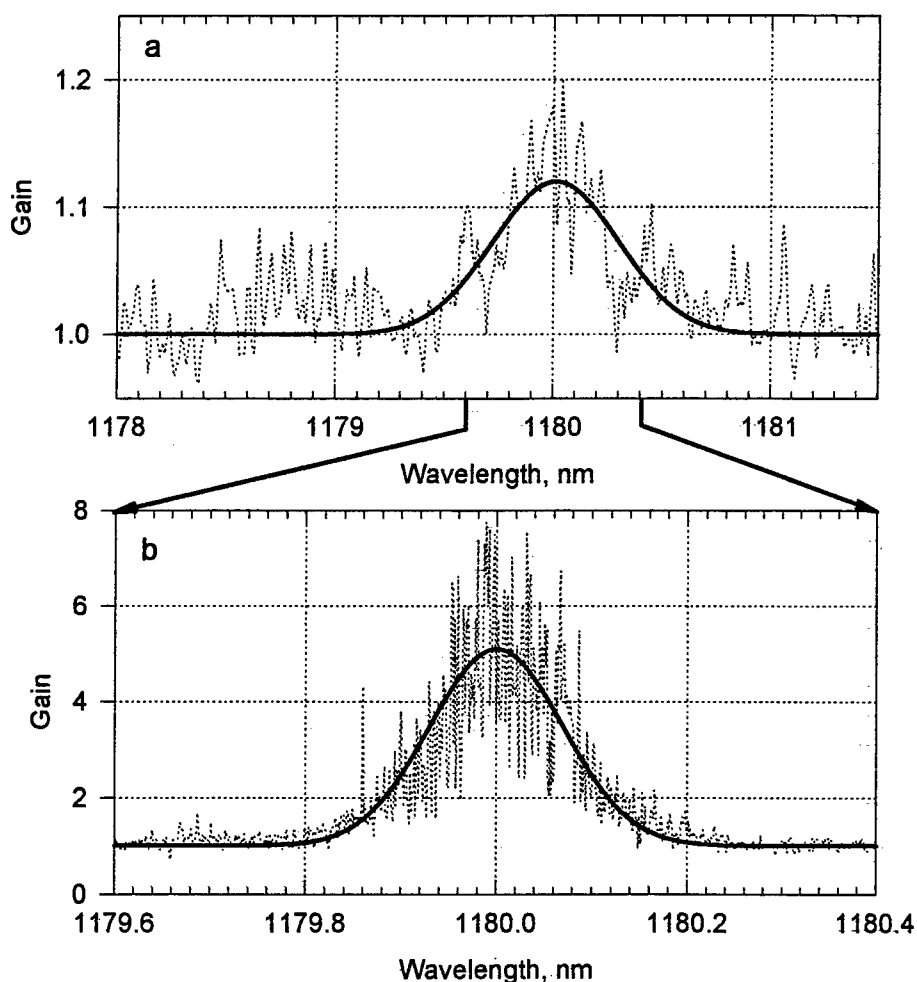


Fig. 4.3 The measured gain spectra of  $\text{Ba}(\text{WO}_4)_2$  crystal with the probe laser scanned without (a) and with (b) intracavity etalon.

The described procedure can be illustrated by the spectra shown in Fig. 4.3. Fig. 4.3a demonstrates the broadband scan with the wide spontaneous Raman gain spectra of BaWO<sub>4</sub> crystal. The width of the line is fully defined by the probe laser linewidth and is measured to be about 5 Å. The further scan with the probe laser line of 0.1 cm<sup>-1</sup> in the narrow region around the maximum of the detected line is presented in Fig. 4.3b. The measured width of the gain line in this case is seen to be only 1 Å.

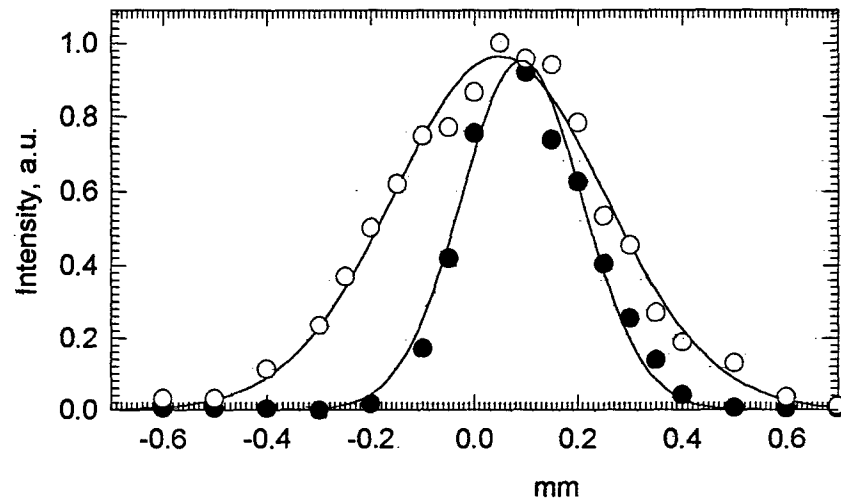


Fig 4.4. Spatial distribution of the pump (A) and probe (B) beams in the crystals

During the Raman amplification experiments the SRS gain coefficient in KGW crystal was measured. Focusing lenses with focal length  $f_{\text{pump}} = 600$  mm and  $f_{\text{probe}} = 300$  mm were used in this case. KGW crystal 1 cm long was set at the waist of probe beam. The spatial overlap and distribution of pump/probe beams at the crystal position were measured by the photodiode and scanning diaphragm with 40  $\mu\text{m}$  diameter. The spatial distribution of the probe and pump beams are shown in Fig. 4.4. As one can see the pump and probe beams are well overlapped. The beam widths at half maximum were 0.6 and 0.3 mm for pump and probe beam correspondingly. Pulse energy measured by energy meter IMO-2 were equal to 24 mJ and 0.04 mJ for pump and probe beams correspondingly. The peak power calculations were based on the pulse temporary shape measured by avalanche photodiode and full pulse energy. Peak power density of the beam with Gaussian shape is connected to peak power and beam width by the following equation:

$$P = \int I(r) dS = \frac{\pi}{4 \ln(2)} I_0 \Delta_{FWHM}^2$$

or

$$I = \frac{4 \ln(2)}{\pi} \frac{P}{\Delta_{FWHM}^2}$$

where  $I$  peak power density,  $P$  peak power and  $\Delta_{FWHM}$  beam widths at half maximum. The temporary shape of the pump/probe power density are shown in Fig. 4.5. As one can see pump and probe beams have good temporal overlap and power density of the pump is more than 100 times exceed the power density of probe pulse. It allows to use weak field approximation for calculation of nonlinear coefficient. The nonlinear Raman amplification cross-section was calculated as following:

$$g = \frac{\ln(I_{am}/I_o)}{I_p l}$$

where  $I_o$ ,  $I_{am}$ ,  $I_p$ , are power density of pump, probe (incident and amplified) pulses correspondingly and  $l$  - is crystal length. The nonlinear Raman amplification cross-section of KGW crystal obtained in our experiments was 1.5 cm/GW. This value may be slightly underestimated due to amplification decrease at wings of spatial distribution of pump beam.

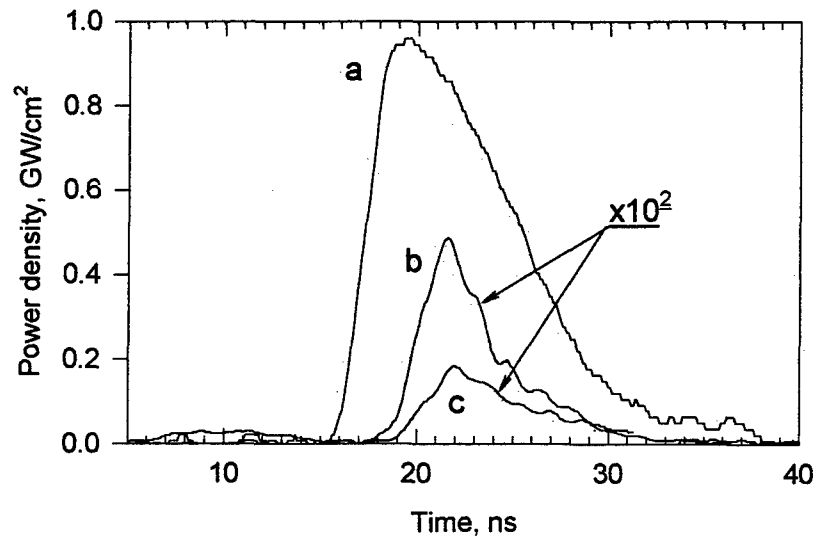


Fig.4.5 Power density of pump (a), amplified (b) and probe (c) beams.

Raman amplification in semiconductor materials such as Si and GaAs were also investigated. However the absorption edge related to the band to band and impurity to band absorption of these crystals is close to the pump wavelength of ( $\lambda = 1.064 \mu\text{m}$ ). It leads to strong laser induced absorption of the radiation in these samples. As an example the transmission of probe (curves

B,C,D) and pump (curve A) pulses through 3 cm long GaAs crystals are shown in Fig. 4.6. As one can see the transmittance of the probe pulse (at  $\lambda = 1.111 \mu\text{m}$ ) is very weak ( $T=0.2\%$ ) even in the absence of pump radiation. The comparison of incident (curve B) and transmitted (curve C) temporal pulse shapes shows that the absorption at the pulse maximum is much stronger than that at the pulse wings due to absorption increase caused by nonlinear processes. Switching of pump radiation to on leads to the additional absorption of the probe beam within the range of the two pulses temporal overlapping (see curve D). Thus for Raman amplification measurements in these crystals it is necessary to shift the pump wavelength far from single and two-photon absorption edge or cool the crystals down to decrease thermally stimulated transitions.

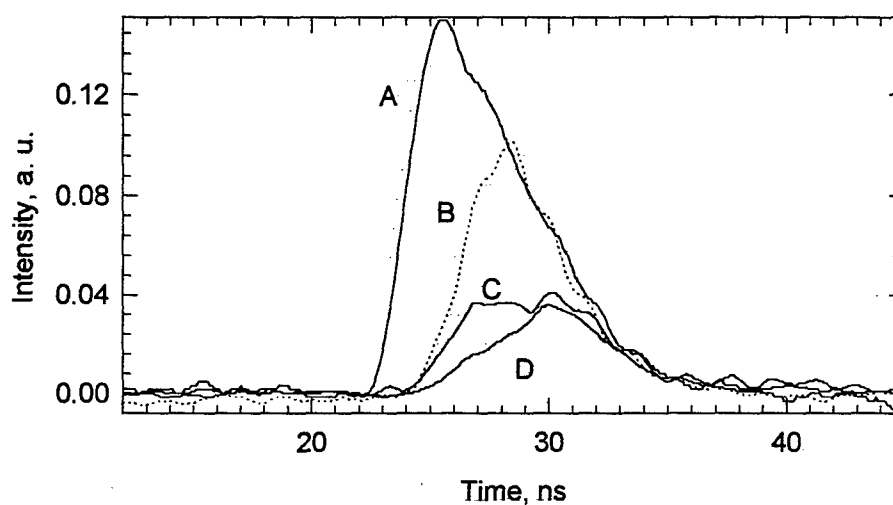


Fig. 4.6 Measured pulse oscillograms.

- A - pump pulse,
- B - Incident probe pulse X0.002 (at  $\lambda=1111.8 \text{ nm}$  wavelength),
- C - Transmitted probe pulse (without pump),
- D - Transmitted probe pulse (under pump).

Spontaneous Raman gain measurements for GaP crystal 1.5 cm long were performed. The known drawback of this semiconductor material is low damage threshold. This demanded the pump power to be decreased strongly compared to tungstate crystals. This was achieved by increasing the pump beam diameter combined with stronger pump beam attenuation. Simultaneous attenuation of the probe beam was performed to keep the relation between the pump and probe beams power density nearly unchanged. The measured spontaneous Raman gain spectra scanned with intracavity etalon inserted is shown in Fig. 4.7. The observed small gain and small signal to noise ratio here are due to very low pump power density compared to experiments with tungstate crystals and can be improved by applying longer sample crystals.

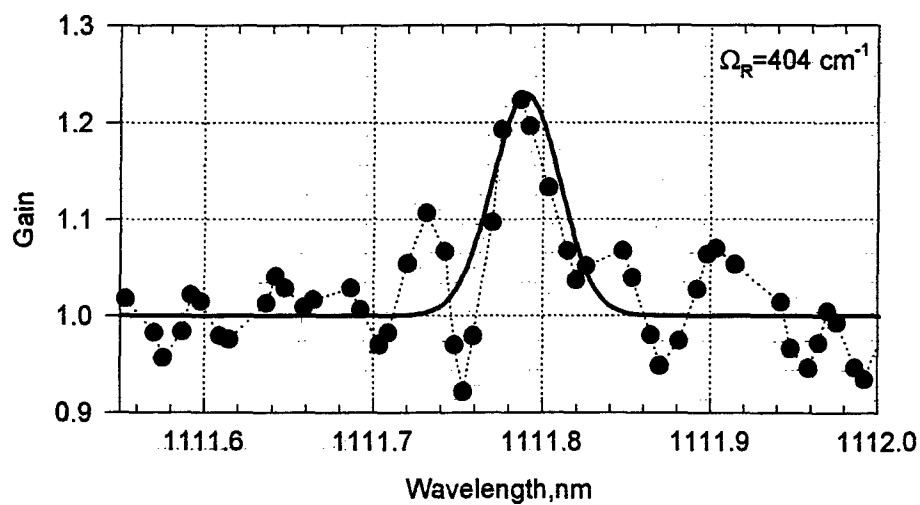


Fig. 4.7 Raman amplification spectra of of 1.5 cm long GaP crystal.

1. P. G. Zverev, T. T. Basiev, "Investigation of the line broadening of a SRS-active vibration in a barium nitrate crystal by two-photon Raman amplification spectroscopy," *Quantum Electronics*, **25**, 1204-1207 (1995).